

UNIVERSITY OF SÃO PAULO
POLYTECHNIC SCHOOL

NIKOLAS LUKIN

Metamodeling of structural failure:

Case study of API S-135 steel tube cut in BOP

São Paulo

2020

NIKOLAS LUKIN

Metamodeling of structural failure:

Case study of API S-135 steel tube cut in BOP

Thesis submitted to the Polytechnic School of the University of São Paulo in fulfillment of the requirements for the degree of Doctor of Science.

São Paulo

2020

NIKOLAS LUKIN

Metamodeling of structural failure:

Case study of API S-135 steel tube cut in BOP

Revised version

Thesis submitted to the Polytechnic School of the University of São Paulo in fulfillment of the requirements for the degree of Doctor of Science.

Concentration area: Mechanical engineering, project and manufacturing.

Supervisors:

Prof. DSc. Larissa Driemeier

Prof. DSc. Michael Brünig

São Paulo

2020

Autorizo a reprodução e divulgação total ou parcial deste trabalho, por qualquer meio convencional ou eletrônico, para fins de estudo e pesquisa, desde que citada a fonte.

Este exemplar foi revisado e corrigido em relação a versão original, sob responsabilidade única do autor e com a anuência de seu orientador.

São Paulo, ____ de _____ de _____

Assinatura do autor: _____

Assinatura do orientador: _____

Catálogo-na-publicação

Lukin, Nikolas

Metamodeling of structural failure: case study of API S-135 steel tube cut in BOP / N. Lukin -- versão corr. -- São Paulo, 2020.
157 p.

Tese (Doutorado) - Escola Politécnica da Universidade de São Paulo. Departamento de Engenharia Mecatrônica e de Sistemas Mecânicos.

1.Finite Element Method 2.Structural fracture 3.Statistical interpolation 4.Drilling rig equipment 5.Drilling strings I.Universidade de São Paulo. Escola Politécnica. Departamento de Engenharia Mecatrônica e de Sistemas Mecânicos II.t.

Dedicated to the memory of COVID-19 victims

ACKNOWLEDGMENTS

This thesis is devoted to whom dedicates his/her time and efforts to science improvement as research proved to be fundamental to life as COVID-19 outbreaked worldwide. The conclusion of this thesis was possible thanks to the help I received, which I would like to thank with gratitude here. Please forgive me if I forgotten someone. I would like specially to thank my mother Ivete, my grandmother Eugênia, Prof. DSc. Raquel Lobosco and my advisor, Prof. DSc. Larissa, for the countless hours spent and patience to guide my work. Thanks to Prof. DSc. Rafael Traldi Moura, Prof. DSc. Marcílio Alves, Rafael Oliveira Ferreira, Prof. DSc. Izabel Machado, Érick Reis from University of São Paulo for the support given to manufacturing and analyzing the tested specimens, as well as to Janek Tix and Steffen Gerke from Bundeswehr University who made it possible DIC analysis. Mention to Mr. Washington Coelho from Thread Pipe Machine C. Serviços LTDA (Macaé) who donated the tube sample and, finally, to my best friends Renata, Bruno and Richard for contributing to the thesis preparation. My personal gratefulness for my colleagues in Petrobras whom the acquaintanceship made me a better person, as well as to our Company for the data provided.

This research did not receive any specific grant from funding agencies of the public, commercial, or not-for-profit sectors.

Metamodeling of structural failure: case study of API S-135 steel tube cut in BOP

In offshore oil exploration, it is necessary the use of a Dynamic Positioning System (DPS) to maintain the platform at a fixed point regardless of the influence of the environment. In an event of failure, however, a drill string inside BOP (BlowOut Preventer) must be cut using its indenters and safely disconnected from the well. Therefore, it is needed an accurate and realistic virtual model of this failure process. Numerical model analysis, in addition to avoid expensive and complex experimental tests, allows, through post-processing tools, a detailed understanding of all phases of the failure process. On a first stage, API S-135 steel, a material commonly used to manufacture drill strings, is characterized using Johnson-Cook model (J-C) for plasticity and failure. The material parameters are obtained from experimental tensile tests on dog bone and 3-point bending beams specimens with different notch radii, covering a wide range of stress triaxialities. Experimental tests and numerical simulations were compared by means of stress-strain curves, Digital Image Correlation (DIC) and Scanning Electron Microscopy (SEM) to validate the model. The material model is applied to simulate the pipe cutting process and to predict the required force for the BOP to cut drill pipes with different geometries, which in comparison to experimental tests permitted to determine BOP internal frictions. Additionally, the numerical simulation also allowed a better understanding of the cutting process here presented as well, coherent to SEM imaging of a similar cut tube in BOP. The required force to cut the string is traditionally determined by analytical models and commissioning tests, which can be far from the real situations. Depending on boundary conditions of this tubular, the BOP may fail to cut it, which can lead to catastrophic events. In this way, a metamodel is defined to predict required forces for BOP to cut API S-135 6.63" 40.87ppf drill pipes, with different boundary conditions. Different simulations in combined conditions, including initial traction and torque, pipe decentralization and indenter offsetting, were performed in order to find the required force in indentator to cut the pipe. Such data were used to develop a metamodel using feed a machine learning algorithm which leads to conclude that current BOP cutting models may underestimate the required force to cut pipe in realistic conditions.

Keywords: Finite Element Method, Structural fracture, Statistical interpolation, Drilling rig equipment, Drilling strings.

Metamodelagem de falha estrutural: estudo de caso do corte do tubo de aço API S-135 em BOP

Na exploração de petróleo offshore, o Sistema de Posicionamento Dinâmico (DPS) é necessário para manter a plataforma em um ponto fixo, independentemente da influência do ambiente. Em caso de falha do DPS, no entanto, uma eventual coluna de perfuração dentro do BOP (BlowOut Preventer) deve ser cortada para uma desconexão segura do poço. Portanto, é necessário um modelo virtual preciso e realista desse processo de falha. A análise de modelos numéricos, além de evitar testes experimentais complexos e caros, permite, por meio de ferramentas de pós-processamento, um entendimento detalhado de todas as fases do processo de falha. Em uma primeira etapa, o aço API S-135, material comumente usado na fabricação de colunas de perfuração, é caracterizado usando o modelo Johnson-Cook (J-C). Os parâmetros do material para o são obtidos a partir de ensaios experimentais de tração em amostras cilíndricas e em vigas de flexão de 3 pontos com diferentes raios de entalhe, cobrindo uma ampla gama de triaxialidades de tensão. Testes experimentais e simulações numéricas foram comparados por meio de curvas tensão-deformação, Correlação Digital de Imagem (DIC) e Microscopia Eletrônica de Varredura (MEV) para validar o modelo de material, o qual é aplicado para simular o processo de corte de tubos e prever a força necessária para o BOP cortar tubos de perfuração com geometrias diferentes. Em comparação com testes experimentais, essas simulações permitiram determinar os atritos internos do BOP, fornecendo também uma melhor compreensão do processo de corte aqui apresentado, coerente com imagens SEM de um tubo semelhante cortado no BOP. A força necessária para cortar um tubo de perfuração é tradicionalmente determinada por modelos analíticos e testes de comissionamento, que podem estar longe das condições reais. Dependendo das condições de contorno deste tubular, o BOP pode falhar em cortá-lo, o que pode levar a eventos catastróficos. Para tanto, um metamodelo é definido para prever as forças necessárias para o BOP cortar um tubo de perfuração API S-135 6.63" 40.87ppf, com diferentes condições de contorno. Diferentes simulações em condições combinadas, incluindo tração e torque inicial, descentralização do tubo e desalinhamento do indentador, foram realizadas para encontrar a força necessária no indentador para cortar o tubo. Tais dados foram usados para desenvolver um metamodelo usando um algoritmo de aprendizado de máquina, levando a concluir que os atuais modelos de corte do BOP podem subestimar a força necessária para cortar o tubo em condições realistas.

Palavras-chave: Método dos Elementos Finitos, Fratura das estruturas, Interpolação estatística, Equipamentos da sonda de perfuração, Colunas de perfuração.

LIST OF FIGURES

Figure 1 - Schematics of earth crust.....	2
Figure 2 - Offshore drilling equipment	3
Figure 3 - Schematics of BOP ram hydraulic system with booster	4
Figure 4 – BOP stack	5
Figure 5 - Schematics of a subsea BOP	5
Figure 6 - Stages of Rig loss of dynamic positioning and disconnection	6
Figure 7 - Steps to cut a pipe in BOP.....	7
Figure 8 - Examples of rams available for BOPs.....	7
Figure 9 - Simplified stress strain curve of a tensile test in ductile material.....	8
Figure 10 - Difference of FEM and metamodels numeric substitutional models.....	10
Figure 11 - Development of metamodels to predict structural failure	11
Figure 12 - Experimental apparatus for testing indentation of tubes	13
Figure 13 - Elements of the analytical model: rings and generators, including their connection	14
Figure 14 - Pipe shear force obtained by experimental results x predicted by DET model	16
Figure 15 - Telkin (2010) FEM model and results	17
Figure 16 - Koutsolelos (2012) FEM model.....	17
Figure 17 - Liu (2017) FEM model.....	18
Figure 18 - Stress state represented in Haigh-Westergaard plane.....	25
Figure 19 - Ductile polycrystalline metals failure mechanism proposed by NOELL et al (2018)	29
Figure 20 - Necking of ligament between two voids	30
Figure 21 - Shear bands between two voids	31
Figure 22 - Representation of fracture due to shearing (left) and necking coalescence due to spherical growth of voids (right).....	31
Figure 23 - Dependence of the equivalent strain to fracture on the stress triaxiality, for testing performed with plain stress specimens.....	34
Figure 24 – Comparison of fracture strain predicted by Johnson-Cook (1985) and Bai-Wierzbicki (2009) models.....	35
Figure 25 - Effect of voids in a material matrix subjected to a load	37
Figure 26 - Effect of damage on the material matrix stiffness.....	39
Figure 27 - Stress x Strain curve with progressive damage evolution.....	41
Figure 28 - Layer used to build a metamodel	42
Figure 29 - Representation of different failure modes on a tube cut in BOP as a function of internal pressure (P_i) and traction (N)	43
Figure 30 - Example of sampling method in 5x5 space using Latin Square.....	45
Figure 31 – Space filling illustration of inputted values for a two variables domain	47
Figure 32 - Flowchart of generating DoE simulations for metamodel construction	48

Figure 33 - Regression and regularization effects on coefficients	51
Figure 34 – Proposed methodology	54
Figure 35 – 5.5” 21.9ppf drill pipe used for manufacturing testing specimens .	57
Figure 36 - Specimens extraction process	58
Figure 37 – INSTRON 3369 universal testing machine and experimental arrangement at GMSIE/USP	59
Figure 38 - DIC analysis of tensile testing at LFS/USP	59
Figure 39 - JEOL JSM-6010LA scanning electronic microscope.....	60
Figure 40 – Samples for measurement of hardness property	61
Figure 41 - Expected stress states of classical TPs	62
Figure 42 – Geometry of smooth (dog-bone) and notched round bars specimens	63
Figure 43 - Geometry of flat specimens	63
Figure 44 - Tensile Dog-bone specimen	64
Figure 45 - 3-point-bending specimen.....	64
Figure 46 - BOP shear testing protocol	66
Figure 47 - Pipe being positioned inside BOP for shear testing	66
Figure 48 - Drill pipe cut in BOP	67
Figure 49 - Pressure spectra (in psi) obtained in Shear ram piston during shearing process as a function of time	68
Figure 50 - Hydril BSR rams.....	68
Figure 51 - Shaffer CVX ram.....	69
Figure 52 - Geometry of the testing specimens modeled by FEM.....	70
Figure 53 - Model constrains of BOP commissioning case model.....	71
Figure 54 - Geometry for pipe cut in BOP commissioning case	72
Figure 55 - Model constrains of pipe stuck in well case model.....	73
Figure 56 - Geometry of the pipe cut in BOP model (dimensions in mm).....	73
Figure 57 - Affected area by shearing	75
Figure 58 - Test sample length requirement.....	75
Figure 59 – Partition on model mesh.....	76
Figure 60 - Shear forces x Cross sectional pipe area obtained from literature and Petrobras.....	77
Figure 61 – Unnotched DB NN specimen	79
Figure 62 - Notched DB NT01 specimen.....	79
Figure 63 - Notched DB NT02 specimen.....	79
Figure 64 - Notched DB NT10 specimen.....	79
Figure 65 - Beam specimens after 3-point-bending test.....	80
Figure 66 – Process flowchart for material model calibration	81
Figure 67 - Triaxiality x normalized distance from DB center	82
Figure 68 - Calibration procedure for damage initiation model	82
Figure 69 - DB sample failure.....	83
Figure 70 - Stress and strains for unnotched specimen and FEM material calibration procedure	84

Figure 71 - Comparison of experimental and FEM simulation of DB notched specimens	85
Figure 72 - Numerical predicted axial strain field in comparison to its experimentally measured results in DBs specimens	87
Figure 73 - Numerical predicted 1 st principal strain field in comparison to its experimentally measured results at failure onset	88
Figure 74 - Numerical predicted 2 nd principal strain field in comparison to its experimentally measured results at failure onset	89
Figure 75 - Comparison of experimental and FEM simulation of force-displacement curves in 3-point-bending tests.....	90
Figure 76 – Pipe cutting simulation in different ram displacements (δ)	91
Figure 77 – 6.63" 40.87ppf drill pipe after cut.....	92
Figure 78 - Numerical predicted PEEQ and triaxiality field in cut cross section of 6.63" 40.87ppf drill pipe in no load condition along process of cut.....	94
Figure 79 - Numerical stress analysis in cut cross section of 6.63" 40.87ppf drill pipe for different project variables at onset of pipe cut	95
Figure 80 - Comparison of surface microscopy, microhardness and FEM measurements in the cross-sectional area of a 6 5/8" 40.87ppf tubular.....	97
Figure 81 – Pipe geometry after cut in BOP	98
Figure 82 – Comparison of numerical and experimental plot of principal dimensions of the sheared pipe with respect to the original pipe diameter (OD_0)	100
Figure 83 - Required force to shear a pipe x pipe cross sectional area: FEM x experimental results	101
Figure 84 – Experimental arranged used to measure pressure on the closing chamber	102
Figure 85 - Normalized displacement for 6.63" 40.87ppf drill pipe cut in BOP	103
Figure 86 - Process flowchart for metamodel construction.....	104
Figure 87 - Mesh convergence study	105
Figure 88 – Example of energy balance for compatible boundary conditions	107
Figure 89 – Example of energy balance for incompatible boundary conditions	107
Figure 90 – ElasticNet tuning	109
Figure 91 – Accuracy x generalization for different models of data analysis ..	110
Figure 92 – Metamodel training accuracy for different analysis models and iteration cycles.....	111
Figure 93 – Rate of convergence for different analysis models using train data	111
Figure 94 – Metamodel generalization accuracy for different analysis models and iteration cycles.....	112
Figure 95 – Rate of convergence for different analysis models using test data	112
Figure 96 – Metamodel complexity for different analysis models and iteration cycles	113

Figure 97 Metamodel parameters convergence using OLR for different iteration cycles	113
Figure 98 –Metamodel parameters convergence using Ridge for different iteration cycles.....	114
Figure 99 –Metamodel parameters convergence using Lasso for different iteration cycles.....	114
Figure 100 –Metamodel parameters convergence using ElasticNet for different iteration cycles.....	115
Figure 101 - Effect of T^* and N^* on F^*	116
Figure 102 - Effect of Pe^* and Pi^* on F^*	117
Figure 103 - Effect of h^* and d^* on F^*	117
Figure 104 - Effect of T^* and N^* on F^* with attenuated pressure dataset ...	118
Figure 105 - Effect of h^* and d^* on F^* with attenuated pressure dataset	119
Figure 106 – Capability plot for pipe cutting as a function of ΔP and d in different BOPs.....	120
Figure 107 - Different FEM element types.....	133
Figure 108 - Manufacturing project for DB specimens	136
Figure 109 - Manufacturing project for specimens of plate 1.....	137
Figure 110 - Manufacturing project for specimens of plate 2.....	138
Figure 111 - Manufacturing project for specimens of plate 3.....	139
Figure 112 - Manufacturing project for specimens of plate 4.....	140
Figure 113 – Drill pipe geometrical properties	141
Figure 114 - 5" x 19,5 lb/ft (2012).....	146
Figure 115 - 5 1/2" x 21,90lb/ft (2011).....	146
Figure 116 - 5 7/8" x 26,7 lb/ft (2011).....	147
Figure 117 - 6 5/8" x 48,13 lb/ft (2011).....	147

LIST OF TABLES

Table 1 - Summary of works done in pipe cutting in BOP problem found in literature	19
Table 2 - (Cont.) Summary of works done in pipe cutting in BOP problem found in literature.....	20
Table 3 - Effect of boundary conditions in the tubular cutting force	21
Table 4 - Failure models for ductile materials.....	31
Table 5 - Sudden failure models.....	32
Table 6 - Samples mechanical properties	56
Table 7 - Chemical composition for S-135 pipes	56
Table 8 - Geometrical properties of the studied pipes	57
Table 9 - Classical shapes for testing specimens.....	62
Table 10 - Dimensions measured for cylindrical DB specimens.....	65
Table 11 - Dimensions measured for 3-point bending testing beams.....	65
Table 12 - Mesh shaping used for numerical models	70
Table 13 – Summary of BOP commissioning case model constrains	71
Table 14 – Summary of pipe stuck in well case model constrains.....	73
Table 15 – Project variables limits.....	74
Table 16 - Summary of experimental pipe cutting tests.....	78
Table 17 – Measured chemical composition by EDS for the tested samples ...	78
Table 18 - API S-135 steel properties	85
Table 19 – Measured chemical composition by EDS for the cut tube	96
Table 20 - Comparison of sheared pipe geometries trough experimental and FEM numerical results.....	99
Table 21 - Summary of experimental and numerical results of pipe cut forces	101
Table 22 - Compatible simulations as a function of iteration cycles	108
Table 23 - API S-135 6 5/8” 40.87ppf tube fracture properties obtained from tube manufacturer	108
Table 24 - Normalized input variables	109
Table 25 - Maximum force delivered by BOP as a function of actuating pressure and driving piston size.....	120
Table 26 - Summary of project variables effect in pipe cut.....	123
Table 27 – Drill pipe geometrical properties	142
Table 28 - Data of pipe cut in BOP from Petrobras and open literature	143
Table 29 - FEM simulations results	148

TABLE OF NOTATION

α	Penalty factor for regularization (tuning parameter)
β	Metamodel parameters vector
$\beta_{k,l}$	Metamodel parameters
δ	Ram displacement
$\delta_{i,j}$	Kronecker delta
$\bar{\varepsilon}^p$	Equivalent plastic local strain
$\bar{\varepsilon}_D^p$	Equivalent plastic local strain at onset of damage nucleation
ε_f^p	Equivalent plastic local strain at failure
ε_{MM}	Metamodel convergence error
ε_β	Metamodel's coefficients convergence error
ξ_L	Length along Haight-Westergaard cylindrical axis
ϵ_i	Error of metamodel estimation on each FEM simulation
$\varphi_{k,l,i}$	Variable functions of data regression
γ	ElasticNet mixing parameter
λ	Stress tensor eigenvalue
η	Stress triaxiality
Ω	Rate of learning
σ_u	Ultimate tension
σ_y	Yield tension
σ_n	Normal tension
σ_{eq}	(Von Mises) equivalent tension
σ_H	Hydrostatic tension
σ	Cauchy stress tensor
$\sigma_{i,j}$	Stress tensor component
$\tilde{\sigma}$	Effective stress tensor
θ^*	Homogeneous temperature
θ_L	Lode angle parameter

A	Coefficients matrix for linear system
b	Constant column vector for linear system
BE	Energy balance
C	Global dumping matrix
$C_{1\dots n}$	Plasticity model parameters
$D_{1\dots n}$	Failure model parameters
d	Offset of tube from BOP center
d^*	Normalized offset of tube from BOP center
D_m	Damage measure
D_{cr}	Critical damage measure (damage at failure)
D_i	Undeformed tube internal diameter
$D_e = OD$	Undeformed tube external diameter
E	Elastic module (Young modulus)
\tilde{E}	Effective elastic module
E_I	System internal energy
E_K	System kinetic energy
E_W	System external work
$E_{Residue}$	System total energy residue
f	BOP internal frictions
F	Force on indenter to cut tube predicted by metamodel
F^*	Normalized force on indenter to cut tube predicted by metamodel
F_{DTE}	Required (ultimate) force to cut a pipe by analytical DTE model
F_{FEM}	Required (ultimate) force to cut a pipe by numerical FEM model
F_{EXP}	Required experimentally (ultimate) measured force to cut a pipe
$F_{EXP}SD$	Standard deviations for observed experimental force to cut pipe
F_{ram}	Maximum force delivered by the ram
G_f	Hillerborg energy fracture parameter
h	Indenter (ram) offset
h^*	Normalized indenter offset
H	Number of project variables

i	simulation index
\mathbf{I}	Identity matrix
I_1, I_2, I_3	Cauchy stress tensor invariants
J_1, J_2, J_3	Deviatoric stress tensor invariants
j	Iteration index
\mathbf{K}	Global stiffness matrix
k	Boundary condition index
k_f	Force - cross sectional area coefficient
k_t	ElasticNet tuning parameter
L	Lode angle
L_c	FEM element characteristic length
m	Failure mode index
\mathbf{M}	Global mass matrix
n	Numerical simulations cycle
N	Traction force applied on tube edges
N_u	Tube rupture traction force
N^*	Normalized traction force on tube edges
N_{sim}	Number of available simulations data
$N_{sim_{min}}$	Minimum number of simulations to be performed
$N_{sim_{train}}$	Number of available simulations data for metamodel training
$N_{sim_{test}}$	Number of available simulations data for metamodel testing
n_j	Stress tensor eigenvector
$OD_{1,2}$	Dimensions of cut pipe
p	Number of nonzero metamodel terms
P_{act}	Actuating hydraulic pressure on BOP ram
P_e	External pressure on tube
$P_{e,u}$	Tube collapse external pressure
P_e^*	Normalized external pressure on tube
P_i	Internal pressure on tube
$P_{i,u}$	Tube rupture internal pressure

P_i^*	Normalized internal pressure on tube
ΔP	Differential pressure on tube
Q	Polynomial order of metamodel
R_e	Undeformed tube external radii
R	Notch radii
R^2	Correlation coefficient
R_{adj}^2	Adjusted correlation coefficient
R_{test}^2	Adjusted correlation coefficient for test data
R_{train}^2	Adjusted correlation coefficient for training data
$r_0(\cdot)$	Random function
\mathbf{s}	Deviatoric stress tensor
$s_{i,j}$	Deviatoric stress tensor component
S	Effective cross-sectional area
S_0	Undamaged cross-sectional area
S_D	Damaged area in cross sectional
S_{ram}	Driven ram piston area
S_t	Tube cross sectional area
T	Torque applied on tube edges
T_u	Tube rupture torque
T^*	Normalized torque on tube edges
\mathbf{U}	Displacement tensor
\bar{u}^p	Equivalent plastic local displacement
\bar{u}_f^p	Equivalent plastic local displacement at failure
x	Input variable
\mathbf{X}	Project variables vector
y	FEM prediction
\hat{y}	Metamodel prediction

$ $	Module
$\ \ $	Norm of a vector
$(\dot{}) = \frac{\partial}{\partial t}()$	Differentiation with respect to time
$\nabla()$	Gradient of multi-variable function
$\Delta()$	Variation for a discrete function

LIST OF ABBREVIATIONS AND ACRONYMS

<i>BOP</i>	Blowout Preventer
<i>DB</i>	Dog Bone Specimen
<i>DET</i>	Distortion Energy Theory
<i>DoE</i>	Design of Experiments
<i>DP</i>	Drill Pipe
<i>DPS</i>	Dynamic Positioning System
<i>EDM</i>	Electrical Discharge Machine
<i>FEM</i>	Finite Element Method
<i>GMSIE</i>	Group of Solid Mechanics and Structural Impact
<i>GUI</i>	Graphic-User Interface
<i>GTN</i>	Gurson, Tvergaard, Needleman model
<i>LFS</i>	Laboratory of Surface Phenomena
<i>LHS</i>	Latin Hypercube Sampling
<i>NN</i>	Not Notched
<i>NT</i>	Notched
<i>OLR</i>	Ordinary Linear Regression
<i>PEEQ</i>	Plastic Equivalent Strain
<i>RVE</i>	Representative Volume Element
<i>SEM</i>	Scanning Electron Microscopy
<i>SSE</i>	Sum of Squares Errors
<i>SST</i>	Sum of Squares Totals
<i>TP</i>	Testing Piece

CONTENTS

1. Introduction	1
1.1. Motivation.....	1
1.2. Failure modeling.....	8
1.3. Use of metamodels to predict structural failure	9
2. General and specific objectives of this thesis	11
3. State of art and theoretical foundations	13
3.1. Previous studies on pipe cutting in BOP	15
3.2. Material model.....	22
3.2.1. Stress invariants	22
3.2.2. Measurements derived from invariants.....	24
3.2.3. Johnson-Cook plasticity model.....	27
3.2.4. Failure in ductile materials	28
3.2.5. Micromechanical models	30
3.2.6. Phenomenological models.....	32
3.2.7. Continuum Damage Mechanics models	37
3.3. Metamodels.....	41
3.3.1. Structural failure condition	42
3.3.2. Design of Experiment (DoE).....	44
3.3.3. Data analysis	48
4. Materials and Methods.....	54
4.1. Material properties.....	55
4.2. Analyzed material samples	56
4.3. Mechanical testing.....	57
4.3.1. Testing specimens geometry.....	61
4.3.2. BOP commissioning tests.....	65
4.3.3. Geometry for the BOP rams	68
4.4. Numerical models.....	69
4.4.1. Testing pieces model.....	69
4.4.2. Pipe cut in BOP model.....	70
5. Results and discussion	76
5.1. Experimental testing.....	76

5.1.1. Statistical analysis for BOP commissioning data	77
5.1.2. Tensile and bending tests	78
5.2. Material modeling and analysis	80
5.2.1. Material model calibration	80
5.2.2. Material model validation	86
5.3. Pipe cut in BOP analysis	91
5.3.1. Numerical modeling	91
5.3.2. Model validation	96
5.4. Metamodel construction	104
5.4.1. Numerical data generation	105
5.4.2. Machine-learning	107
5.4.3. Results interpretation	119
6. Conclusions	121
7. Further Works	124
References	125
Attachment A: FEM fundamentals	133
Attachment B: Design for manufacturing testing specimens	136
Attachment C: API/ISO drill pipe geometrical properties	141
Attachment D: Data of cut pipes in BOP	143
Attachment E: Cut pipes geometric measurements	146
Attachment F: Simulation results for pipe cut under different boundary conditions	148
Attachment G: Petrobras data disclaimer	155
Attachment H: Publications derived from this thesis	156

1. Introduction

This work aims to provide means to use metamodels technique to predict the effect of project variables in structural failure of a characterized material. The motivation herein came from the pipe cut in BOP problem in oil industry.

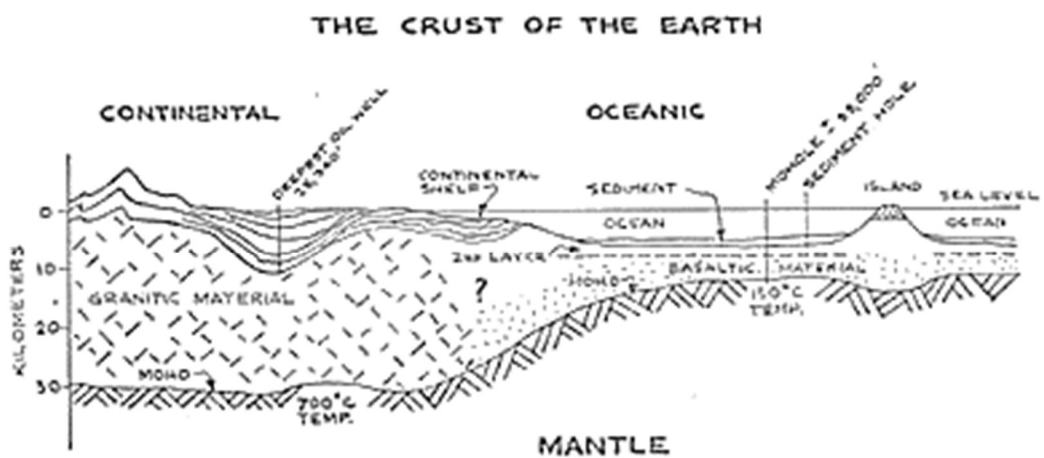
1.1. Motivation

In modern oil industry, offshore drilling operation is a sophisticated and risky process made by means of wear and fracture of rocks inside a well by a bit. The drilling rig transmits mechanical loads to the bit by means of a drill string which is constituted essentially by tubes [1]. Although petroleum was known by the ancient Persians 4000 years ago, it was only in 1859 when it was first extracted from soil by a drilling machine in Pennsylvania (USA) by Edwin Drake. Due to pore pressures in which oil was submitted, it was common the occurrence of uncontrolled petroleum eruptions (or blowouts) as the bit reaches the reservoir. Blowouts causes risk of explosions, losses and decrease in reservoir pressure and, consequently, the amount of oil to be extracted. In order to avoid such undesirable event, a mechanical BOP (Blowout preventer) was developed as a large hydraulically operated arrangement of valves and closure devices, designed, as the name implies, to prevent blowouts, in an operation named "well control" [2]. BOP was invented by James Smither Abercrombie and Harry S. Cameron in 1922 and was brought to market in 1924 by Cameron Iron Works [3].

In its early ages, BOP was a surface equipment, however it became a subsea device as soon as drilling migrated from onshore (explored on continent surface) to offshore explorations (where explorations occurs under water). Along petroleum history, combinations of the commodity price and onshore availability lead to explorations in sea. The first offshore peerless wells were drilled in Caddo Lake (USA) in 1911, in former URSS in late of 20's and in Gulf of Mexico in mid-30's using wood structures in sheltered waters. After war efforts, the first fixed jacket rig platforms with surface BOPs were installed in the late of 50's. Despite all engineering advances made to their construction, fixed platforms were limited to shallow water depths (maximum of 500m). In the same decade, moored rigs

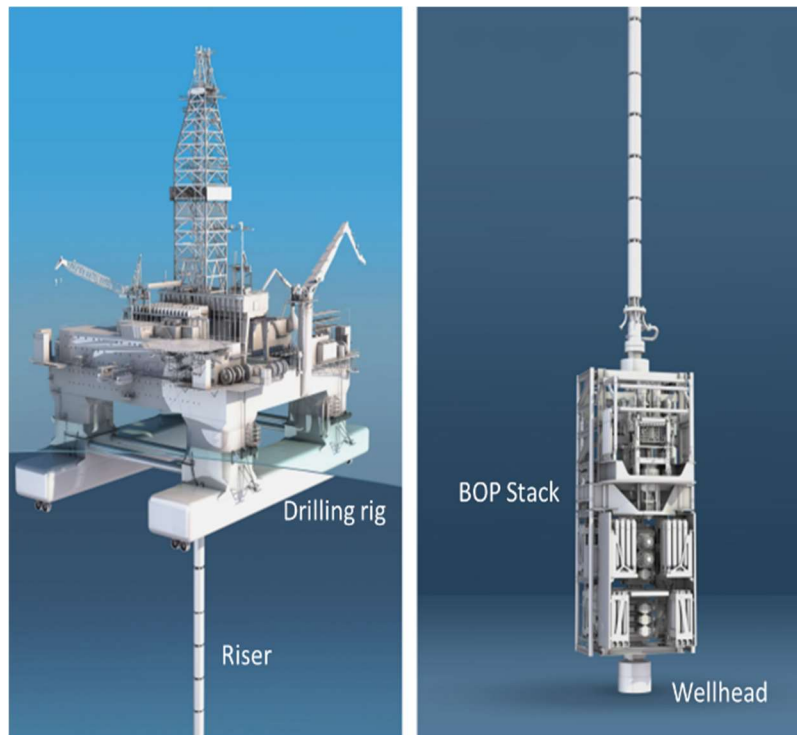
were developed to go beyond with more mobility reaching water depths up to 1000m at the time [4] [5]. To go further, in the early 60's, project Mohole sponsored by USA government provided technological means to drill in deeper waters using subsea BOP and rigs that maintains its position in a point of the sea through dynamic positioning system (DPS). As part of the moon exploration scope, the project purpose was to reach the earth mantle using subsea wells, once the layer of earth crust was thinner in oceanic basins (Figure 1) [6].

Figure 1 - Schematics of earth crust



Source: Extracted from [6].

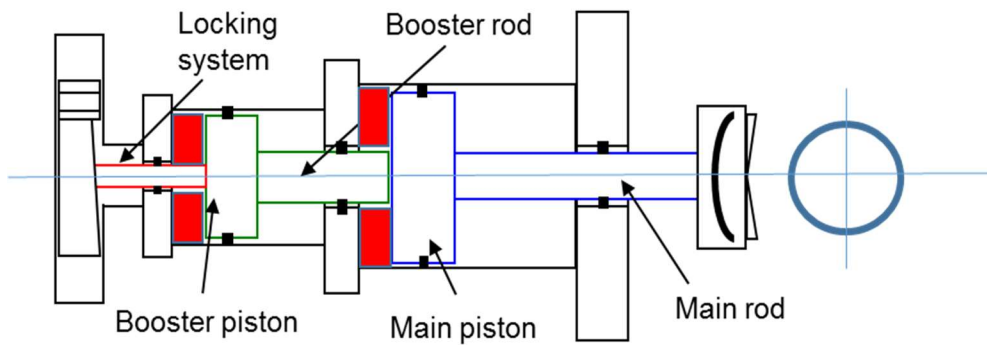
Although the project was discontinued before reaching its main objective, it delivered some subsea drilling techniques still in use. It was conceptualized that for offshore applications, the drill string is isolated from the seawater by a drilling riser, which is constituted essentially by pipe sections extended from seabed to surface and connected to the BOP located at the top of the wellhead [7]. Figure 2 indicates the main parts of the conceptualized deep water drilling equipment, which is currently used nowadays.

Figure 2 - Offshore drilling equipment

Source: Extracted from [8].

A BOP is made of stacked valves, divided into different groups, according to their mechanism and function: annular, variable bore pipe rams and blind rams (or sealing rams). Annular and pipe ram are designed to close and seal the well, without damaging it [9] and were used in the first surface BOPs. Blind rams are used to close and seal the well without a pipe through BOP. The rams are driven by shafts (main rod), supported by hydraulic pistons (main piston). In order to multiply force, some ram assemblies have a second pair of rod and piston (namely booster) connected to the main system, as shown in Figure 3. The actuating pressure usually varies from 3,000 psi up to 5,000 psi (approximately 207 bar up to 345 bar). The ram system is also provided with a locking mechanism to maintain the ram closed in a fixed position in the event of loss of closing pressure on the pistons.

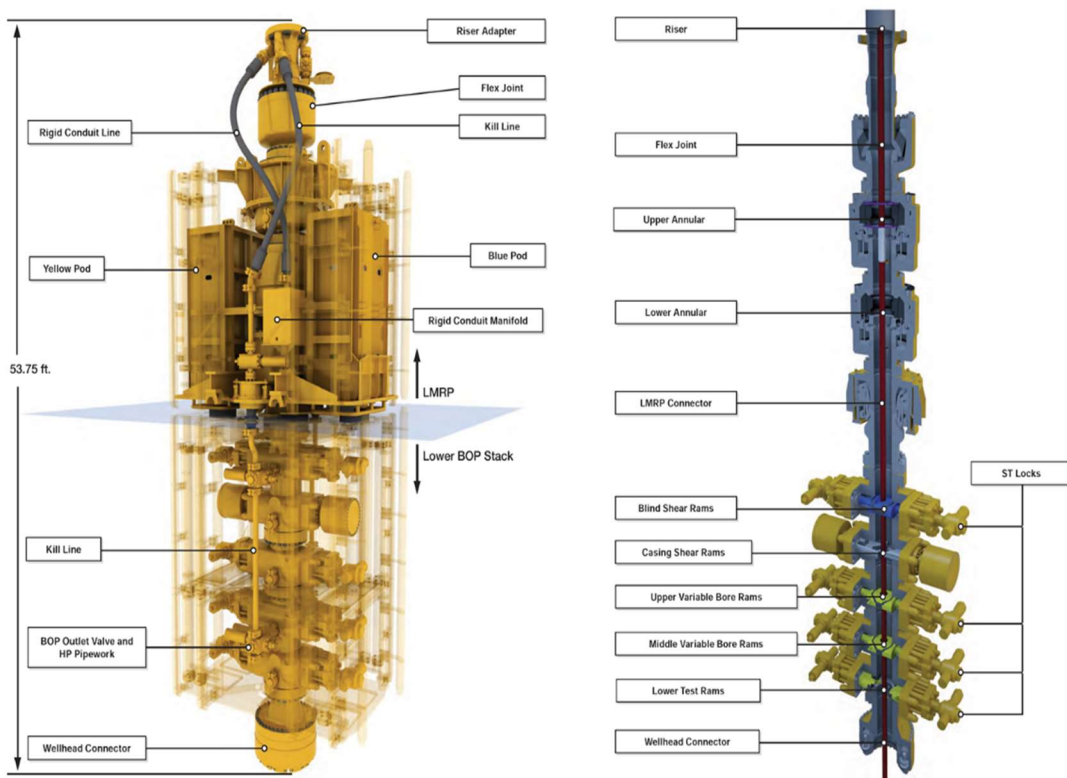
Figure 3 - Schematics of BOP ram hydraulic system with booster



Source: Petrobras.

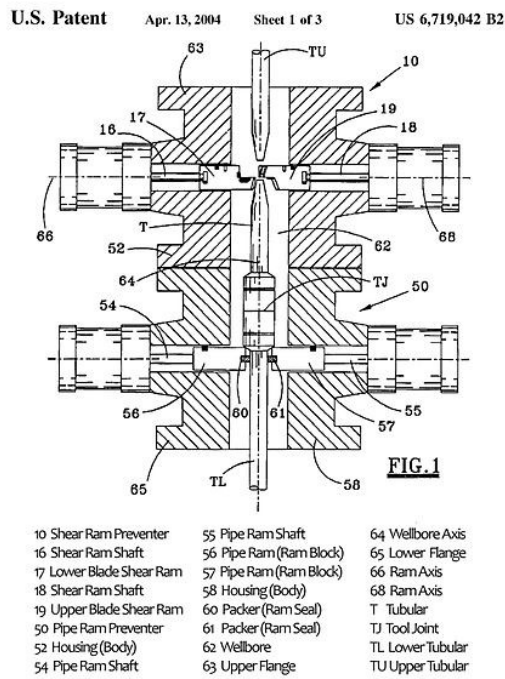
Surface BOPs were adapted and improved to be used under water. In subsea BOPs a mechanism to disconnect BOP from the wellhead is needed. Thus, blind rams from surface BOPs were substituted by blind shear rams and casing shear rams, which are designed to cut a drill string inside BOP to close and seal the well. Moreover, subsea BOPs consist in two retrievable sections: LMRP (Lower Marine Riser Package), that enables quick disconnection between marine riser and BOP in emergency situation, and a lower section known as the BOP stack which remains connected to the well. The lower BOP stack contains a series of rams arranged according to the operator's requirements. Figure 4 shows an example of typical BOP from Cameron manufacturer, as detailed in Transocean (2011) [10]. A more detailed scheme of a subsea BOP stack is illustrated in Figure 5.

Figure 4 – BOP stack



Source: Adapted from Transocean (2011) [10].

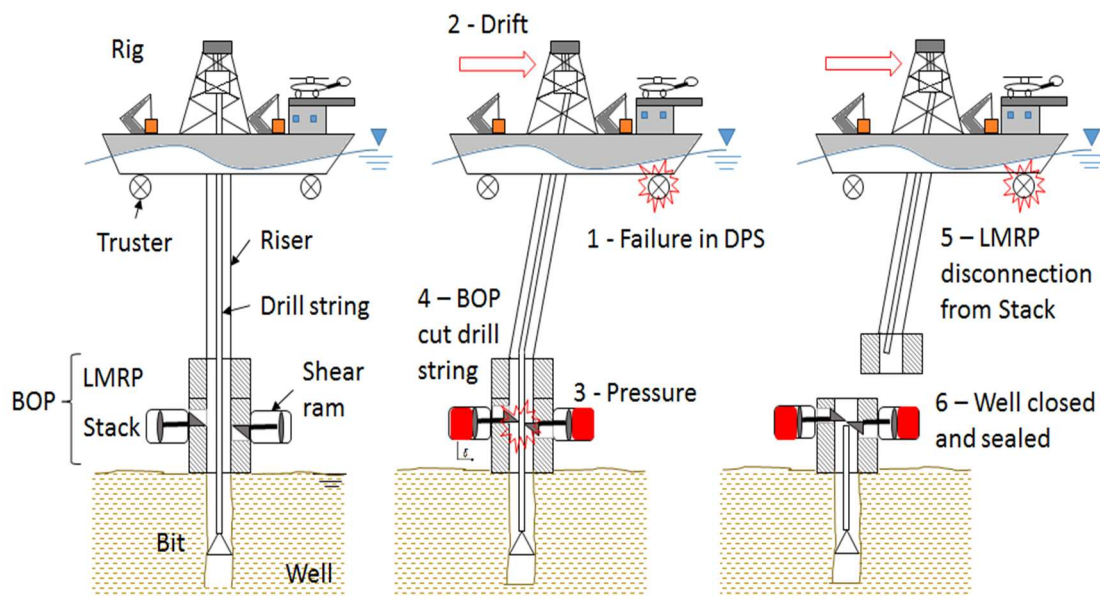
Figure 5 - Schematics of a subsea BOP



Source: Extracted from [11].

Accordingly, assuming that there is a loss of dynamic positioning (drift) due to DPS failure or extreme weather, the shear ram preventer is activated by hydraulic pressure and must be capable to close and seal the well, cutting any drill string existing inside the BOP in order to allow disconnection of LMRP from Stack, as illustrated in Figure 6. Once disconnected, the rig can move away while the lower BOP stack remains on the wellhead to seal and protect the well.

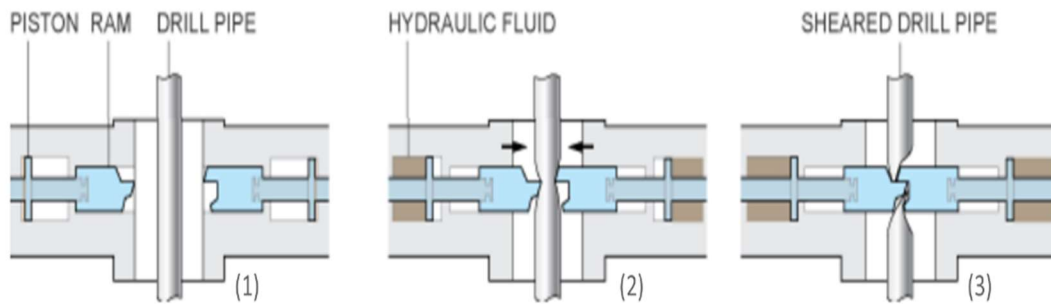
Figure 6 - Stages of Rig loss of dynamic positioning and disconnection



Source: Personal file.

Planned failure through cutting the pipe by shear rams are necessary to close and seal the well. The steps for cutting the pipe string are highly nonlinear and are illustrated in Figure 7: ram movement (1), contact with pipe (2), pipe deformation (3) and pipe cutting (4).

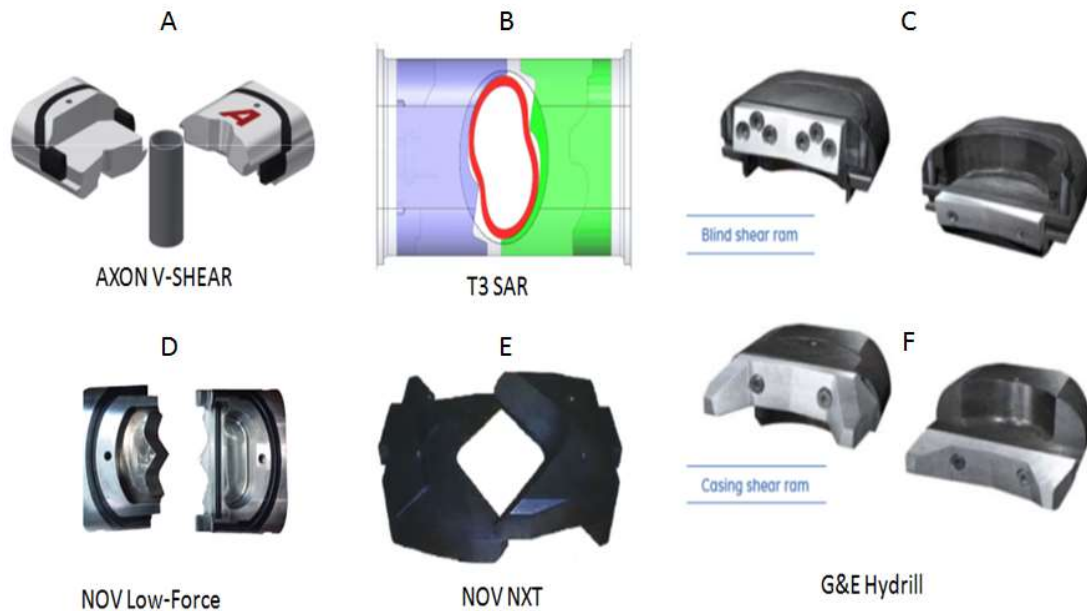
Figure 7 - Steps to cut a pipe in BOP.



Source: Extracted from [12].

There are different models of shear rams available in the market and they induce different stress states on the object to be cut [13] [14]. Some of the available rams are shown in Figure 8. Those rams essentially have two mechanisms to shear pipes: pure shearing (*A, C, E, F*) and puncture combined with shearing (*B, D*).

Figure 8 - Examples of rams available for BOPs

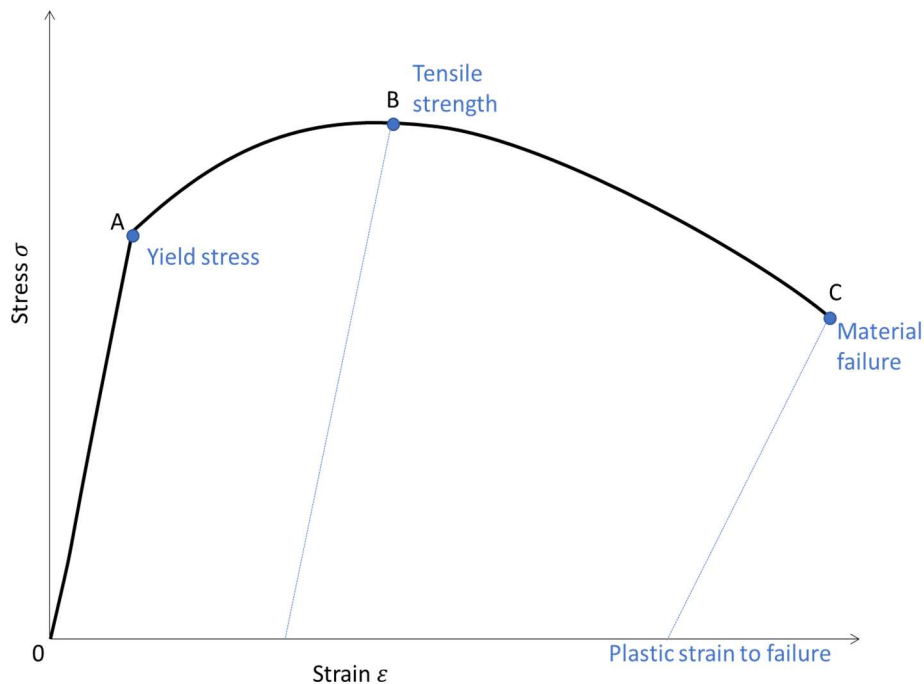


Source: Personal file.

1.2. Failure modeling

When external forces are applied to a constrained deformable structure, the body will be stretched and, consequently, internal forces will develop within the body. The physical quantity that expresses the internal force is called stress and a simplified stress strain curve for a ductile material is illustrated in Figure 9.

Figure 9 - Simplified stress strain curve of a tensile test in ductile material



Source: Personal file.

For relatively small stresses and strains, the material is in the elastic regime, where any deformation due to applied stress is reversed when the force is removed, as illustrated by the region OA in Figure 9. Just beyond the proportional limit the material transitions from elastic behavior to plastic behavior. The yield point, shown in the figure as point “A” (in a simplified version, to maintain a simplicity of approach) is the point where strain increases faster than stress (referred to as “strain hardening”), and the material experiences some amount of permanent plastic deformation. Finally, at point “B” internal damage is evidenced and the curve begins to fall. At this point, the material’s ultimate tensile strength has been reached, that means, it denotes the maximum stress that can be applied to a material in tension before failure [15].

In its simplest version, the failure limit is defined by means of an equivalent critical plastic strain value. However, nowadays, more refined models are available in the literature and they will be discussed further in this thesis. Broadly speaking, it is accepted that ductile material failure occurs due to damage evolution which is generated by nucleation, growth and coalescence of voids inside the material matrix and/or through shear bands formations. An efficient failure model will not cover an unbounded range of stress states, so, it must be adherent to the failure mode, which is the mechanism of failure in the particular studied structure.

1.3. Use of metamodels to predict structural failure

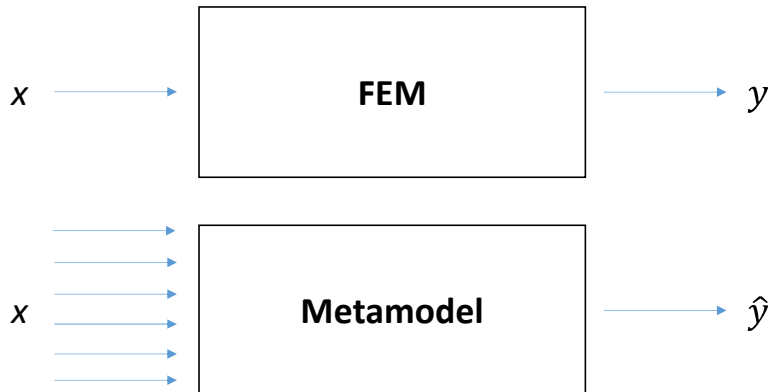
Real mechanical systems may be complex or even unfeasible to model due to the geometry, large number of variables and boundary conditions involved. Moreover, in many real systems, boundary conditions are variable, depending on the service conditions and the environmental effects. The difficulty in this case is that, often, obtaining experimental or directly numerical results is impracticable for several reasons: it generates very high experimental costs (in addition to some conditions not being possible to be simulated experimentally), and, in the numerical case, the combination of the various conditions can generate an extremely large number of options to be simulated [16].

Therefore, to analyze the effect of multiple conditions contained in a continuous and limited domain it is useful an interpolation technique, such as a metamodel. Metamodel is known as “the model of the model” and it will approximate the exact solution, providing a simpler model that mimics the effects of the most important variables in the phenomenon under analysis. Although the solution is not exact, the metamodel minimizes the error to the exact solution. In the context of this thesis, the metamodel allows a general understanding of the effect of different boundary conditions in the mechanism of structural failure.

As illustrated in Figure 10, a set of boundary conditions (including imposed external forces, constraints and contact) namely x , material model and geometry are the input of a FEM analysis and y is the associated structure failure response. In BOP pipe cut, y stands for the ultimate cutting force. While a FEM simulation

provides a unique solution for a single set of boundary conditions, the entrances of a metamodel should be only the boundary conditions for the fixed structure, and the output \hat{y} is the approximate response for a FEM solution with the same input.

Figure 10 - Difference of FEM and metamodels numeric substitutional models



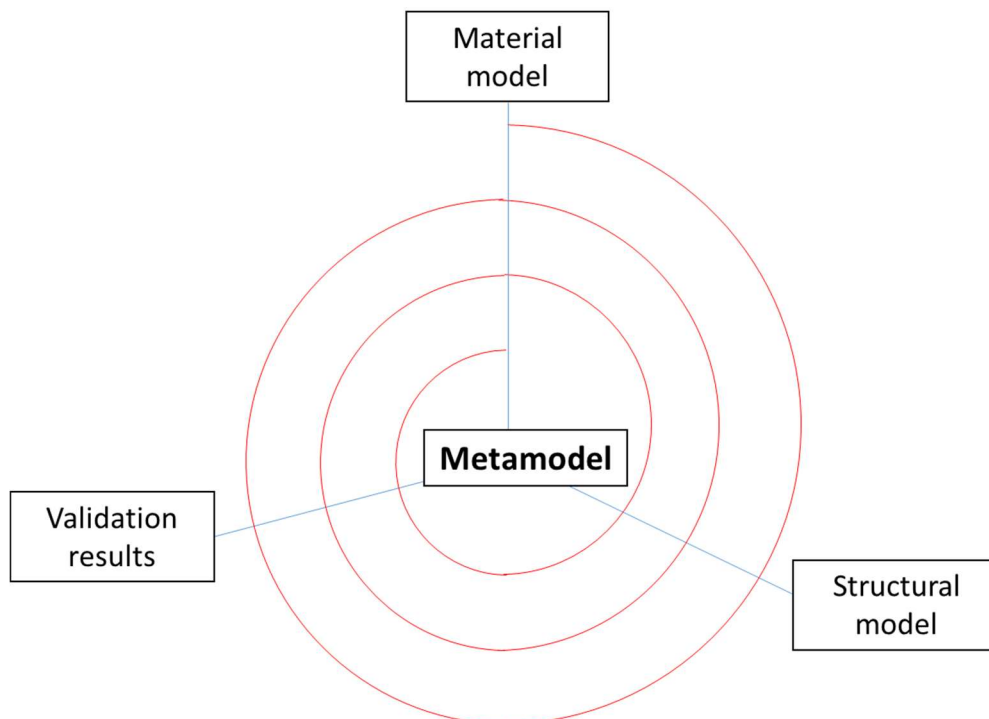
Source: Personal file.

Metamodels may be used to fit data with the best coefficients. However, they must not be used as a true representation of nature, once the measured variable may be influenced by noise effects such as vibrations. Choosing a metamodel that minimizes the error resulting from a model which is also an approximation of reality does not guarantee that it will represent exactly the natural phenomena. Despite the abstraction involved in predicting results for scenarios that are not feasible to be previously experimented, such approximation can provide insights to how boundary conditions can affect a structure and what we can expect from nature [17].

2. General and specific objectives of this thesis

The general objective of this thesis is to generalize the use of metamodels to predict failure in structures as a function of project variables which are selected from a set of essential structural boundary conditions (contact and loadings). A secondary objective is to use the proposed methodology to predict the required force to cut a 6 5/8" API S-135 40.87ppf drill pipe in a BOP to validate the technique and give a technological advance for offshore oil industry. The development of the use of metamodel to predict structural failure is iterative and follows a project spiral as illustrated in Figure 11. To reach the metamodel, the triad material models, structural models and validation results will be verified at each iteration of the development cycle.

Figure 11 - Development of metamodels to predict structural failure



Source: Personal file

To accomplish this objective, initially, the state of art is introduced. Then the main aspects of solid mechanics are reviewed. Thereafter, the failure theory of ductile materials is detailed. Once the structural problem is defined, the most suitable failure model for representing it can be selected in function of the general

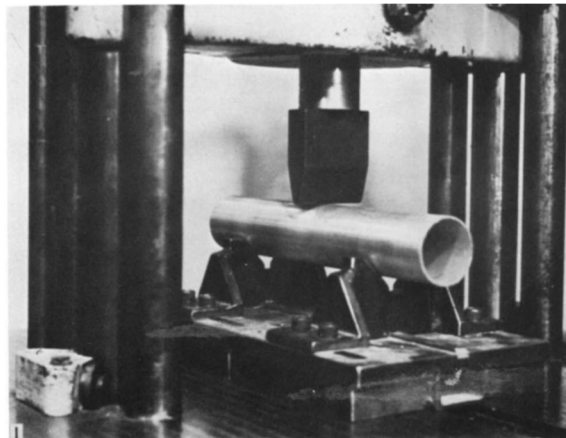
state of stress. Accordingly, experimental tests are performed to calibrate the material model. As soon as the material model is validated, the structural failure analysis is elaborated, simplified to reduce computational cost and also validated. The project variables for simulations are defined and sampled using a design of experiments technique. Finally, a parametric metamodel is sought to agglutinate all simulation results, allowing to interpret, rank and understand the structural failure under different scenarios.

3. State of art and theoretical foundations

The interest is focused on modeling analytically the load-deflection on pipes subjected to transversal indenting emerged in offshore oil and gas exploration. Damage estimation caused by a dropped object (an anchor for example) in a pipeline resting in seabed or by the collision of a supply ship in production risers are some examples [18]. The concept of an analytical model for the pipe-indenting problem was first presented by Runtz and Hodge [19]. They idealized a perfectly plastic tube being crushed between two rigid plates modeled in plane strain. In the model, stationary plastic hinges are formed in the tubular profile as the plates move. The model predicted results adherent with experimental tests in small displacements regime, and divergences were attributed to material nonlinearities. However, the model needed improvement to reflect the real situations involving wedged indenters.

The modes of deformation were experimentally studied by Thomas, Reid and Johnson [20]. They first described the deformation profile of tubes under the action of transverse loading transmitted by different indenter types and force - penetration relations (Figure 12). Later, Ong and Lu [21] modified the boundary conditions of the tube, considering simply supported, fully fixed ends and the whole tube freely resting on a flat surface.

Figure 12 - Experimental apparatus for testing indentation of tubes



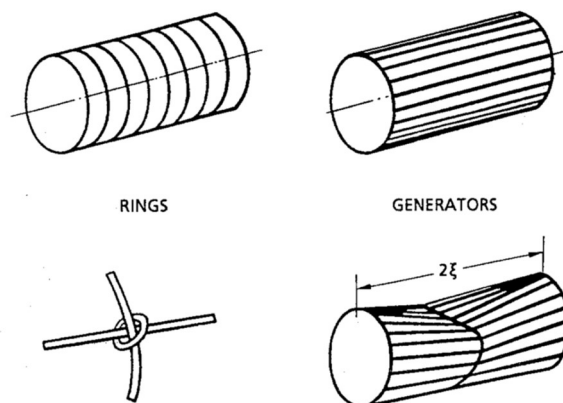
Source: Extracted from [20].

The first “knife on tubular” model, *i.e.*, tube indentation under combined bending and axial loading, was derived by Wierzbicki and Suh [22] and later improved by Moussouros [23]. In the proposed model, the tubulars are constituted of unconnected rings (called slices) and longitudinal beam-strings (generators) made of rigid-perfect plastic material, as illustrated in Figure 13. Slices and generators are loosely connected such that only radial loads are transmitted (no tangential or shearing loads). In this model, most of the indenter energy is absorbed by plastic bending. The proposed general relation for pipe indenting was simplified by Polanco [24], according to:

$$\frac{P}{\sigma_y t^2} = C \left(\frac{D_e}{t} \right)^n \left(\frac{\delta}{R_e} \right)^m \quad (1)$$

where P is the indenter resultant force, C , n and m are constants related to the material and the geometry, D_e is the tube outer diameter (R_e is the tube outer radius), t is the tube thickness, σ_y is the material yield stress and δ is the indenter depth. Studies demonstrated that the range of application of analytical models are also restricted to small indenter displacements [25].

Figure 13 - Elements of the analytical model: rings and generators, including their connection



Source: Extracted from [22].

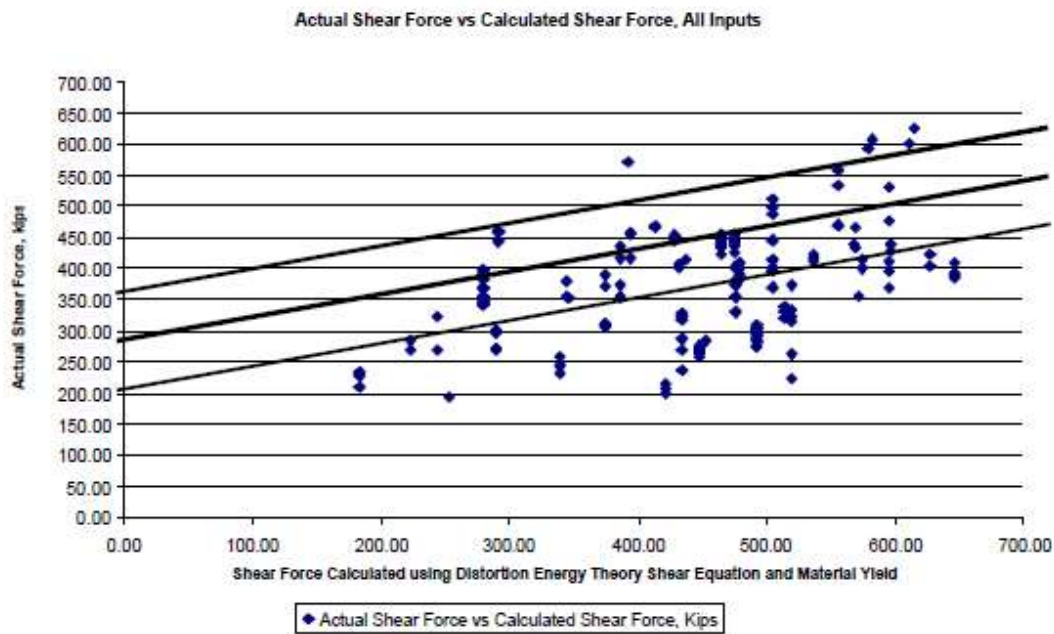
3.1. Previous studies on pipe cutting in BOP

Although BOPs were used since the beginning of the last century in the oilfields, an academic study predicting the required force to cut a pipe in BOP was developed almost one hundred years later. The pioneering work of Childs *et al.* [26], from 2004, about modeling of the pipe failure in BOP proposes an analytical solution for the required cut force. Based on the Distortional Energy Theory (DTE) they assumed a pure and uniform shear state in the cross section of the pipe, with the shear force being proportional to the ultimate stress, σ_u , and the tubular cross-sectional area (S_t).

$$F_{DTE} = \frac{1}{\sqrt{3}} \sigma_u S_t \quad (2)$$

Although the ultimate force is proportional to the product of the ultimate strength (σ_u) and the tubular cross-sectional area (S_t), the DTE model overestimated the force due to the 3D stress state induced by the ram contact and stress concentrations. Moreover, the model is independent of shear ram geometry and external loadings applied in the tubular, limiting practical applications. In [26], the authors proposed calibration curves and interpolations, extrapolating results to other tubulars sizes, although they were unable to extend the results to other materials or ram geometries that were not previously tested. However, corrections based on empirical linear correlations with experimental results were proposed as shown in Figure 14. Such analytical model is still adopted by most of BOP manufactures.

Figure 14 - Pipe shear force obtained by experimental results x predicted by DET model

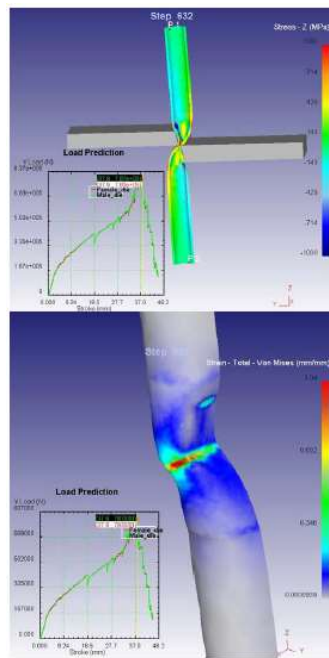


Source: Extracted from [26].

The motivation for a deeper understanding of the pipe cutting mechanism came with a relatively recent tragedy. In April 2010, at Macondo prospect located in Gulf of Mexico, a series of events culminated in a disaster where an oil spill took place in Deepwater Horizon platform. The BOP was not able to cut the drill string and close the well, when a blowout event was in course. The failure in BOP actuation was pointed as one of the main root causes of the tragedy, in terms of environmental and financial issues and human lives (11 workers lost their lives that day and a loss estimated in US\$ 82 billion was reported [27]).

In the same year, Telkin [12] provided the first known systematic study in BOP pipe shearing simulation using FEM. The work identified and studied the influence of the factors that interfere on the forces required by a shear ram to cut a pipe, namely the offset between rams, loads and centralization on the pipe. The numerical model is illustrated in Figure 15. Despite the use of the FEM approach to model the cut of the pipe, the author did not discuss material failure model, thus generating questionable conclusions.

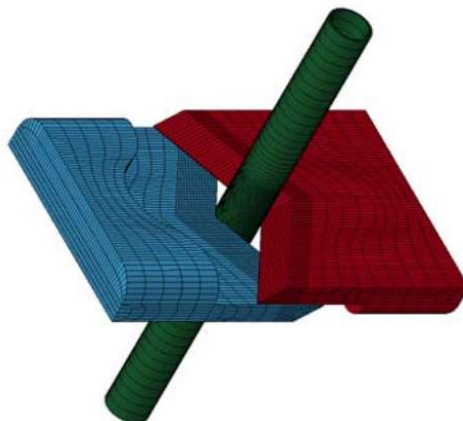
Figure 15 - Telkin (2010) FEM model and results



Source: Extracted from [12].

In 2012, Koustelos [28] presented the first discussion about material failure model applied to the pipe cut in BOP problem (Figure 16). The author applied the modified Mohr-Coulomb criterion developed in 2009 by Bao and Wierzbicki [29] with validated material parameters based on TRIP 690 and X70 steels, which are rarely used in drill strings in the Brazilian scenario.

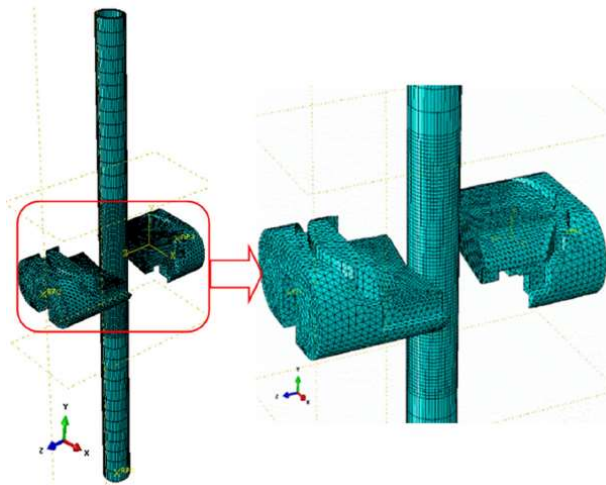
Figure 16 - Koutsolelos (2012) FEM model



Source: Extracted from [28].

In 2015, Han [3] developed a study in pipe cutting in BOP using an extended Johnson-Cook model calibrated by experimental tests. More recently, Liu et al. [30] reproduced the work from [28], by using the failure model proposed in [29] calibrated by a micromechanical approach (Figure 17). In 2018, McCleney et al. [31] also modeled the pipe cut of a BOP under flowing conditions using the Johnson-Cook material model, simulating a well shut in in a blowout condition concluding that it does not interfere relevantly in the cutting process.

Figure 17 - Liu (2017) FEM model



Source: Extracted from [3].

Castilho, in 2016, compared the ultimate force obtained from numerical and analytical models. The author demonstrated that analytical models tend to overestimate the shear forces for most of pipes used in oilfields. According to the author, analytical models are not accurate to represent the effects of nonlinearities, such as hardening and large displacements [32].

Also, in 2016, the Chemical Safety Board (CBS) released a report which concluded that the precipitating cause of Macondo incident was the inability of the shear ram to cut the pipe, close it and seal the wellbore [27]. Based on a sensibility analysis using FE simulations under different boundary conditions of pipe cut in BOP performed by Tulimilli et al, the report pointed out that this failure occurred due to compression and buckling on drill string and its offset from the BOP bore center [33], [34]. Morales in 2020 proposed a damage model for AISI 4340 steel, based on numerical and experimental tests that can potentially be used in tubulars for subsea drilling applications [35]. The summary of all works

performed on the BOP cutting problem found in literature is listed in Table 1 and Table 2.

Table 1 - Summary of works done in pipe cutting in BOP problem found in literature

#	Author	Year	Failure criterion	Analysis	Tube	Material	Loads	Principal results
1	Childs et al.	2004	DET	Analytical	Various	Various	Only gravity	1 - Linear relation between force and cross-sectional area; 2 - DET model needs correction curves to be used.
2	Telkin	2010	?	FEM (Deform 3D)	Various	S-135	Various	1 - FEM model provides more accurate result than DET; 2 - Sensibility analysis of the principal factors that contribute to the shear force: loads (traction and compression in the pipe), tool clearance.
3	Koutsolelos	2012	B-W	FEM (Abaqus)	5 1/2"	X-70	Various	1 - Formal definition of FE model and failure criterion, using experimental-based calibration; 2 - Stress states during the cutting procedure; 3 - Sensibility analysis to determine the optimal shape of "V" shear blades.
4	Tulimilli et al.	2014	?	FEM (Abaqus)	3 1/2" 13,3ppf	S-135	Various	1 - Analysis of the influence of different ram geometries on the pipe cutting force; 2 - Sensitivity analysis of the cutting force to different pipe positioning; 3 - Pipe buckling increases up to 40% the necessary force to cut pipe; 4 - Negligible effects of flow in the tubular cutting force.

Source: Personal file.

Table 2 - (Cont.) Summary of works done in pipe cutting in BOP problem found in literature

#	Author	Year	Failure criterion	Analysis	Tube	Material	Loads	Principal results
5	Han	2015	J-C	FEM (Abaqus)	5" 25,6ppf	S-135	Only gravity	1 - Sensibility analysis to determine the optimal shape of "V" shear blades; 2 - Comparison between plastic deformation in the rams predicted by FEM and experiments; 3 - According to experiments, rams first deform the pipe and then cut it.
6	CBS	2016	N/A	N/A	5 1/2"	-	-	1 - Main causes of Macondo incident was inability to shear ram to cut pipe due to buckling and far of BOP center.
7	Castilho	2016	Max equivalent strain	FEM / Analytical	Various	E-75	Only gravity	1 - Comparison between analytical and FEM model, concluding that FEM is more accurate; 2 - Analytical models can't predict ductility with accuracy.
8	Liu et al.	2017	B-W (cell model)	FEM (LS-Dyna)	200mm x 10mm	TRIP 690	Only gravity	1 - The ram force applied in the pipe and the displacement in the pipe are compared for material models calibrated by B-W and micromechanical cell B-W model. 2 - Micromechanical model predicted accurate results using less experimental data.
9	McCleney et al.	2018	J-C	FEM (LS-Dyna)	6 7/8" 50ppf	S-135	Fluid-Structure Interactions (FSI), gravity	1 - The water hammer effects on the cutting force while flowing inside BOP bore is small compared to the forces required to cut the pipe

Source: Personal file

Hitherto, there has been no systematic study for API S-135 steel failure characterization. Although FEM simulations provided results coherent with experimental observations, the pipe cut mechanism is not completely

understood, as indicated in [31]. In order to deepen the understanding of all BOP process of cutting the drill string, the material failure behavior must be better analyzed, in a likely stress state range. It should also be noted that the previous studies reached some contradictory conclusions about the effects of boundary conditions in the required force to cut a 5.5" 21.9ppf drill pipe in BOP, probably due to the limited number of simulations or a difference in the adopted failure model. Table 3 summarizes the conclusions of the main works found in the literature, relating the effect of the force boundary conditions and their ranges on the cutting force.

Table 3 - Effect of boundary conditions in the tubular cutting force

Author	Tube Material	Boundary Condition	Range	N_{sim} *	Effect on force to cut pipe
Telkin (2010)	API S-135	Traction	22,1ton (216.7kN)	3	Decrease 3% to a threshold
		Compression	47,7ton (467.8kN)	3	Increase 8%
		Indenter offset	0,6mm	6	Minimum at 0,2mm (decrease 7%)
Koutsolelos (2012)	TRIP 690	Traction	?	2	Decrease 23%
		Compression	?	2	Decrease 64%
		Internal pressure	100psi (689.5kPa)	2	No effect
Tulimilli (2014)	API S-135	Traction	100kips (444.8kN)	1	Decrease 10%
		Compression	100kips (444.8kN)	1	No effect
		Buckling	?	1	Increase ~40%
		Tubular decentralization	100%	1	Decrease ~40%

* N_{sim} refers to the number of numerical simulations performed

Source: Personal file.

3.2. Material model

As extensively discussed here, numerical simulation is an important tool to analyze and understand the BOP action in real conditions. The process evolves progressive plastification with hardening, material deterioration and failure of the tube. Therefore, the material model is crucial in the definition of the virtual model.

In general, for isotropic behavior, material models are usually expressed in terms of the Cauchy stress tensor invariants. Thus, a brief discussion about the invariants is presented before the discussion about plasticity and failure models.

3.2.1. Stress invariants

The stresses state in an elementary volume can be defined as the Cauchy's stress tensor [36],

$$\boldsymbol{\sigma} = \begin{bmatrix} \sigma_{11} & \sigma_{12} & \sigma_{13} \\ \sigma_{21} & \sigma_{22} & \sigma_{23} \\ \sigma_{31} & \sigma_{32} & \sigma_{33} \end{bmatrix} \quad (3)$$

Once stresses must also satisfy Newton's second Law, the stress tensor is symmetric and positive definite. For every positive definite stress state, it is possible to rotate the coordinate system and, in particular, there is one in which the shear stresses are null, namely the principal (main) axis. This main coordinate system is found by means of eigenvalues and eigenvectors of Cauchy's stress tensor. Using index notation,

$$(\sigma_{ij} - \lambda \delta_{ij})n_j = 0 \quad (4)$$

where λ are the eigenvalues or principal stresses, n_j are the corresponding eigenvectors, or principal directions and δ_{ij} is the Kronecker function, defined as,

$$\delta_{ij} = \begin{cases} 1, & \text{if } i = j \\ 0, & \text{if } i \neq j \end{cases} \quad (5)$$

The characteristic Equation (6) is the non-trivial solution of the eigenvalue problem, which is derived from the determinant of Equation (4),

$$\lambda^3 - I_1 \lambda^2 + I_2 \lambda - I_3 = 0 \quad (6)$$

where I_1 , I_2 , and I_3 are the invariant scalars of the Cauchy's stress tensor. These invariants are defined as,

$$I_1 = \sigma_{ii} \quad (7)$$

$$I_2 = \frac{1}{2}(I_1^2 - \sigma_{ij}\sigma_{ij}) \quad (8)$$

$$I_3 = \det(\sigma_{ij}) \quad (9)$$

From Equation (6) the solutions for λ are the principal stresses $\sigma_1 \geq \sigma_2 \geq \sigma_3$. It is a common practice to express the stress tensor into two components, namely the hydrostatic or dilatational (σ_m) and deviatoric (s) parts. The deviatoric stresses results from the subtraction of the hydrostatic part of the stress tensor,

$$s_{ij} = \sigma_{ij} - \sigma_m \delta_{ij} \quad (10)$$

or,

$$\boldsymbol{\sigma} = \sigma_m \begin{bmatrix} 1 & 0 & 0 \\ 0 & 1 & 0 \\ 0 & 0 & 1 \end{bmatrix} + \begin{bmatrix} s_{11} & s_{12} & s_{13} \\ s_{21} & s_{22} & s_{23} \\ s_{31} & s_{32} & s_{33} \end{bmatrix} \quad (11)$$

Where σ_m is the hydrostatic pressure defined as,

$$\sigma_m = \frac{\sigma_{ii}}{3} = \frac{I_1}{3} \quad (12)$$

Hydrostatic component of the tensor causes only volumetric deformations on the body while the deviatoric stresses are responsible for isovolumetric shape deformations. Material models are also based on invariants of the deviatoric part of the stress tensor, which are defined as,

$$J_1 = 0 \quad (13)$$

$$J_2 = \frac{1}{2}s_{ij}s_{ij} = \frac{1}{3}(I_1^2 - 3I_2) \quad (14)$$

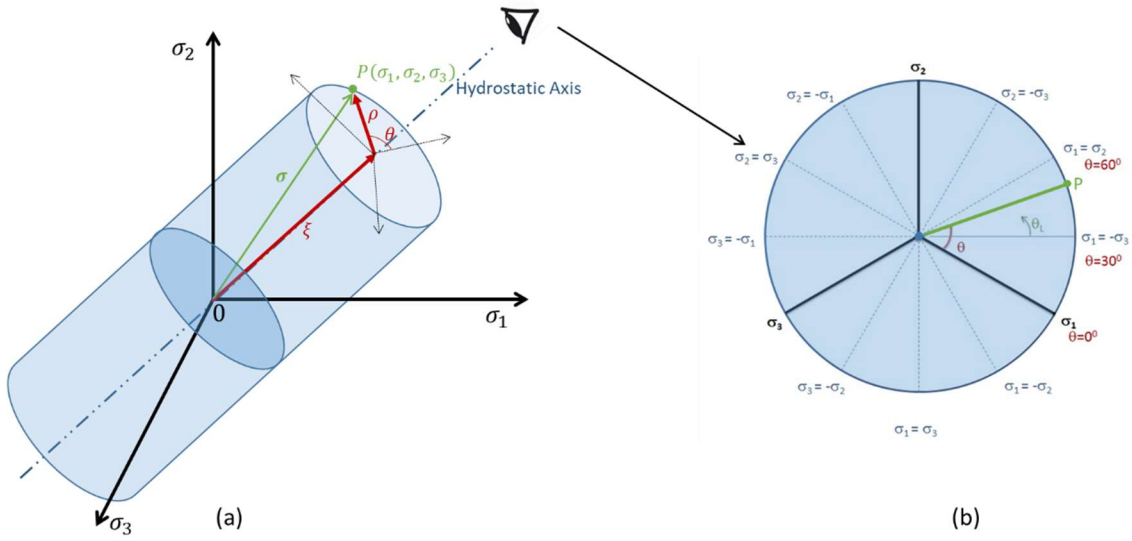
$$J_3 = \frac{1}{3}s_{ij}s_{jk}s_{ki} = \frac{1}{27}(2I_1^3 - 9I_1I_2 + 27I_3) \quad (15)$$

It should be noted that the same analysis methodology can be applied to the strains tensor.

3.2.2. Measurements derived from invariants

It is more convenient to visualize the stress state σ in principal stress space, known as Haigh-Westergaard space, in the cylindrical coordinate system, expressed in terms of the radius ρ , the angle θ_L and the distance from the origin along the cylindrical axis, ξ_L .

Figure 18 - Stress state represented in Haigh-Westergaard plane



Source: Personal file.

The cylindrical coordinate system components (ξ_L, ρ, θ_L) is illustrated in Figure 18 and defined as,

$$\rho = \sqrt{2J_2} \tag{16}$$

$$\xi_L = \frac{\sqrt{3}}{3} I_1 = \sqrt{3} \sigma_m \tag{17}$$

$$\theta_L = \frac{1}{3} \cos^{-1} \left(\frac{3\sqrt{3}}{2} \frac{J_3}{J_2^{3/2}} \right) \tag{18}$$

The angle θ_L is called the Lode angle parameter, where $0 \leq \theta_L \leq 1/3$ and ξ_L is the length along Haigh-Westergaard cylindrical axis. The radius ρ is related to the well known von Mises equivalent stress (σ_{eq}),

$$\sigma_{eq} = \left(\frac{3}{2} s : s \right)^{\frac{1}{2}} = \sqrt{\frac{3}{2}} \rho = \sqrt{3} J_2 \tag{19}$$

The ratio between hydrostatic pressure (σ_m) and the von Mises equivalent tension (σ_{eq}) is defined as stress triaxiality (η) which is related to some material failure criteria,

$$\eta = \frac{\sigma_m}{\sigma_{eq}} = \frac{1}{3\sqrt{3}} \frac{I_1}{\sqrt{J_2}} \quad (20)$$

where $-\infty \leq \eta \leq \infty$.

Lode angle parameter (θ_L) is a measure of the second principal stress *locus* in relation to the first and third principal stresses, which indirectly characterizes the stress state. There are several variations of Lode angle parameter in Equation (18). For example,

$$L_{Bao} = 1 - \frac{6L}{\pi} \quad (21)$$

where L is the so called Lode angle with $-1 \leq L_{Bao} \leq 1$. This definition is widely used in the literature in failure models, for example, in Bao and Wierzbicki (2008) [37], Barsoum and Faleskog (2011) [38], Danas and Castañeda [39], among others. Particularly, Xue (2007) [40] defined the following relation for Lode parameter,

$$L_{Xue} = \text{atan} \left(\frac{1}{\sqrt{3}} \mu \right) \quad (22)$$

where μ is the Lode parameter $-1 \leq \mu \leq 1$,

$$\mu = \frac{2\sigma_2 - \sigma_1 - \sigma_3}{\sigma_1 - \sigma_3} \quad (23)$$

Such equation is valid for $\sigma_1 \geq \sigma_2 \geq \sigma_3$. The influence of triaxiality, hydrostatic pressure and Lode angle in the plasticity, damage and failure of ductile materials has been extensively studied in Brünig et al. (2008) [41], Driemeier et al. (2010) [42], Barsoum and Faleskog (2011) [38], Danas and Castañeda (2012) [39], Kiran and Khandelwal (2014) [43], Xiao et al. (2019) [44]. Particularly, experimental tests at different loading conditions are explored in Wierzbicki et al. (2005) [45],

Gerke, Adulyasak and Brünig (2017) [46], Brünig, Gerke and Tix (2018) [47] and in Brünig, Gerke and Schmidt (2016, 2016a, 2018) [48], [49], [50].

3.2.3. Johnson-Cook plasticity model

Briefly, the empirical Johnson–Cook (1983) (J–C) model was chosen as the constitutive plasticity model. It is a particular type of Mises plasticity model with uncoupled analytical forms of the hardening law, rate and temperature dependence. It is widely used in many engineering applications because of its simplicity due to decoupling effects, which allows calibration of variables parameters that interfere on material hardening [51]. When compared to other plasticity models such as GTN model, J-C model provides more accurate results for large deformations. Parameters of the J-C model for many different materials are also available in the literature [52]. According to this model, the yield stress is determined by the formula,

$$\sigma_y = (C_1 + C_2 \bar{\epsilon}^{p C_3}) (1 + C_4 \ln \dot{\epsilon}^*) (1 - C_5 \theta^*) \quad (24)$$

where C_1 up to C_5 are materials parameters and are determined by experimental results: C_1 is the initial yield stress, C_2 is the hardening modulus, C_3 is the strain-hardening exponent, C_4 is the strain rate dependency coefficient, C_5 is the thermal softening coefficient. $\dot{\epsilon}^*$ is the dimensionless strain rate defined as,

$$\dot{\epsilon}^* = \frac{\bar{\epsilon}^p}{\dot{\epsilon}_0} \quad (25)$$

Where $\bar{\epsilon}^p$ is the plastic strain rate and $\dot{\epsilon}_0$ is a reference strain rate, usually 0.001s^{-1} . θ^* is the homologous temperature [53] defined as,

$$\theta^* = \frac{T-T_0}{T_m-T_0} \quad (26)$$

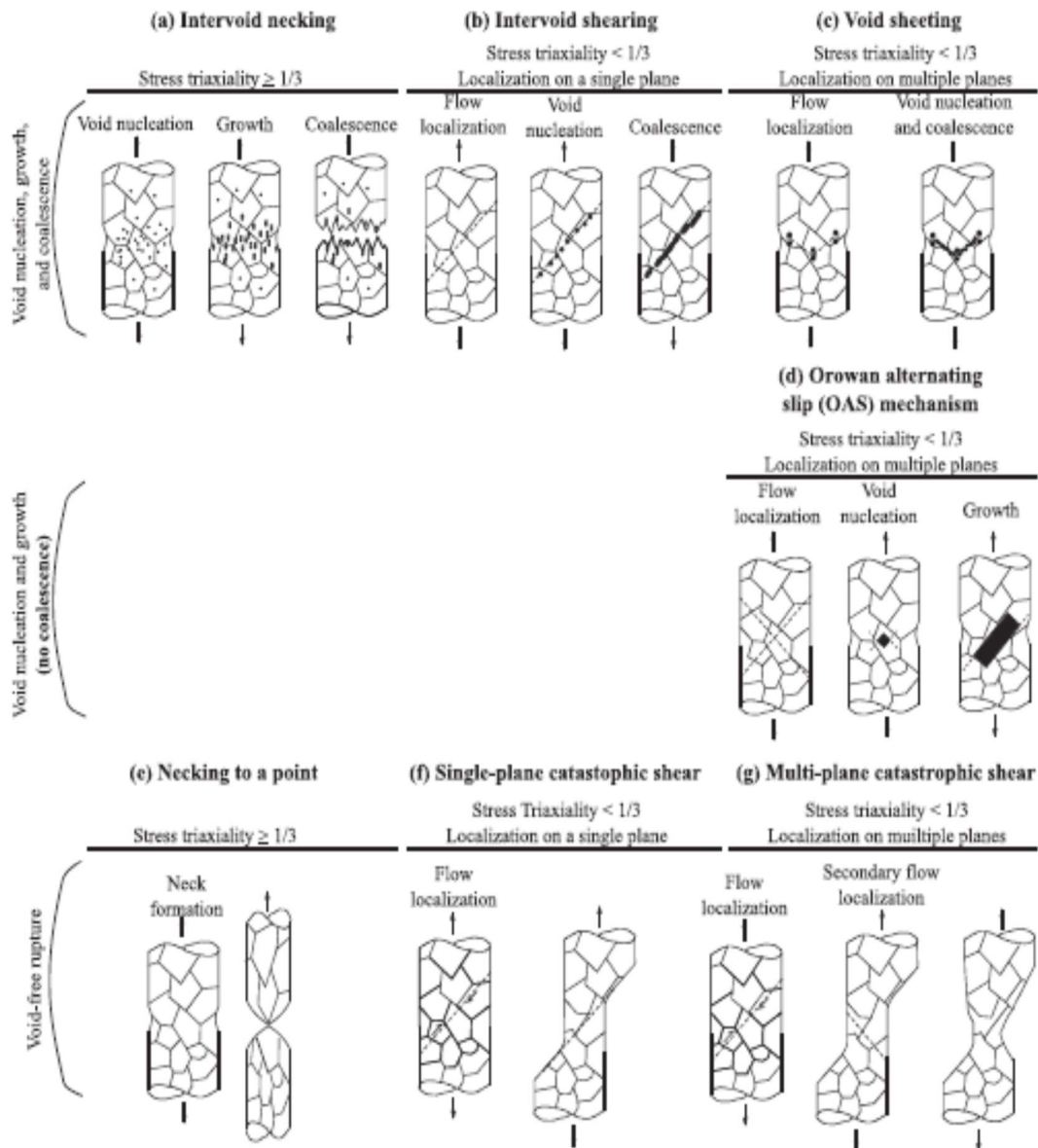
where the quantities T , T_m and T_0 are the local point temperature, material melt temperature and room temperature (25°C) respectively. It is assumed that the problem in focus can be considered quasi-static and adiabatic, the strain rate and temperature sensitivity parameters are neglected, resulting in the reduced form of J-C model for flow stress in plasticity,

$$\sigma_y = C_1 + C_2(\bar{\epsilon}^p)^{C_3} \quad (27)$$

3.2.4. Failure in ductile materials

The knowledge of the stress state which precedes the failure is essential to understand phenomenological changes in the material microstructure. The ductile failure, in its essence, begins with the growth of existing voids in the body and the nucleation of new voids close to inclusions, and, in more advanced stages, the process of coalescence either by micro stresses or by shearing between voids. It was known that the first was dominated by stress triaxiality and only recently it has been pointed out in the literature that the Lode angle plays an important role to model shear band mechanism for relatively low triaxialities [54] [55] [56] [57] [58]. A detailed study of failure modes in ductile material was performed by Noell et al [59]. They distinguished seven different polycrystalline mechanisms that govern ductile failure (Figure 19), despite being the two known traditional mechanisms, which are also related to the stress state at failure locus.

Figure 19 - Ductile polycrystalline metals failure mechanism proposed by NOELL et al (2018)



Source: [59]

There are essentially three types of ductile failure models: micromechanical, phenomenological and continuum damage mechanics. Failure models also can be either coupled or uncoupled with the voids (damage) effects over the material mechanical properties. Coupled models consider softening in material stiffness due to voids growth and tend to be more realistic to represent material behavior. Uncoupled models, on the other hand, does not account for the material softening and, consequently, are simpler for numerical analysis and, in general, present more conservative results [60]. That is the reason why,

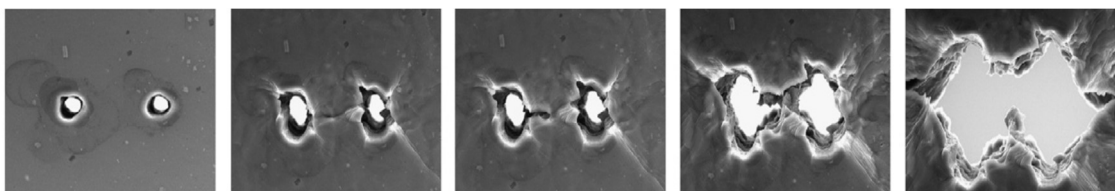
despite their shortcomings, uncoupled models are still frequently used in the literature.

3.2.5. Micromechanical models

Micromechanical models are concerned to analyze how microscale void shapes influences on material mechanical behavior in macroscale. Based on analytical models, such models are constituted by a single void involved by the material matrix substrate on a volume element in micro scale [61]. The pioneering studies of McClintock (1968) [54], Rice and Tracey (1969) [56], Hancock and Mackenzie (1976) [62] concluded that failure in ductile materials is due to nucleation and growth of voids accompanying large plastic flow and it is directly influenced by stress triaxiality.

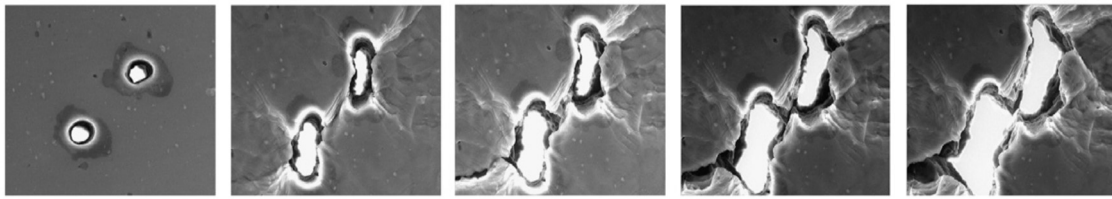
When voids are large enough they coalesce. In this phenomenon, the voids concatenate with their neighbors which can occur by necking (Figure 20) or by shear bands formations (Figure 21) depending on the stress state. A schematic representation of those effects is illustrated in Figure 22 and the main micromechanical models are resumed in Table 4.

Figure 20 - Necking of ligament between two voids



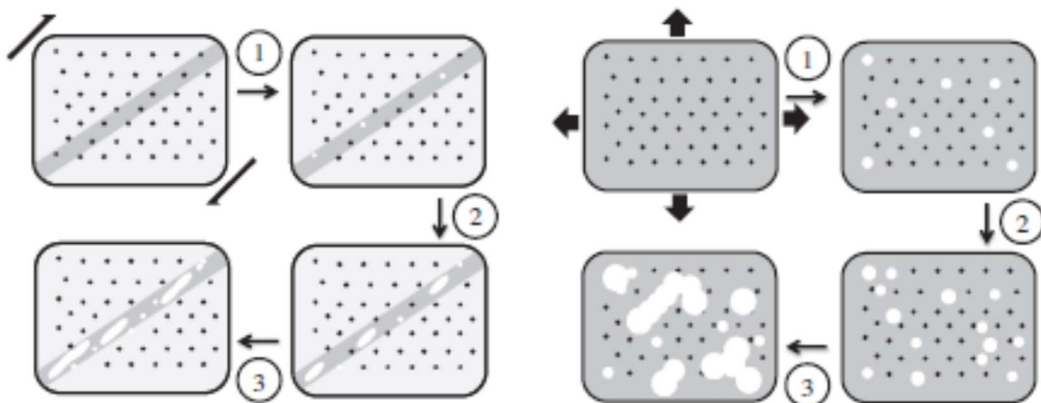
Source: Extracted from [63].

Figure 21 - Shear bands between two voids



Source: Extracted from [63].

Figure 22 - Representation of fracture due to shearing (left) and necking coalescence due to spherical growth of voids (right)



Source: Extracted from [64].

Table 4 - Failure models for ductile materials

Model	Year	Hypothesis	Failure criterion
McClintock [54]	1968	Similar to Rice criterion, however it considers a cylindrical void ideally distributed in identical cells	Failure occurs when the boundary of a void reaches the boundary of a cell.
Rice and Tracey [56]	1969	Considers the growth of a perfect spherical void in a perfect elastic matrix.	Failure occurs when the rate of void growth is higher than the strain growth of the elastic matrix.
Gurson [55]	1977	Consider the growth of a perfect spherical void in an elastic-plastic matrix.	Failure is associated to the matrix yield condition.

Source: Adapted from [60].

Since various important mechanisms occur at the atomic scale (dislocations or grain boundaries) and microscale (hard precipitates or voids), models such as those presented in Table 4 are essential to enhance the general understanding of damage and ductile failure process. Nowadays, numerical simulations of unit-cells with single voids are still discussed in the literature as, for example, Brüning, Gerke and Tix (2018) [47]. However, these models have significant simplifications and are not applicable when modeling real structures. Indeed, multiscale modelling for neutron induced embrittlement in metals have been studied in the literature as interesting alternatives to model complex phenomena related to lower scales.

3.2.6. Phenomenological models

Phenomenological failure model is a macroscopic theory. It provides the most significant parameters to predict failure, based on internal variables not directly derived from its mechanism in microscale. The pioneer models were used to relate material sudden failure with a threshold of equivalent stress or strain. Despite its simplicity and accurate results in some cases (especially in impact and ballistic simulations), they are not accurate enough to capture the material deterioration, which is critical in some situations such as fatigue. The most well-known sudden failure models are summarized in Table 5, in which some will be detailed due to its importance to this thesis.

Table 5 - Sudden failure models

Sudden failure model	Year	Measured variable
Max shear stress (Rankine)	1864	Shear stress.
Max equivalent stress (Von Mises)	1913	Equivalent shear stress
Mohr-Coulomb	1914	Combination of normal and shear stress.
Freudenthal	1950	Equivalent plastic work
Max Equivalent plastic strain (MaxDPE)	1966	Equivalent plastic strain
Cockcroft-Latham (C-L)	1968	Plastic work associated to traction (higher principal stress)
Johnson-Cook (J-C)	1985	Equivalent accumulated plastic strain (function of triaxiality, temperature and strain rate).

Source: Adapted from [60].

3.2.6.1. Maximum equivalent plastic strain (MaxDPE)

According to this failure criterion, a defined effective plastic strain is used as a threshold to define material failure. The effective plastic strain ($\bar{\varepsilon}^p$ or PEEQ) is a measurement of the total plastic strain in all principal directions ε_{ii}^p . It is a simple model and is widely used in the main FEM software. Material failure occurs when $\bar{\varepsilon}^p \geq \bar{\varepsilon}_f^p$, in which,

$$\bar{\varepsilon}^p = \frac{1}{\sqrt{3}} \sqrt{2 \left(\varepsilon_{11}^{p\ 2} + \varepsilon_{22}^{p\ 2} + \varepsilon_{33}^{p\ 2} \right)} \quad (28)$$

where $\bar{\varepsilon}_f^p$ is a limit for the equivalent plastic strain.

3.2.6.2. Johnson-Cook fracture criterion

Johnson-Cook failure model (J-C) is widely used due to its simplicity and empirical basis [53]. Moreover, the material parameters can be found in the open literature for many different materials. According to this failure criterion, the equivalent strain to fracture ($\bar{\varepsilon}_f^p$) expression is given by,

$$\bar{\varepsilon}_f^p = (D_1 + D_2 e^{D_3 \eta}) (1 + D_4 \ln \dot{\bar{\varepsilon}}^*) (1 + D_5 \theta^*) \quad (29)$$

where D_1 to D_5 are material constants to be determined experimentally, η is the stress triaxiality, $\dot{\bar{\varepsilon}}^*$ is the dimensionless effective strain rate and θ^* is the homogenous temperature as defined in Equation (29). Nonetheless, J-C model can also be calibrated to provide the strain at damage onset, namely $\bar{\varepsilon}_0^p$. In this approach, the material is dominated by the continuum damage mechanics, once damage is triggered [45].

3.2.6.3. Mohr-Coulomb fracture criterion and extensions

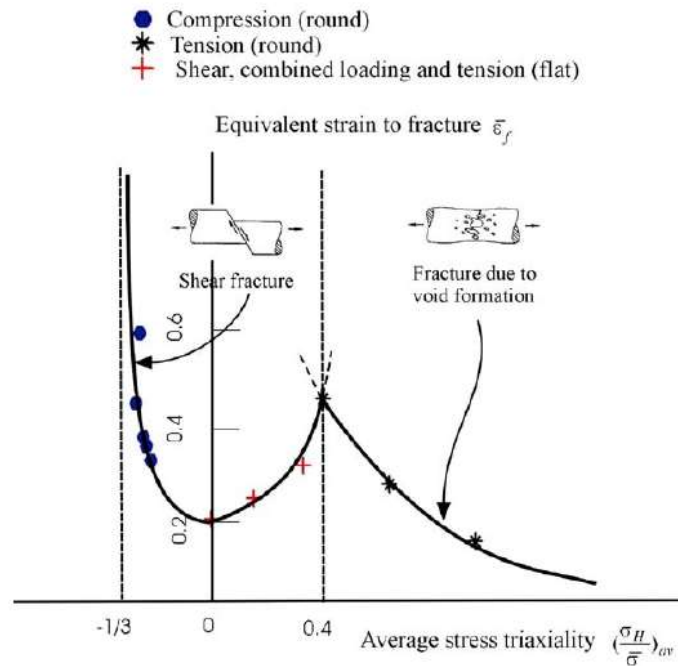
The original Mohr-Coulomb criterion (M-C) is often used in rock and soil mechanics. According to this model, fracture will occur when a combination of normal and shear stress is reached in the fractured plane,

$$(\tau + D_1\sigma_n)_f = D_2 \quad (30)$$

where the constants D_1 and D_2 are known as the tangent of the internal friction angle and cohesion force respectively, τ and σ_n are the shear and normal stress at the fracture surface respectively.

Although the existing failure models could predict accurately the strain to fracture results for high stress triaxiality (characterized by voids necking), they were unable to predict failure in low triaxialities due to shear band failure mechanism, as concluded by Bao [65] (Figure 23). Bai and Wierzbicki (2009) [29] proposed a modification in the M-C model, known as B-W or E-MC, to efficiently consider shear and tensile failure in the same model. Ever since, has become a reference model despite its complexity.

Figure 23 - Dependence of the equivalent strain to fracture on the stress triaxiality, for testing performed with plain stress specimens



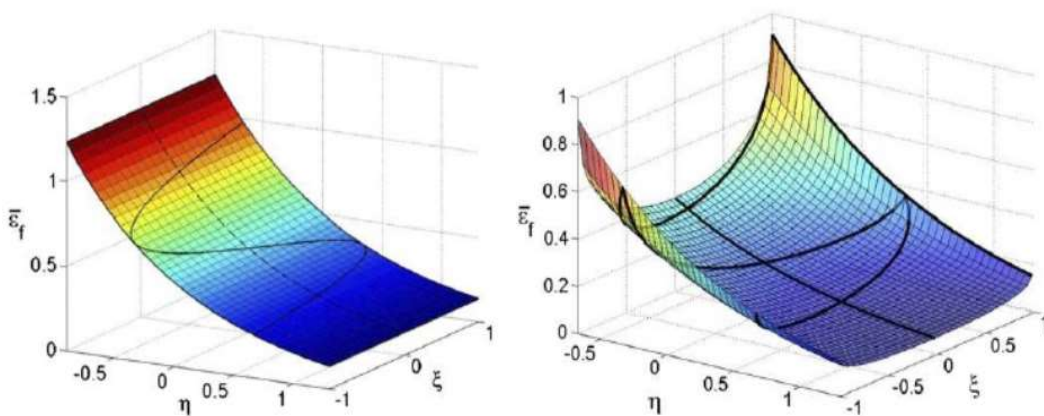
Source: Extracted from [65].

The B-W model is based on a change in stress coordinates in M-C model. Instead describing the material failure condition in terms of shear stress (τ) and normal stress (σ_n) as proposed by the original M-C criterion, the B-W model relates stresses at failure with triaxiality (η) and the Lode angle (ξ). With the use of a generalized hardening rule to relate stress with strain, the obtained model has a total of eight parameters to be calibrated by experiments (two of them related to fracture and the other six to plasticity). However, assumptions can be made to simplify the formulation and B-W criterion to,

$$\bar{\varepsilon}_f^p = D_1 \left\{ D_2 \cos\left(\frac{\theta_L \pi}{6}\right) + D_3 \left[\eta + \frac{1}{3} \sin\left(\frac{\theta_L \pi}{6}\right) \right] \right\}^{-D_4} \quad (31)$$

where D_1 up to D_4 are material parameters to be calibrated with fracture tests, θ_L and η are the Lode angle and the stress triaxiality, respectively, as defined in section 3.2.2. A comparison of J-C with B-W models is shown in Figure 24. The first relies merely on stress triaxiality while the second also depends on Lode angle, whose effect is more pronounced at low levels of triaxiality. The results obtained by Bao (2004) [65] were explained by the inclusion of Lode effect in B-W model.

Figure 24 – Comparison of fracture strain predicted by Johnson-Cook (1985) and Bai-Wierzbicki (2009) models



Source: Extracted from [37].

In the meanwhile, Nahshon and Hutchinson used weight functions approach to include the Lode effect in the Gurson model, (N-H) reaching similar

results as the B-W model [66]. Dunand and Mohr [67] compared the fracture results of several specimens over a wide range of Lode angle and triaxiality predicted by Modified Mohr-Coulomb (B-W) criterion to the Nahshon-Hutchinson (N-H) criterion. They concluded that, despite the B-W model being less physically and more empirically based than the N-H criterion, it provides more precise results. Malcher [68] compared the predicted fracture of aluminum alloy 2024-T351 by phenomenological model [37], damage approach [69] and micromechanical model [70] concluding that all of them have limitations and need to be improved for different stress states and, consequently, different mechanisms of failure [64].

Indeed, the addition of more complex parameters in the constitutive models, to correct deviations of experimental results, demands more and more sophisticated tests for calibration. This conclusion confirms that the failure model used in numerical simulations must be suitable to the particular failure mechanism involved and coherent with the stress state in the failure locus. However, as will be shown later in this thesis, it turns out that in modelling the shear band Lode angle is not significant for the stress states reached in the cut of the pipe. In this way, more complete failure models, as Hyperbolic functions regarding stress triaxiality and symmetric to normalized Lode parameter proposed by Wu et al (2017) [71], can be simplified to the J-C failure model in which ductility depends only on stress triaxiality and require less experimental tests to calibrate the parameters.

$$\bar{\epsilon}_D^p = (D_1 e^{-D_2 \eta} - D_3 e^{-D_4 \eta}) \theta_L^2 + D_5 e^{D_6 \eta} \quad (32)$$

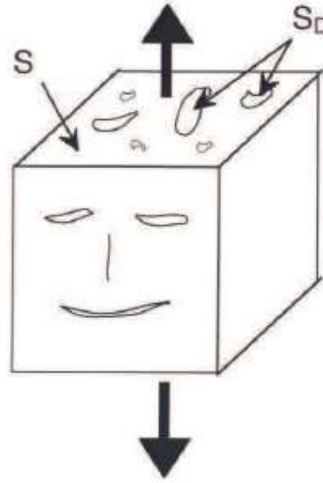
where, D_1 to D_6 are positive material parameters and θ_L is the Lode parameter.

This conclusion confirms that the failure model used in numerical simulations must be suitable to the particular failure mechanism involved and coherent with the stress state in the failure locus. Particularly of interest in this thesis, as will be shown later, the Lode angle is not significant for the stress states reached in the locus of initiation of failure, which triggers the pipe cut. In this case, the model in Equation (32) can be simplified to the J-C failure model presented in Equation (29), requiring less experimental tests to calibrate the parameters.

3.2.7. Continuum Damage Mechanics models

Once voids nucleate in a material matrix, they get damaged by degradation of its stiffness. In 1958 L. Kachanov postulated the fundamentals of continuum damage mechanics by defining a continuous damage variable D_m ($0 \leq D_m \leq 1$) to measure such degradation [72]. This variable is defined as the ratio of voids in the projected cross-sectional area (S_D) to the nominal undamaged area (S_0) of the body subjected to the action of a load as illustrated in Figure 25,

Figure 25 - Effect of voids in a material matrix subjected to a load



Source: Extracted from [73].

$$S_0 = S + S_D \quad (33)$$

$$D_m = \frac{S_D}{S_0} = \frac{S_0 - S}{S_0} \quad (34)$$

Kachanov also conceptualized the effective stress ($\tilde{\sigma}$), which is derived from a homogenization of a stressed body containing cracks and voids. When comparing two similar bodies subjected to the same tensile force, being one internally voided and the other undamaged, Kachanov demonstrated that the effective stress should consider the reduction in the cross-sectional area due to voids, since they do not transmit the load. The author also concluded that if the

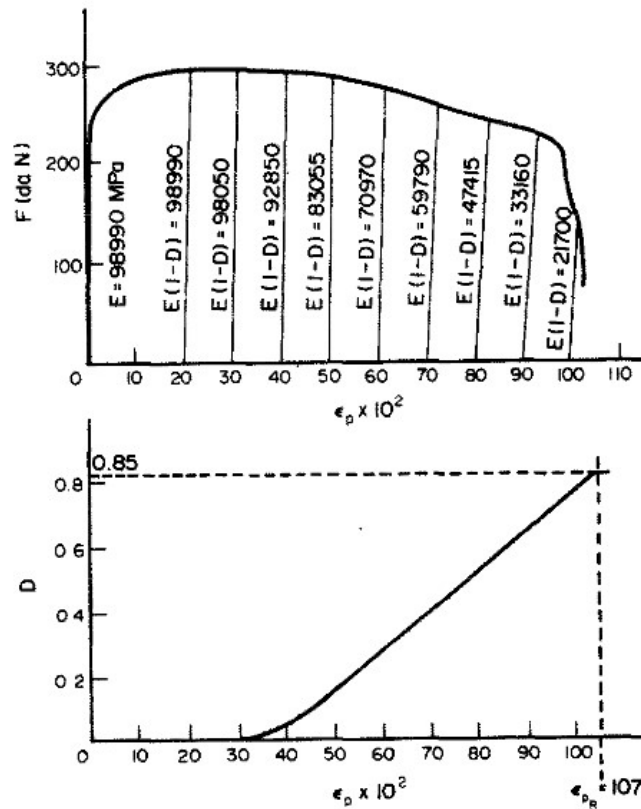
scale is large enough, the material is considered homogeneous. Thus, the definition for effective stress ($\tilde{\sigma}$) and effective stiffness (\tilde{E}) are, respectively,

$$\tilde{\sigma} = \frac{\sigma}{1-D_m} \quad (35)$$

$$\tilde{E} = E(1 - D_m) \quad (36)$$

Kachanov work was further continued by Lemaitre and Chaboche [74]. Lemaitre defined the Representative Volume Element (RVE), which is a statistical representation, by an averaging procedure, of typical material macro response. The RVE is the smaller volume in which the material properties are assumed homogenous and its size should be small enough to avoid smoothing of high gradients inside the control volume, although large enough to voids be considered homogeneously distributed. For metals and ceramics, a RVE should be of order of $(0.1\text{mm})^3$ [73]. Phenomenological damage may manifest by decreasing of the yield stress and by degradation of the material elasticity. Lemaitre [69] evidenced the change of copper elasticity modulus after loading with increments of plastic strains and unloading it, correlating this phenomenon with damage evolution (Figure 26). In his work, it is also observed that elasticity modulus remained unchanged until a determined plastic strain threshold, as predicted earlier by Kachanov.

Figure 26 - Effect of damage on the material matrix stiffness



Source: Extracted from [73].

In numerical implementation, a stress-state or strain-state model is used to define the damage initiation. Such model can be a plasticity or failure phenomenological model calibrated to indicate the strain at damage onset. Once damage is initiated, it follows an evolution law analogous to Miner Rule [75], where the damage is defined according to the cumulative formula,

$$D_m = \sum \frac{\Delta \epsilon^p}{\epsilon_f^p} \quad (37)$$

where $\Delta \epsilon^p$ is the increment of plastic strain and ϵ_f^p is the plastic strain at failure. In ABAQUS explicit FEM software by default, ϵ_f^p can be calculated in terms of Hillerborg energy required to open a unit area of crack (G_f) [76] [77]. G_f can be obtained from the experimental load-displacement curves of the material according to,

$$G_f = \int_0^{\bar{u}_f^p} \sigma_y d\bar{u}^p = \int_{\bar{\varepsilon}_0^p}^{\bar{\varepsilon}_f^p} \sigma_y L_e d\bar{\varepsilon}^p \quad (38)$$

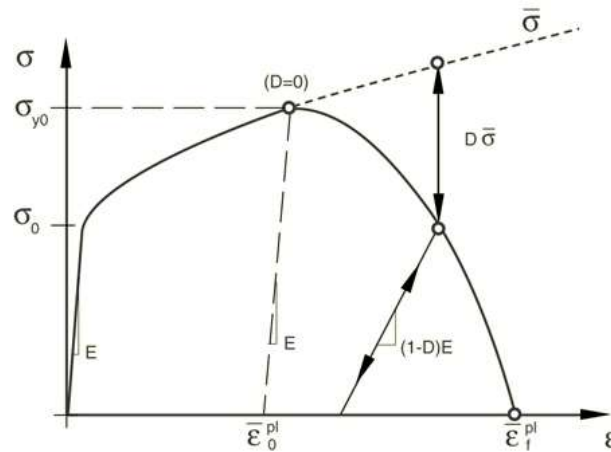
where \bar{u}^p is the local equivalent plastic displacement, σ_y is the material yield stress, $\bar{\varepsilon}^p$ is the local equivalent plastic strain, $\bar{\varepsilon}_0^p$ and $\bar{\varepsilon}_f^p$ are, respectively, plastic strain at damage onset and failure and L_e is the characteristic length of element. After damage initiation, the evolution of the equivalent plastic displacement and of the equivalent plastic strain are related by the characteristic length,

$$\dot{\bar{u}}^p = L_e \dot{\bar{\varepsilon}}^p \quad (39)$$

For damage-based models, failure of material occurs when damage reaches a critical value, *i. e.*, $D_m \geq D_{cr}$. The theoretical critical damage value is unitary, however experiments have found that material failure usually occurs at lower values [73].

Multiple failure models for materials can be used simultaneously to predict failure in structures under general loading conditions [78]. Regardless the model approach, it must be adherent to the structural failure mode. In this way, prior comprehension of the stress state in the failure is essential before choosing the failure model to be adopted.

Figure 27 - Stress x Strain curve with progressive damage evolution



Source: Extracted from [76].

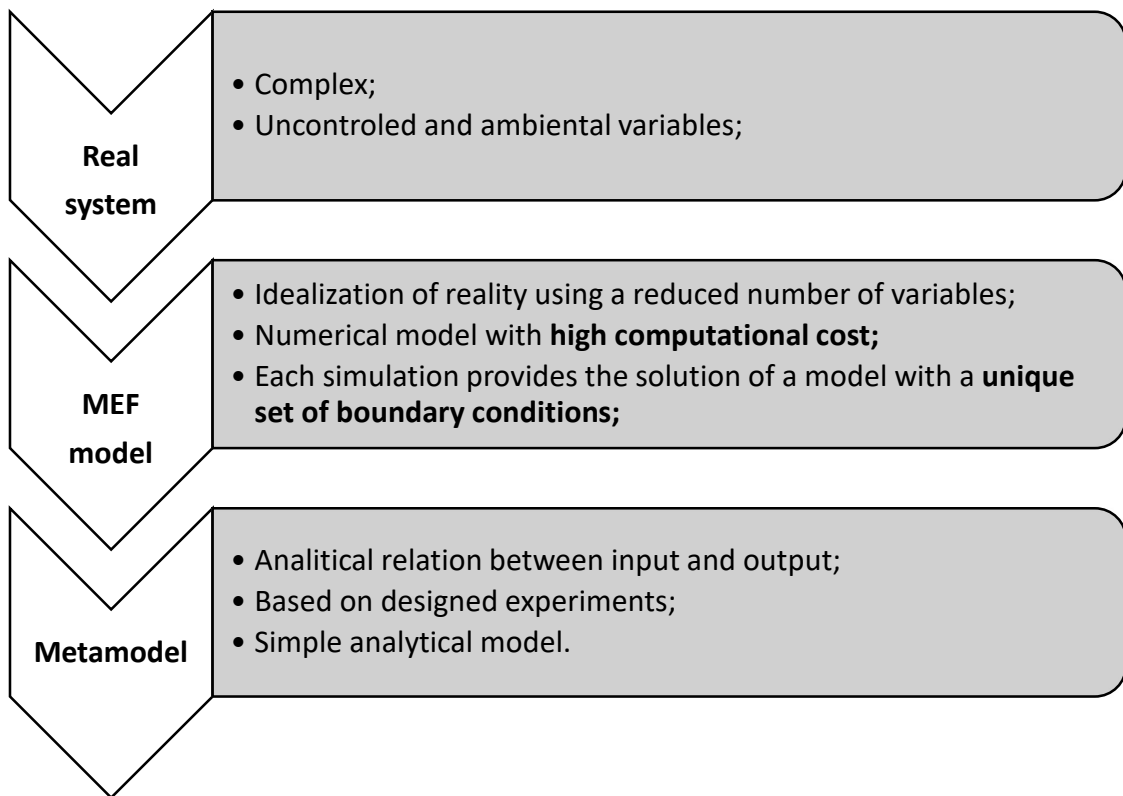
Plasticity, damage and failure are nonlinearities in the material behavior. Thus, it is unfeasible to find an analytical solution and a numerical method combined with interpolation techniques should be used.

3.3. Metamodels

Real mechanical systems may be too complex or even unfeasible to model analytically due to the geometry, large number of variables and/or initial conditions involved. Moreover, when the real system is strongly nonlinear, it is desirable to have a simpler model that relates the most important input variables to the system behavior. One efficient approach is the use of metamodels, which are based on the results of a sample of designed experiments.

Metamodel is roughly defined as *the model of the model* and it is used to simplify and reduce complexities of a real mechanical system. In a first approach, the real system is represented by a numerical model such as in FEM. Then, controlled simulations are performed on this model to generate results, which are statistically analyzed and jointed by interpolation methods [79]. The layers used to construct the metamodel are schematically illustrated in Figure 28.

Figure 28 - Layer used to build a metamodel



Source: Personal file.

3.3.1. Structural failure condition

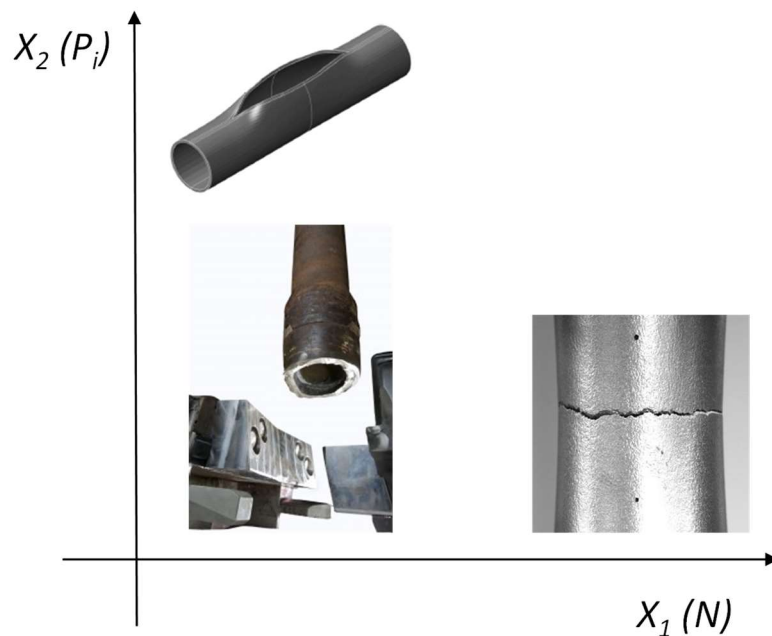
It is supposed that a structure is submitted to H independent project variables set $X = (X_1, X_2, \dots, X_H)$ in a single FEM simulation. Nevertheless, they will induce different stress states, which eventually leads to different failure modes. In numerical simulations, for a single X , FEM provides the stress state and failure mode as a consequence of the adopted material failure criterion. On the other hand, the metamodel is intended to stablish a direct link between different boundary conditions with a specific failure mode in the structure.

To develop the metamodel, it is supposed that the project variables are related to each other when failure mode m is reached. Thus, it is possible to describe structural response y and estimate its magnitude as a function of the project variables X by means of function $\phi_{f,m}(X)$,

$$y = \Phi_{f,m}(X_1, X_2, \dots, X_H) \quad (40)$$

which is assumed valid for is constant magnitude of X and same initial conditions for the structure, that is, undamaged and undeformed. Particularly in this study, we are interested on the BOP failure scenario, that is, the cutting of the well's drill pipe (structure) by the BOP rams. However, it can fail in different ways, depending on the magnitude of the boundary conditions. Figure 29 illustrates a generic tube failure, depending on the axial tension force (N) or internal pressure (P_i) levels.

Figure 29 - Representation of different failure modes on a tube cut in BOP as a function of internal pressure (P_i) and traction (N)



Source: Personal file.

A priori, the effect of boundary conditions on the stress state and, consequently, at a failure mode, is unknown. Some of them may even have null or negligible effect in structural failure. Indeed, it is supposed that the effect of project variables that leads to structural failure can be interpolated by a polynomial equation of order Q ,

$$\phi_{f,m}(\vec{X}) = \beta_0 + \sum_{k=1}^H \sum_{l=1}^Q \beta_{k,l} (x_k)^l \quad (41)$$

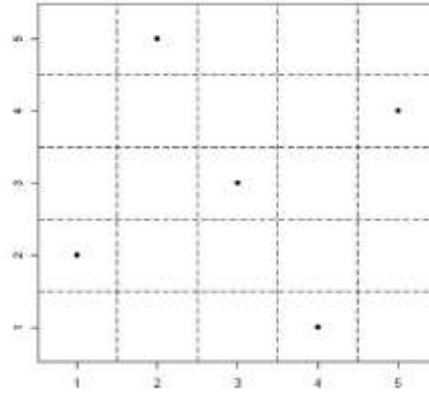
where k is the project variables index ($0 < k < H$), l is the polynomial exponent index ($l \in \mathbb{N} \mid 0 < l \leq Q$), $\beta_{k,l}$ are the adjustable metamodel coefficients and β_0 is the independent term for accounting the model bias.

3.3.2. Design of Experiment (DoE)

Initially, the real system is modeled in FEM and design variables are defined. In order to analyze the effects of a selected set of project variables on the system response, the acceptable range for them is established based on minimum and maximum expected operational values. Once this range is continuous, it is experimentally, and even computationally, unfeasible to test all possible combinations. Therefore, the use of an interpolation technique based on Design of Experiment technique (DoE) becomes necessary to reach optimized and reliable results based on the smallest possible set of input data.

There are several DoE techniques. The most popular are complete factorial, fractioned factorial, central composite designs (CCD), Box-Behnken, Plackett-Burman, Koshal, D-optimum, orthogonal matrices and Latin Hypercube Sampling (LHS) [16]. Particularly in the present study, Latin Hypercube Sampling (LHS) approach is chosen due to its versatility and fast convergence. The concept of the LHS algorithm is based on the definition of the "Latin Square", a $N_{sim} \times N_{sim}$ square grid containing the sample points, where the values must appear exclusively once in any given column or row, as illustrated in Figure 30.

Figure 30 - Example of sampling method in 5x5 space using Latin Square



Extracted from [16].

The LHS is a generalization of Latin Square to an arbitrary number of dimensions, where each input (design) variable X_k is partitioned into N_{sim} equally spaced subintervals. Then, each of the N_{sim} partitions of each input are sampled once, and randomly combined. The input variable subinterval is defined in the range,

$$\Delta X_k = X_{k_{max}} - X_{k_{min}} \quad (42)$$

where $X_{k_{max}}$ and $X_{k_{min}}$ are, respectively, upper and lower limits for each design variable X_k . In this thesis, a Bayesian variation of LHS is proposed. It is proposed to construct the metamodel in cycles, where the number of the DoE input data is doubled every iteration cycle and results from previous cycle are used in the analysis. To reach this purpose, the project variables intervals are discretized in N_{sim} parts for checking the convergence of the metamodel at each iteration cycle n ($n \in \mathbb{N} \mid n > 1$), selecting new values of X_k and using the previous ones. N_{sim} is related to iteration cycle by,

$$N_{sim} = 2^n + 1 \quad (43)$$

For each simulation i ($i \in \aleph \mid 0 < i \leq N_{sim}$), the DoE can be formulated as,

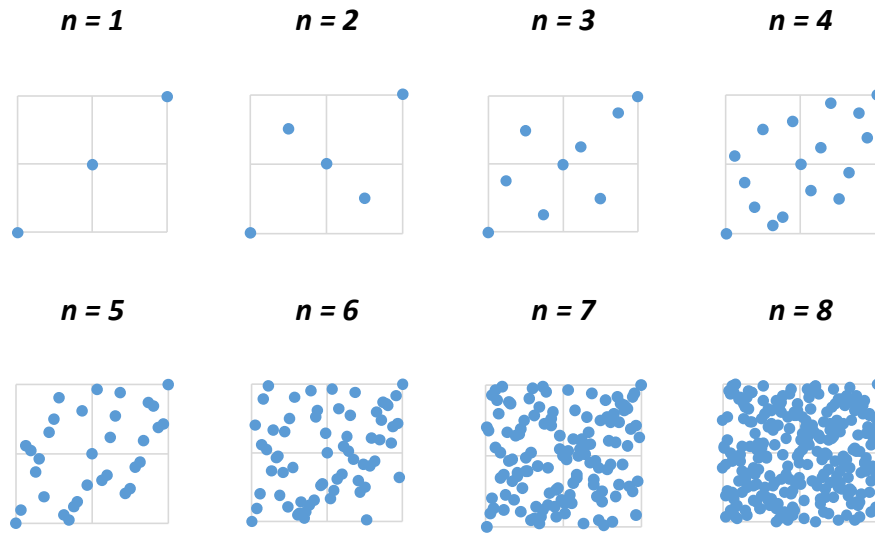
$$X_{k,i} = X_{k_{min}} + \frac{r_o(i,n)}{2^n} \Delta X_k \quad (44)$$

where, $X_{k,i}$ is the input variable of the i^{th} simulation performed, ΔX_k is the range between upper and lower variable limits and $r_o(i, n)$ is a function which returns a unique (*i.e.*, with no repetition) random odd number in the interval $0 < r_o(i, n) < 2^n$, with $2^{n-1} < i \leq 2^n$. For $n = 1$, the extremities and median of the variables in the domain are used as seed values,

$$\begin{cases} \vec{X}_0 = (X_{1_{min}}, X_{2_{min}}, \dots, X_{k_{min}}, \dots, X_{H_{min}}) \\ \vec{X}_1 = \left(\frac{\Delta X_1}{2}, \frac{\Delta X_2}{2}, \dots, \frac{\Delta X_k}{2}, \dots, \frac{\Delta X_H}{2} \right) \\ \vec{X}_2 = (X_{1_{max}}, X_{2_{max}}, \dots, X_{k_{max}}, \dots, X_{H_{max}}) \end{cases} \quad (45)$$

It should be noted that using this approach, the average value for the variables is always located in the median of their domain. For different values of n iteration cycle levels, the domain space filling of two variables using the proposed DoE is illustrated in Figure 31.

Figure 31 – Space filling illustration of inputted values for a two variables domain



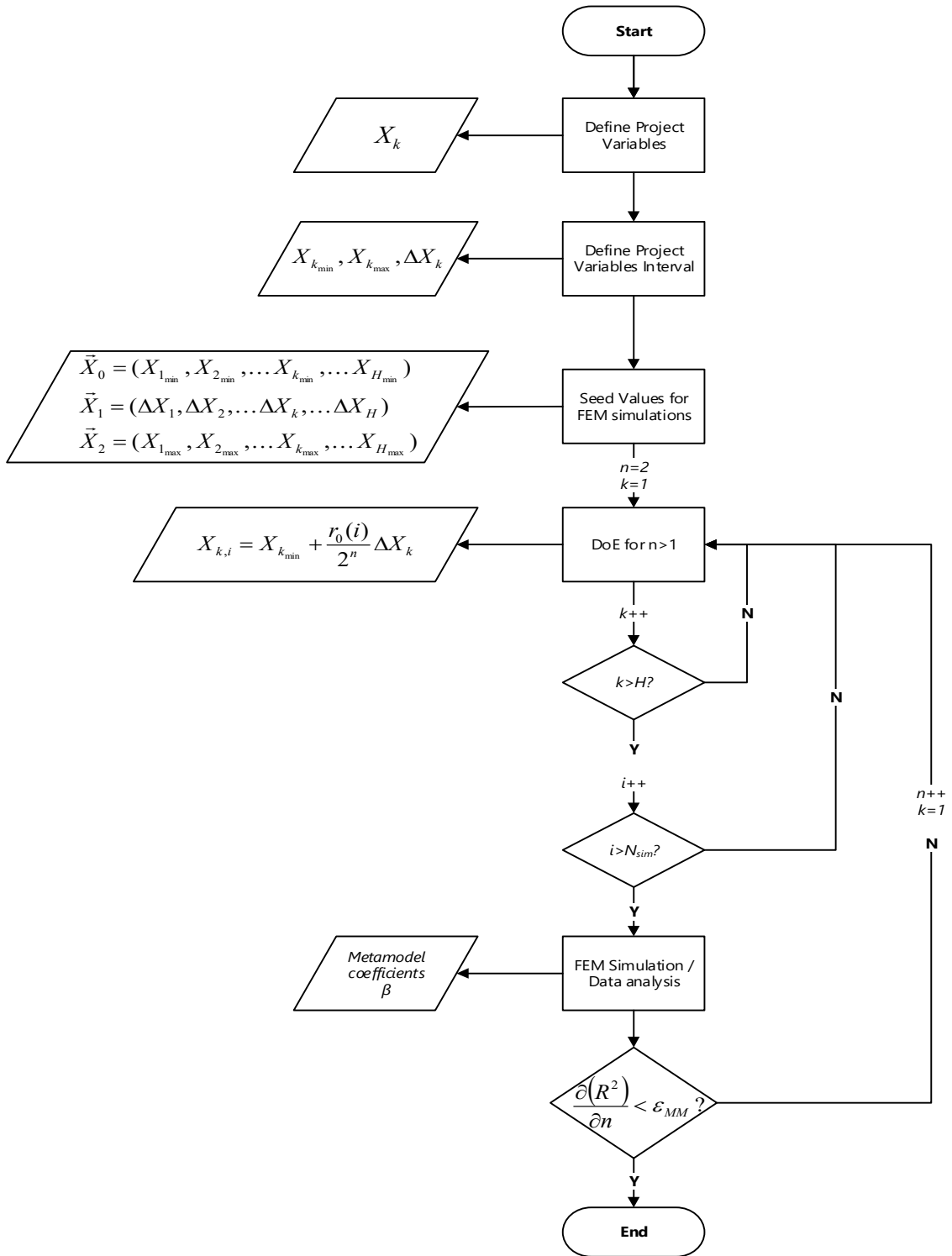
Source: Personal file.

Thus, the randomness of function $r_o(i, n)$ and the restriction of reaching equal input variables values guarantees the space filling of the variables domain. DoE simulations are generated until metamodel parameters reach convergence, measured by the relative variation of R^2 along with the increment of metamodel iteration cycle n (rate of convergence),

$$\frac{\partial(R^2)}{\partial n} \equiv \frac{\Delta R^2}{R^2} = \frac{(R^2)_{n+1} - (R^2)_n}{(R^2)_{n+1}} < \varepsilon_{MM} \quad (46)$$

where ε_{MM} is a the metamodel convergence error and R^2 is the statistical correlation coefficient as defined ahead. The process of generating designed experiments is summarized in the flowchart of Figure 32.

Figure 32 - Flowchart of generating DoE simulations for metamodel construction



Source: Personal file.

3.3.3. Data analysis

FEM models with project variables defined according to the sampling points obtained from DoE are simulated. Then, functions are used in curve fitting of the output cloud of points generated by the FEM simulations to build the metamodel. The most used techniques are Response Surface Method (RSM), Radial Basis Functions (RBF) and Kriging [16]. Among them, the simplest is RSM, which is basically a polynomial regression. Independently of the adopted technique, the general form of the method results in an approximation of the exact solution,

$$y_i = \hat{y}_i + \epsilon_i \quad (47)$$

where, for a given state i of input variables, y_i is the exact solution from the numerical model, \hat{y}_i is the approximate response surface and ϵ_i is the error between the exact solution and the approximation. The approximations \hat{y}_i are those that minimize the sum of squared errors (SSE), defined as,

$$SSE = \sum_{i=1}^{N_{sim}} \epsilon_i^2 = \sum_{i=1}^{N_{sim}} (y_i - \hat{y}_i)^2 \quad (48)$$

In RSM, \hat{y}_i is a linear combination of functions $\varphi_{k,l,i}$, which can stand for the polynomial terms of the polynomial series,

$$\hat{y}_i = \beta_0 + \sum_{k=1}^H \sum_{l=1}^Q \beta_{k,l} \varphi_{k,l,i} \quad (49)$$

To minimize SSE the derivatives of \hat{y}_i with respect to each metamodel coefficients must be null,

$$\frac{\partial SSE}{\partial \beta_{k,l}} = 0 \quad (50)$$

resulting in a linear system of the type $\mathbf{A}\boldsymbol{\beta} = \mathbf{b}$ to be solved for coefficients $\beta_{k,l}$ [80], where \mathbf{A} is the coefficients matrix for the linear system and \mathbf{b} is the constant column vector,

$$\begin{bmatrix} N_{sim} & \sum_{i=1}^{N_{sim}} \varphi_{1,1,i} & \sum_{i=1}^{N_{sim}} \varphi_{1,2,i} & \cdots & \sum_{i=1}^{N_{sim}} \varphi_{H,Q,i} \\ \sum_{i=1}^{N_{sim}} \varphi_{1,1,i} & \sum_{i=1}^{N_{sim}} \varphi_{1,1,i}^2 & \sum_{i=1}^{N_{sim}} \varphi_{1,1,i} \varphi_{1,2,i} & \cdots & \sum_{i=1}^{N_{sim}} \varphi_{1,1,i} \varphi_{H,Q,i} \\ \vdots & \vdots & \vdots & \ddots & \vdots \\ \sum_{i=1}^{N_{sim}} \varphi_{H,Q,i} & \sum_{i=1}^{N_{sim}} \varphi_{H,Q,i} \varphi_{1,1,i} & \sum_{i=1}^{N_{sim}} \varphi_{H,Q,i} \varphi_{1,2,i} & \cdots & \sum_{i=1}^{N_{sim}} \varphi_{H,Q,i}^2 \end{bmatrix} \begin{bmatrix} \beta_{1,1} \\ \beta_{1,2} \\ \vdots \\ \beta_{H,Q} \end{bmatrix} = \begin{bmatrix} \sum_{i=1}^{N_{sim}} y_i \\ \sum_{i=1}^{N_{sim}} \varphi_{1,1,i} y_i \\ \vdots \\ \sum_{i=1}^{N_{sim}} \varphi_{H,Q,i} y_i \end{bmatrix} \quad (51)$$

In general, linear systems are solved through an iterative method of optimization, such as gradient descendant algorithm. Instead solving it by direct method, which calculates inverse matrix leading to numerical errors and expensive memory consuming, the seek vector of coefficients $\boldsymbol{\beta}$ are found through j iterations,

$$\boldsymbol{\beta}_{j+1} = \boldsymbol{\beta}_j - \Omega \nabla \left(\|\mathbf{A}\boldsymbol{\beta}_j - \mathbf{b}\|_2^2 \right) \quad (52)$$

where Ω is the variable rate of learning, $\nabla(\cdot)$ is the gradient of multi-variable function, $\boldsymbol{\beta} = (\beta_{1,1}, \beta_{1,2}, \dots, \beta_{k,l}, \dots, \beta_{H,Q})^T$ and $\|\mathbf{x}\|_p$ is the matrix p -norm defined as,

$$\|\mathbf{x}\|_p = \left(\sum_{j=1} |x_j| \right)^{1/p} \quad (53)$$

For the least squares of a linear system, the method is also called ordinary linear regression (OLR), whose the solution is defined as [81],

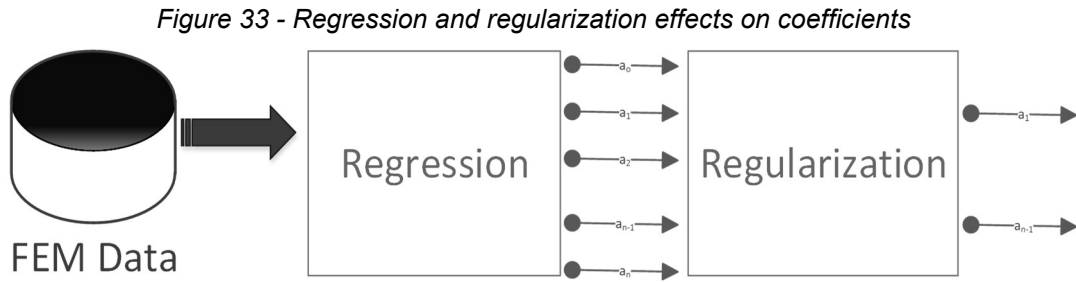
$$\nabla \left(\|\mathbf{A}\boldsymbol{\beta}_j - \mathbf{b}\|_2^2 \right) = 2\mathbf{A}^T(\mathbf{A}\boldsymbol{\beta}_j - \mathbf{b}) \quad (54)$$

An initial value $\boldsymbol{\beta}_0$ is attributed to the coefficients. Iteration runs until a stop condition is met,

$$\|\nabla(\boldsymbol{\beta}_j)\| < \varepsilon_\beta \quad (55)$$

where ε_β is the metamodel coefficients convergence error. The number of coefficients $\beta_{k,l}$ is proportional to number of design variables and the order Q of the polynomial equation used in the linear regression.

Ordinary linear regression may cause unstable variations in the $\beta_{k,l}$ coefficients magnitude. Regularization methods by penalties are used together with linear regression, which acts as filters to the coefficients, to reduce those variations and capture the essential variables that governs the system response (Figure 33). They limit the coefficients norm by a predefined value k_T , which must be determined in tuning process to optimize accuracy and model complexity [82].



Source: Personal file.

The three main regularizations are Lasso (l_1), Ridge (l_2) and ElasticNet. The first (Lasso) regularization creates sparsity selecting the essential variables, but generate errors for highly correlated variable,

$$\sum_{k=1}^H \sum_{l=1}^Q |\beta_{k,l}| \leq k_T \quad (56)$$

where $| \cdot |$ is the module operator.

The Ridge regularization does not create sparsity, but tends to perform well for highly correlated variable and release smother coefficients,

$$\sum_{k=1}^H \sum_{l=1}^Q (\beta_{k,l})^2 \leq k_T^2 \quad (57)$$

The ElasticNet regularization is a combination of l_1 and l_2 penalties, which tends to perform better than those single regularizations at a cost of an extra weighting variable γ (mixing parameter),

$$\gamma \sum_{k=1}^H \sum_{l=1}^Q |\beta_{k,l}| + (1 - \gamma) \sum_{k=1}^H \sum_{l=1}^Q (\beta_{k,l})^2 \leq k_T^2 \quad (58)$$

In numerical implementation, the budget k_T is substituted by a penalty factor α (tuning parameter) and the coefficients are found using Lagrangian multipliers,

$$\min_{(\beta_0, \beta) \in \mathbb{R}} \left\{ \frac{1}{2} \sum_{i=1}^{N_{sim}} (\mathbf{y}_i - \beta_0 - \xi_i^T \beta)^2 + \alpha \left[\frac{1}{2} (1 - \gamma) \|\beta\|_2^2 + \gamma \|\beta\|_1 \right] \right\} \quad (59)$$

where the default value for γ is 0.5.

Such regression models are implemented in Python libraries [83]. Depending on the number of coefficients $\beta_{k,l}$ to be determined and the regression model used, a minimum number of numerical simulations ($N_{sim_{min}}$) must be performed as a function of number of project variables H and polynomial order Q ,

$$N_{sim_{min}} = 1 + HQ \quad (60)$$

If more simulations results are provided, the convergence of the coefficients $\beta_{k,l}$ are verified by the correlation (or determination) coefficient R^2 defined as,

$$R^2 = 1 - \frac{SSE}{SST} \quad (61)$$

where SSE is the sum of square errors as defined in Equation (50) and SST (sum of squares total) is the squared sum of the distance y_i data is away from its mean \bar{y}_i ,

$$SST = \sum_{i=1}^{N_{sim}} (y_i - \bar{y}_i)^2 \quad (62)$$

For better comparison between models and to really evaluate terms relevance, it is better to use the adjusted coefficient of determination R_{adj}^2 which is based on mean squares rather than sums of squares. It is advantageous in reducing bias from small samples and complex models that tends to the

metamodel overfitting resulting in high R^2 [84]. The relation between traditional R^2 and R_{adj}^2 is given by,

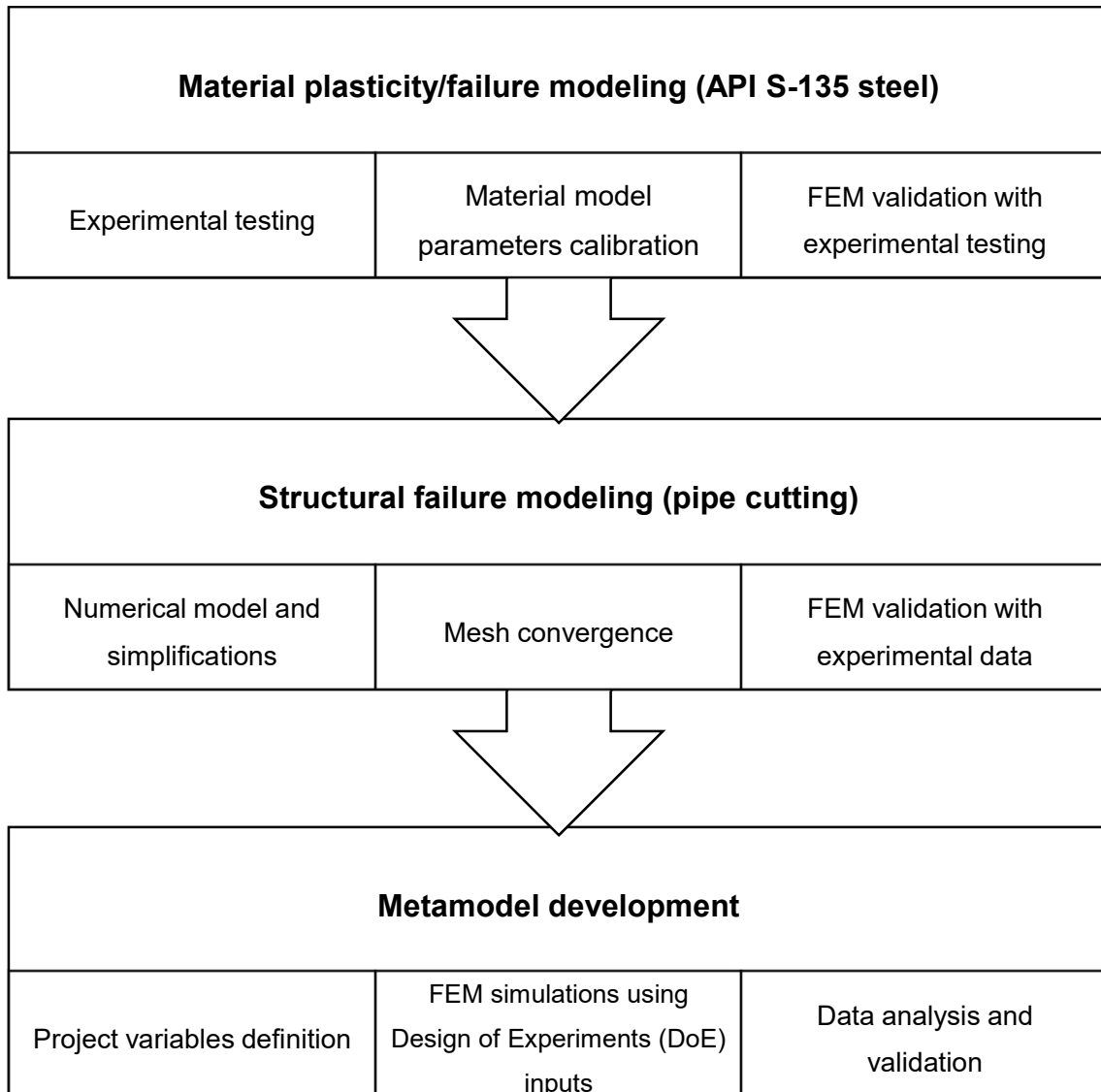
$$R_{adj}^2 = R^2 - \frac{p}{N_{sim}-p-1} (1 - R^2) \quad (63)$$

Where p is the number of nonzero terms in the metamodel. During the iterative process, the input data is divided into two sets, for training and test. The first set is used to determine the metamodel coefficients while the second set (up to 30% of available data) is used to check if the model is robust to predict results. The parameter R^2 is a metric for performance evaluation of the response surface generated by regression and regularization.

4. Materials and Methods

The proposed methodology for the generation of the metamodel for predicting the required force to cut a tube in BOP is shown in the flowchart of Figure 34.

Figure 34 – Proposed methodology



Source: Personal file.

Initially, API S-135 steel is characterized. Information from tensile tests and posterior optical and microscopical analyses of the fractured specimens extracted from a drill pipe are used to describe the elastic, plastic and failure

material behavior. Particularly, the J-C failure model parameters are found. In sequence, pipe cut in BOP is modeled in FEM and validated using data from the literature and from Petrobras commissioning reports.

Finally, the model is used to predict pipe cutting under different drill pipe working conditions, using metamodels technique [85]. Several working condition combinations, based on Latin Hypercube Sampling and values inside a defined range, are simulated via FEM. The required forces to cut the drill string are analyzed using a regression technique and the final results are adimensionalized to compare with different tubulars.

4.1. Material properties

The tubes analyzed in the thesis are made of API S-135 steel, a well-known material used in drill strings manufacturing due to its mechanical strength combined with a resistance to wear and fatigue. This material is considered a low alloy steel having tempered martensitic microstructure (Fe_3C particles in α -ferrite matrix), which is obtained from austenite thermal treatment by annealing, quenching and tempering presenting high tenacity. Despite its high hardness, it is relatively ductile and conformable.

API S-135 steel can be manufactured through a wide range of AISI steels. Steels with high strength, low alloys, fine grains, limited amount of phosphorous and sulfur in its composition as well with mechanical properties that satisfies API Spec 5DP can meet the API S-135 requirements [86]. The general mechanical properties are resumed in Table 6 and the chemical composition of the pipes used is shown in Table 7, including values obtained in different previous studies [87], [88]. As it can be seen, there is a significant variation in the steel composition mainly due to few API standard requirements.

Table 6 - Samples mechanical properties

Source	Yield Strength (MPa)	Elasticity Modulus (GPa)	Poisson ratio	Tensile strength (MPa)	Ultimate strength (MPa)	Elongation (%)
API Spec 5D, 2000	931< σ_y <1138	-	-	>1000	-	>12.5%
Han, 2015	937	202	0,3	976	-	20
Miscow, 2001	1028	-	-	1078	680	21

Source: Personal file.

Table 7 - Chemical composition for S-135 pipes

Source	C	Si	Mn	P	S	Cr	Ni	Cu	Mo
API Spec 5D, 2000	-	-	-	<0.015	<0.030	-	-	-	-
Yan, 2014	0.26	0.21	0.77	0.011	0.0024	0.88	0.021	0.075	0.35
Miscow, 2001	0.33	0.39	1.07	0.022	0.010	0.89	0.03	-	0.21

Source: Personal file.

4.2. Analyzed material samples

Depending on the well construction phase, different sizes of drill strings are used. A total of 10 different tubes are used in this study. Drill pipes are specified basically through their outer diameter (D_e) and its linear weight measured in imperial units (Pounds Per Foot - *ppf*). Once the steel volumetric density for all drill pipes is almost constant, the *ppf* is directly related to the pipe wall thickness (t). Their geometries are detailed in Attachment C and the principal measures are summarized in Table 8. As it can be seen, except for the smallest tube, they can be considered thin thickness tubulars, once the ratio the ratio $\frac{D_e}{t} > 10$.

Table 8 - Geometrical properties of the studied pipes

#	Lin. Weight (ppf)	D_e	t (mm)	D_e/t	S_t (mm ²)
1	13.30	3.50" (88.9mm)	9.35	9.51	2336.1
2	14.00	4.00" (101.6mm)	9.65	10.53	2788.1
3	20/18.7	4.50" (114.3mm)	10.92	10.47	3547.2
4	19.50	5.00" (127.0mm)	9.19	13.81	3403.0
5	21.90	5.50" (139.7mm)	9.17	15.24	3760.1
6	24.70	5.50" (139.7mm)	10.54	13.25	4277.2
7	24.20	5.88" (149.4mm)	9.17	16.27	4034.5
8	25.20	6.63" (168.4mm)	8.38	20.09	4213.8
9	27.60	6.63" (168.4mm)	9.19	18.31	4598.9
10	40.87	6.63" (168.4mm)	15.88	10.60	7600.6

Source: Personal file.

4.3. Mechanical testing

In order to characterize API S-135 failure in different stress states, several specimens were manufactured from a 5.5" 21.9 *ppf* pipe (Figure 35).

Figure 35 – 5.5" 21.9ppf drill pipe used for manufacturing testing specimens

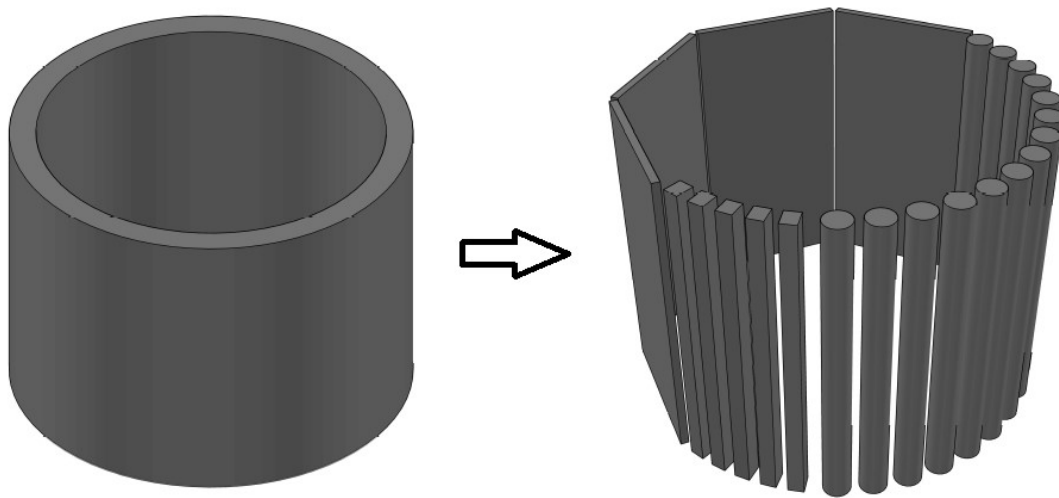


Source: Personal file.

The extraction of the specimens for mechanical tests followed the procedure described by Paredes (2018) [89], which is illustrated in Figure 36.

Beams are generated from longitudinal cuts in a part of the tube. Some of the beams are machined in lathe to form the dog-bone specimens. Plain specimens were extracted by electrical discharge machining (EDM).

Figure 36 - Specimens extraction process



Source: Personal file.

The specimens were tested in a screw-driven machine, INSTRON3369 (Figure 37) at room temperature. For the case of the DB specimens (unnotched and notched), they were held by conventional jaws. For the beam specimens, rods passing through the machine support ends were used to lateral rotations of the beam specimens, absorbing any possible small misalignments. The specimens were pulled by the machine at a speed of 0.02 mm/min, which is slow enough to avoid any strain rate effect. Load and displacement along the test instants were recorded. Displacements were measured by electrical clip gauges rigidly attached around the notches and the crack onset regions, right in the middle of the gauge. Moreover, the Digital Image Correlation, DIC technique, was adopted. For that, the specimen is speckled with black and white spots that slightly change relative position during deformation. The changes are analyzed in a sequence of pictures of the experimental test, taken in a rate of 0.20 pictures/second, by the software INSTRON 4D.

Figure 37 – INSTRON 3369 universal testing machine and experimental arrangement at GMSIE/USP



Source: Personal file.

The software calculates the strain field and present it in a colored scale, superposed to the original image, as illustrated in Figure 38.

Figure 38 - DIC analysis of tensile testing at LFS/USP



Source: Personal file.

After testing, the surface of some of the fractured specimens were observed at 20x magnifying optical microscope and at 5000x JEOL JSM-6010LA scanning electronic microscope (SEM) using secondary electron which is shown in Figure 39. The same apparatus is used to measure chemical composition by means of Energy-Dispersive X-Ray Spectroscopy (EDS).

Figure 39 - JEOL JSM-6010LA scanning electronic microscope



Source: Personal file.

Measurement of hardness with Rockwell C indenter was also performed in the cross section of the tested specimens. During the preparation, the specimens were cut, polished using a fine sandpaper, cleaned in ultrasonic bath and dried with air blast. Then, they were jointed in a polyurethane matrix (Figure 40) and hardness was measured near the surface. The measured hardness gradient is used to validate the plastic strain field predicted by FEM simulation.

Figure 40 – Samples for measurement of hardness property

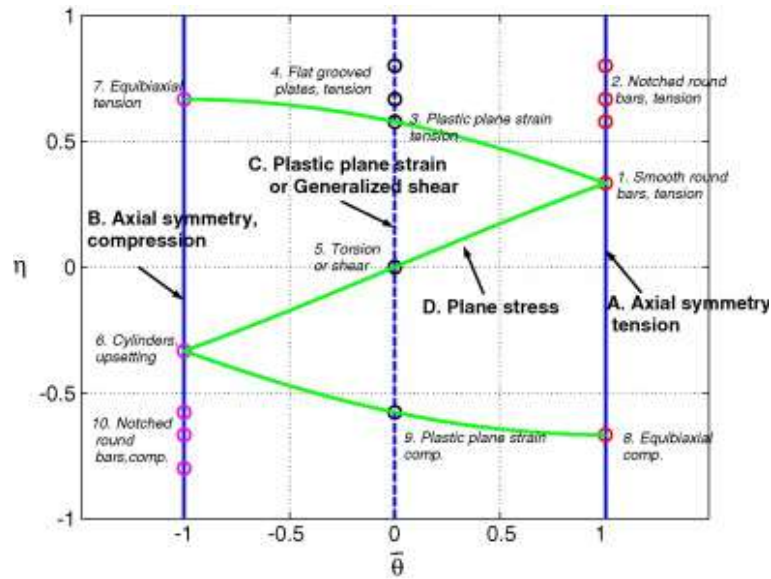


Source: Personal file.

4.3.1. Testing specimens geometry

Classical testing specimens (TPs) are used in the literature to calibrate the material model in a wide range of stress state. A summary of classical TPs with their theoretical triaxiality (vertical axis) and Lode angle (horizontal axis) at the fracture locus are illustrated in Figure 41 and summarized in Table 9. Based on such TPs, some testing specimens were projected to be manufactured (Attachment B). Ideally, the specimen geometries should maintain the triaxiality and the Lode angle constant on the fracture locus during the test. However, this is not possible in practice [37].

Figure 41 - Expected stress states of classical TPs



Source: Extracted from [37].

Table 9 - Classical shapes for testing specimens

No	Specimen type	Loading	Triaxiality	Lode angle (°)
1	Smooth round bars	Tension	$\frac{1}{3}$	0
2	Notched round bars (Bridgman, 1952)	Tension	$\frac{1}{3} + \ln\left(1 + \frac{a}{2R}\right)$	0
3	Plastic plane strain	Tension	$\frac{\sqrt{3}}{3}$	30
4	Flat grooved plates	Tension	$\frac{\sqrt{3}}{3} \left[1 + 2 \ln\left(1 + \frac{t}{4R}\right) \right]$	30
5	Torsion or shear	Tension	0	30
6	Cylinders	Compression	$-\frac{1}{3}$	60
7	Equi-biaxial plane stress	Tension	$\frac{2}{3}$	60
8	Equi-biaxial plane stress	Compression	$-\frac{2}{3}$	0
9	Plastic plane strain	Compression	$-\frac{\sqrt{3}}{3}$	30
10	Notched round bars	Compression	$-\left[\frac{1}{3} + \ln\left(1 + \frac{a}{2R}\right) \right]$	60

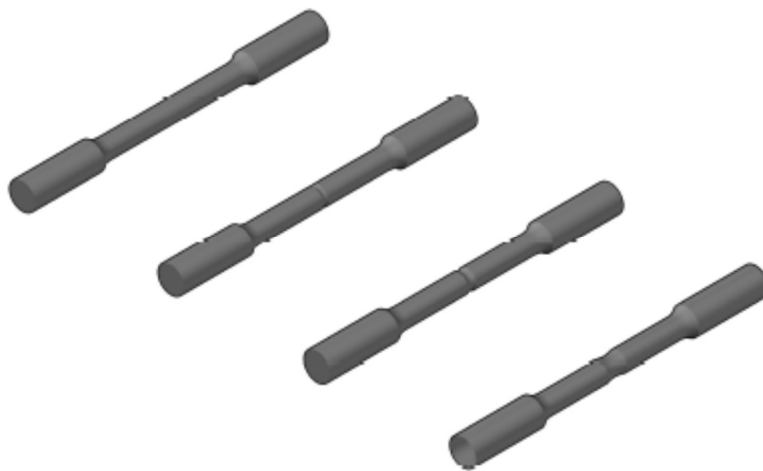
Source: Extracted from [37].

In addition, experiments with carefully designed cruciform specimens are discussed by Gerke et al (2017, 2020) [46] [90] and Brünig et al (2019) [91] to cover a wider range of biaxial stress states. However, the specimens were

extracted from a 5.5in 21.9ppf tube and, due to restrictions on specimens size (Figure 36), biaxial experiments were not possible. Different possible geometries for the specimens are presented in Figure 42 and Figure 43, to test the material failure at different triaxialities and Lode angles [60].

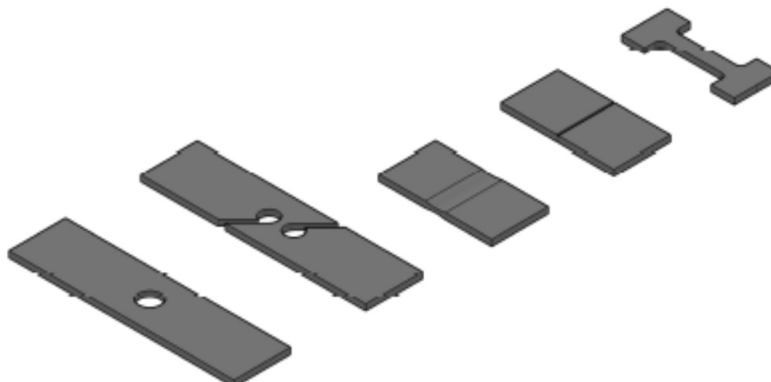
However, the material parameters were obtained from experimental tensile tests with unnotched and differently notched dog-bone (DB) specimens, manufactured and tested before COVID-19 outbreak.

Figure 42 – Geometry of smooth (dog-bone) and notched round bars specimens



Source: Personal file.

Figure 43 - Geometry of flat specimens

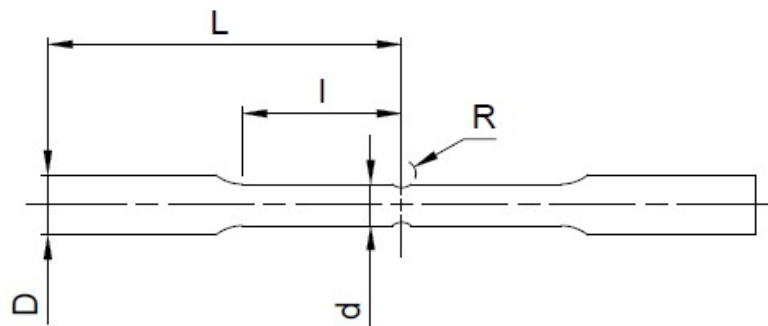


Source: Personal file.

The geometries of the manufactured testing specimens are illustrated in Figure 44 (DBs) and Figure 45 (Beams). The DB shape is cylindrical, with diameter $D = 8.75\text{mm}$ and length $L = 50\text{ mm}$. Three unnotched DB specimens and one DB specimen with each different notch of 1mm, 2mm and 10mm were manufactured.

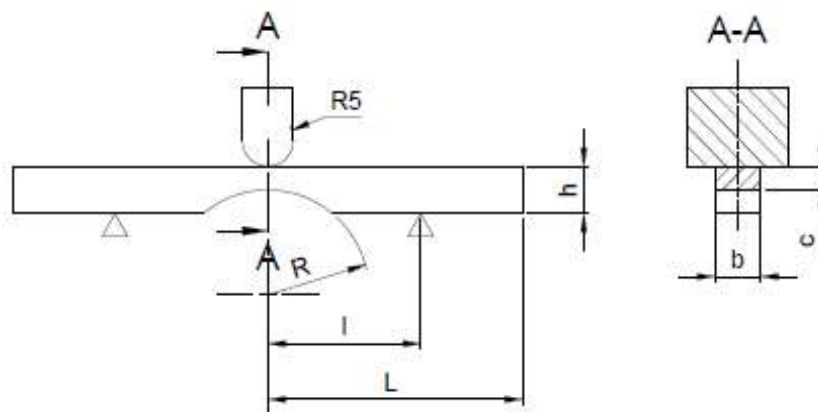
The prismatic beams have length of $L = 50\text{mm}$ and the supports were $l = 30\text{ mm}$ distant from the center of symmetry. For 3-point-bending beam specimen, notches of 2 and 10mm were manufactured as shown in Figure 45 and only one specimen of each geometry was manufactured.

Figure 44 - Tensile Dog-bone specimen



Source: Personal file.

Figure 45 - 3-point-bending specimen



Source: Personal file

The measures taken of the manufactured specimens and its nomenclature are summarized in Table 10 (cylindrical dog-bone shape) and Table 11 (beams for 3-point bending).

Table 10 - Dimensions measured for cylindrical DB specimens

Specimen	l (mm)	d (mm)	R (mm)	D_{min} (mm)*
NN	23.8	5.69	0.00	5.50
NT01	24.1	5.83	0.50	5.20
NT02	21.5	5.59	1.00	4.60
NT10	22.8	6.11	5.00	5.30

* D_{min} : DB diameter at the notch

Source: Personal file.

Table 11 - Dimensions measured for 3-point bending testing beams

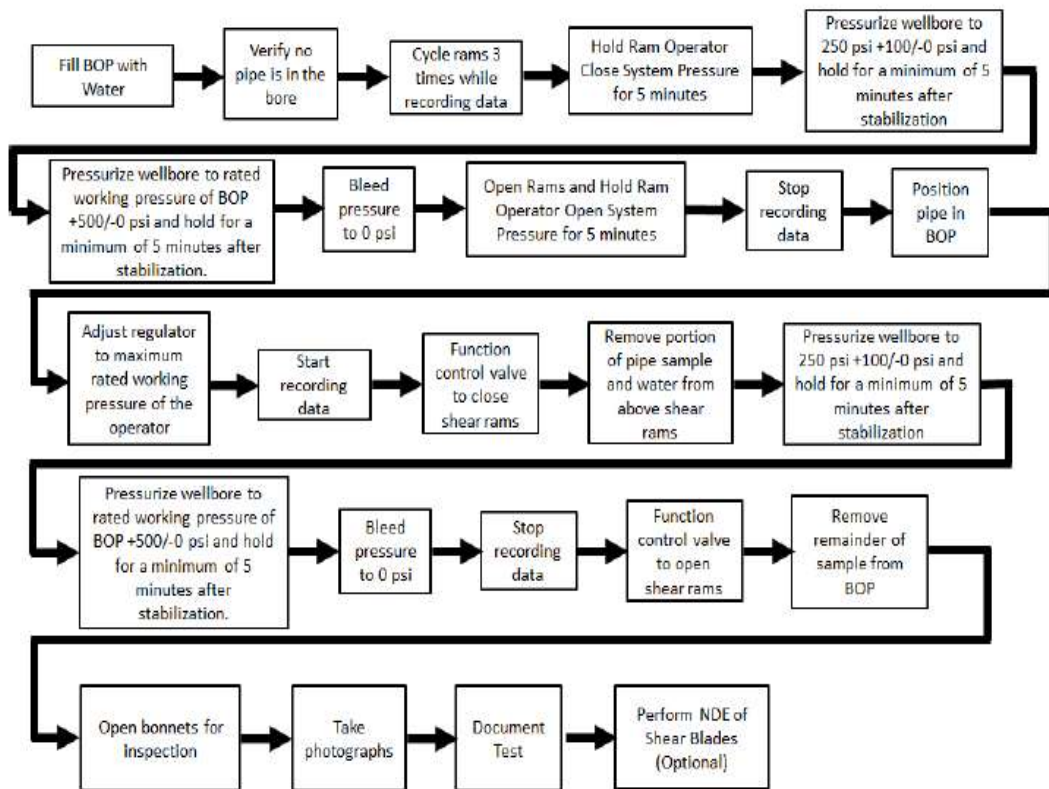
Specimen	h (mm)	b (mm)	c (mm)	R (mm)
NNB	8.9	9.0	9.0	0.0
NT05B	9.0	9.0	5.0	5.0
NT12B	8.7	9.2	5.1	12.0

Source: Personal file.

4.3.2. BOP commissioning tests

Before delivered to use, the BOP is tested for checking the shearing rams capability. Even though sometimes the BOP manufacturer provides the shearing capability, normally this test is done in the commissioning stages. The standard recommended protocol for the shear testing is reported by API 16TC [92] and is shown in Figure 46. An experimental commissioning testing is shown in Figure 47 and an example of a cut pipe is illustrated in Figure 48.

Figure 46 - BOP shear testing protocol



Source: Extracted from API 16TR (2018) [92].

Figure 47 - Pipe being positioned inside BOP for shear testing



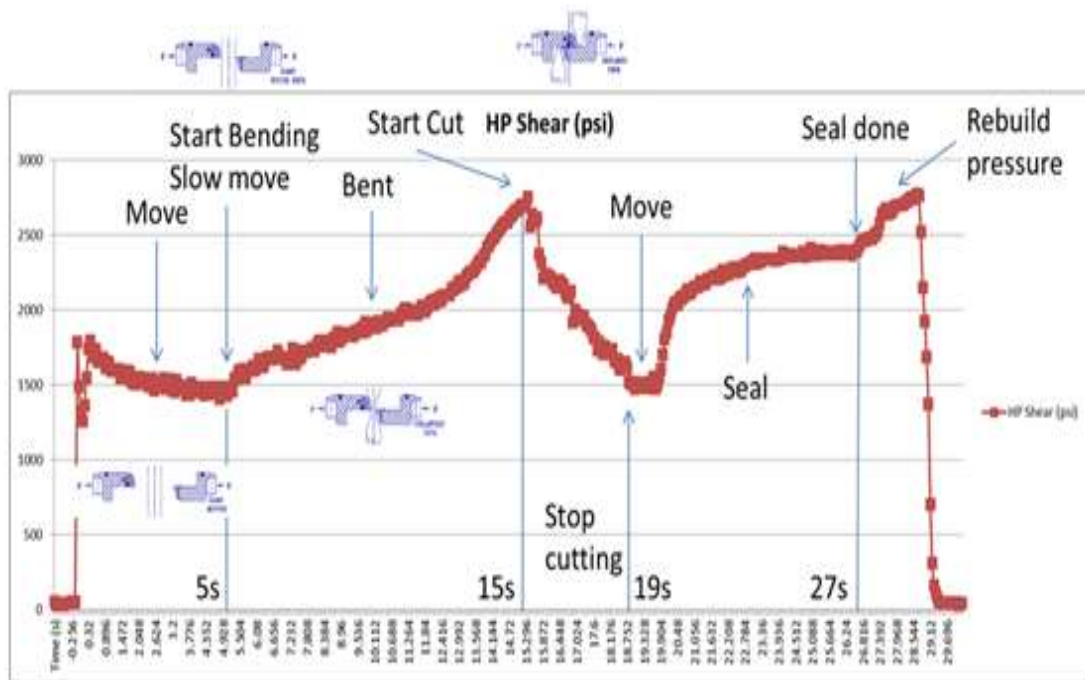
Source: Petrobras.

Figure 48 - Drill pipe cut in BOP

Source: Petrobras.

The study case of this thesis uses mainly the data available in literature for BOPs commissioning reports. Such sources provide information of cutting forces in BOP and the final geometry of different pipes. The force on the ram is obtained by the total equivalent area of the piston multiplied by the measured pressure on ram close chamber. An example of the resulting pressure spectra recorded while cutting a pipe is shown in Figure 49. The cutting force is obtained by the ultimate pressure along the indenter course to close the BOP bore. However, such measure includes the frictional (internal) forces that must be overcome by the BOP to displace the rams.

Figure 49 - Pressure spectra (in psi) obtained in Shear ram piston during shearing process as a function of time



Source: Extracted from [26].

4.3.3. Geometry for the BOP rams

There are several types of rams available in the market. However, in this study, only the shearing tests performed with the Double “V” shear ram profile in 18 3/4” BOP bore will be considered, which include tests performed by Hydril BSR (Figure 50) and Shaffer (NOV) CVX rams (Figure 51).

Figure 50 - Hydril BSR rams



Source: Petrobras.

Figure 51 - Shaffer CVX ram

Source: Extracted from [93].

4.4. Numerical models

In the following section, it will be presented the numerical models used in the analysis.

4.4.1. Testing pieces model

The specimens were simulated using ABAQUS FEM software and the numerical results were compared to experimental measurements. Numerical simulations were modeled adopting the following element types, properly selected for its use: axisymmetric shell triangles (CAX3) and hexagonal element with reduced integration (C3D8R) for DB specimens (the first element allowed a better mesh discretization); hexagonal element with reduced integration (C3D8R) for 3-point-bending beam specimens, as resumed in Table 12 and illustrated in Figure 52. Symmetry was exploited in all specimens to reduce calculations: only the transversal section of DB (CAX3), 1/8 of DB (C3D8R) and 1/4 of beam were

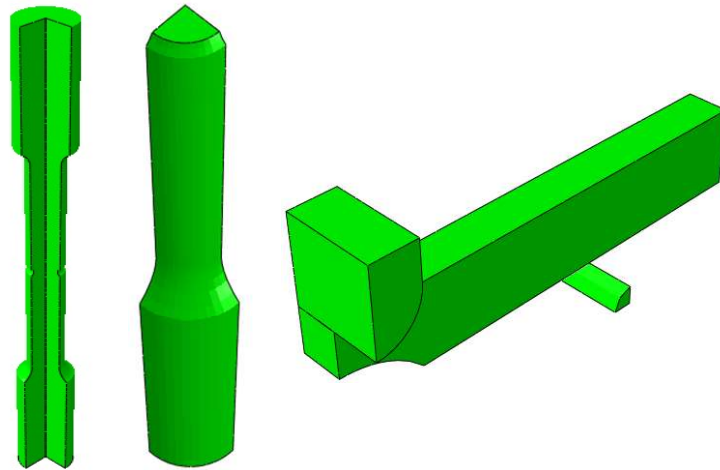
simulated. Results of the tests are described next, compared with the numerical curves produced by the finite element analysis.

Table 12 - Mesh shaping used for numerical models

Numerical model	Element type	Element size (mm)	Use
DB	CAX3	0.5	Stress-strain curves
	C3D8R	0.6	Triaxiality
3-point-bending	C3D8R	0.6	Load-displacement and strain fields

Source: Personal file.

Figure 52 - Geometry of the testing specimens modeled by FEM



Source: Personal file.

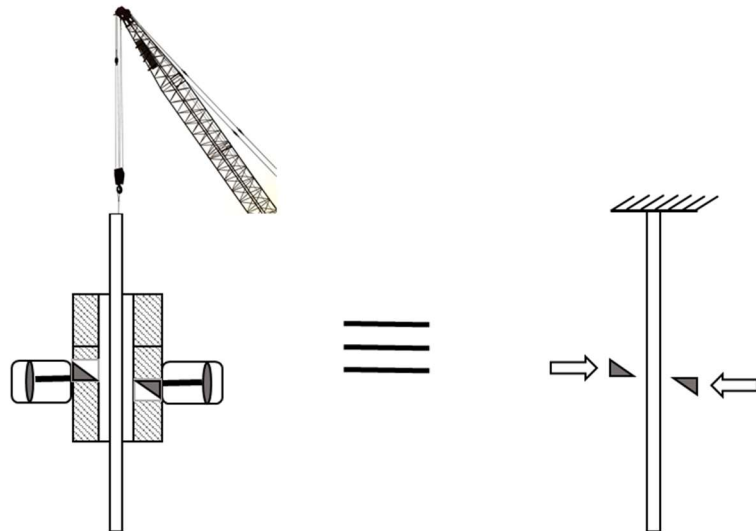
4.4.2. Pipe cut in BOP model

The pipe cut in BOP model mesh, constraints and boundary conditions are based on field observations and literature previous works and, along with the material model determine the numerical problem. The numerical models were based on two cases: BOP commissioning and emergency disconnection with pipe stuck in well. In both cases, the geometry of the indenters was based on the “V” type rams used in field and they displace at constant velocity of 20mm/s. The whole structure is subjected to gravity force.

In the first case, the cutting process of all pipes summarized in Table 8 were simulated in ideal conditions. In commissioning condition, the pipe is hanged through BOP by a crane and is cut to verify the equipment functionality. Thus, the case can be modeled as the pipe clamped in the upper edge once the

pulley block is very heavy (usually about 10 metric tons) and free to move on the lower edge, as illustrated in Figure 53 and summarized in Table 13. The geometry of the numerical model is illustrated in Figure 54.

Figure 53 - Model constrains of BOP commissioning case model



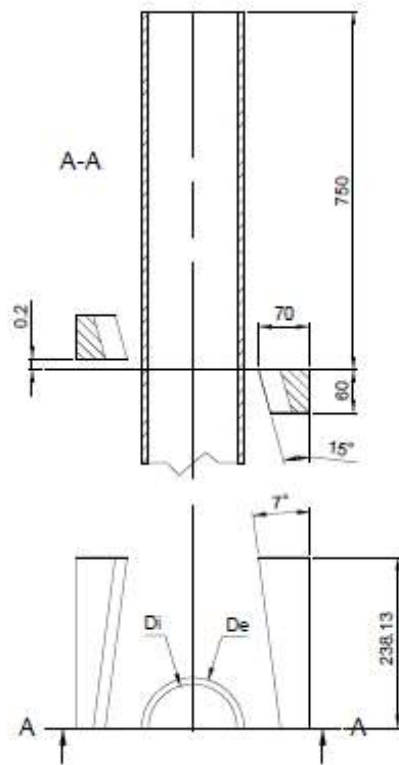
Source: Personal file.

Table 13 – Summary of BOP commissioning case model constrains

#	Part	Location	Constrain
1	Tube	Lower edge	Free
2	Tube	Upper edge	Clamped

Source: Personal file.

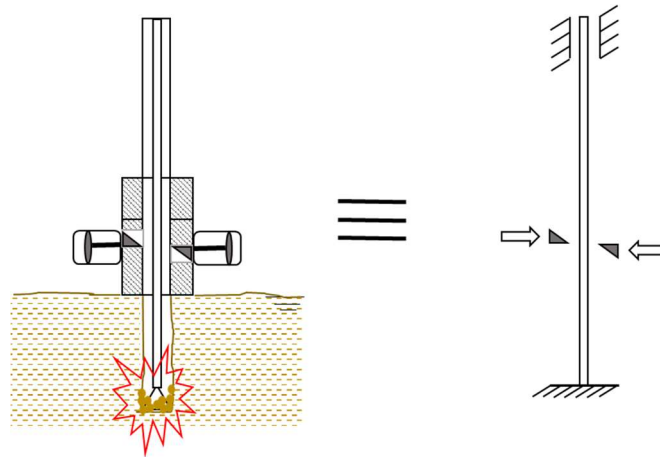
Figure 54 - Geometry for pipe cut in BOP commissioning case



Source: Personal file.

On the other side, pipe stuck in the well is considered the most critical situation in an emergency for BOP disconnection due to its rigidity and smaller number of degrees of freedom, when compared to the BOP commissioning case. In such model the geometry of the pipe was fixed for 6 5/8" 40.87ppf and additional constraints and boundary conditions were established to simulate adverse and realistic situations. It was considered that the pipe couldn't be centralized in BOP to perform a well control prior cutting and disconnecting BOP from wellhead. In the corresponding model, the tube is constrained by its lower extremity due to, for example, well collapse. The model constraints are illustrated in Figure 55 and summarized in Table 14. The geometry of the numerical model is detailed in Figure 56.

Figure 55 - Model constrains of pipe stuck in well case model



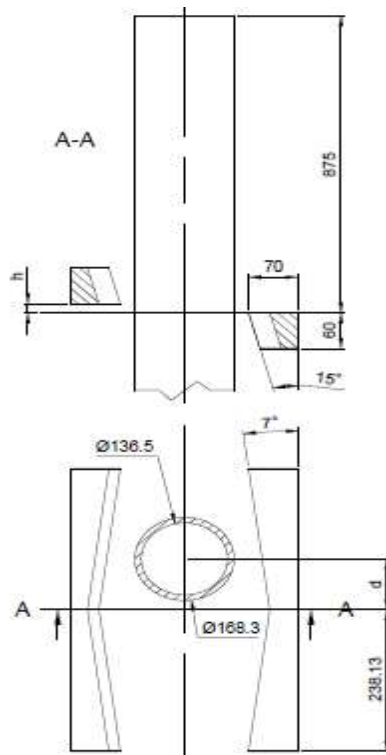
Source: Personal file.

Table 14 – Summary of pipe stuck in well case model constrains

#	Part	Location	Constrain
1	Tube	Lower edge	Clamped
2	Tube	Upper edge	Allow to move in its longitudinal direction

Source: Personal file.

Figure 56 - Geometry of the pipe cut in BOP model (dimensions in mm)



Source: Personal file.

4.4.2.1. Input project variables

The pipe ultimate cutting force (F) is affected by normal traction loads (N), torques (T), internal (P_i) and external (P_e) pressures on tube, as well as its decentralization from BOP bore center (d) and the offset of the indenters (h), which are taken as project variables. Bending on the tube due to the rig drift was not considered once BOP normally is actuated before a considerable curvature is observed [94].

Traction loads are limited by the maximum weight the rig derrick can support in tension and by bucking phenomenon of the tubular in compression. Torque usually is limited by make-up connections in the drill string. Pressure should never exceed the well control equipment capability. Geometric factors such as indenter offset and pipe decentralization from well center are restricted by BOP dimensions. The limits for such project variables are listed in Table 15.

Table 15 – Project variables limits

Variables limits

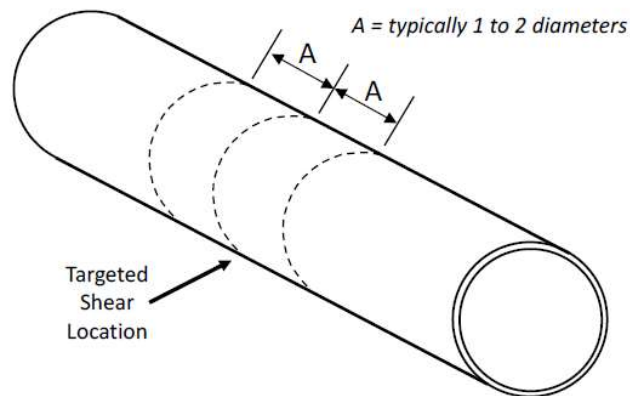
	N	T	P_i	P_e	h	d
Max	800 kips (3.5 MN)	40 klbf.ft (54.2kNm)	9.5kpsi (65MPa)	9.5kpsi (65MPa)	2.0 mm	84.0 mm
Min	-10 kips (-0.05 MN)	0 klbf.ft (0 kNm)	0 psi (0kPa)	0 psi (0kPa)	0.1 mm	0.0 mm

Source: Personal file.

4.4.2.2. Numerical mesh of pipe

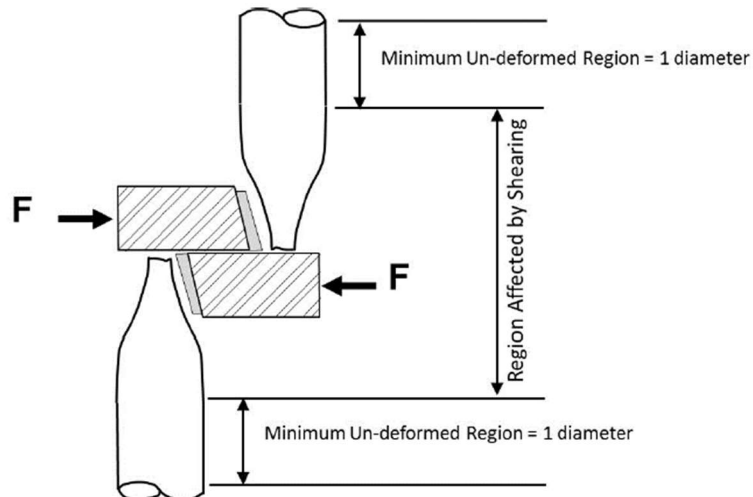
The considered length of the pipe for numerical analysis is in accordance with API technical report 16TR1 (2018) [92], which states that affected (deformed) region by cutting is about 1 to 2 diameters length as shown in Figure 57 and Figure 58. Moreover, the pipe mesh is more refined in the contact region, where large deformations and failure are expected.

Figure 57 - Affected area by shearing



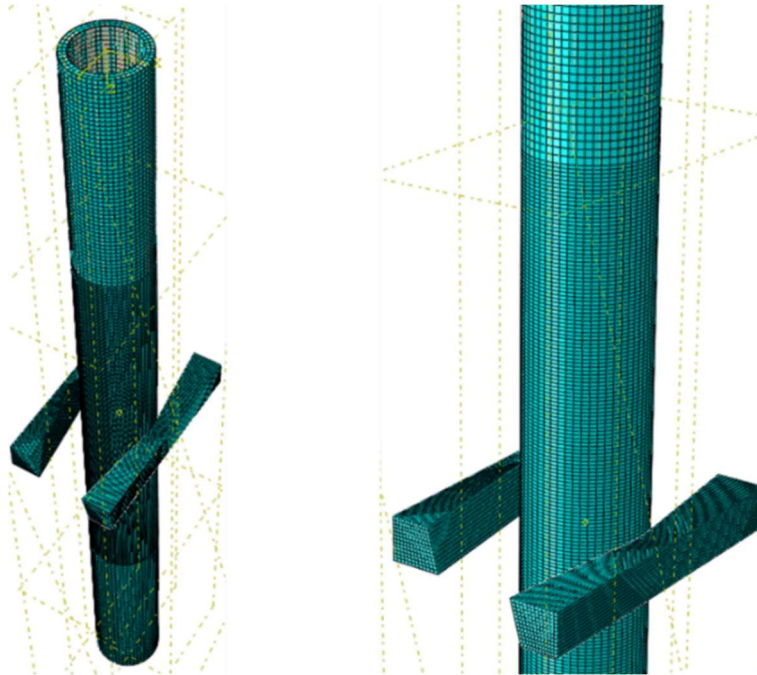
Source: Extracted from API 16TR [92].

Figure 58 - Test sample length requirement



Source: Extracted from API 16TR [92].

In this model, the partitioned area is 1.0m and the length of the tube is 1.75m. Outside this area, the mesh is coarse and integration is reduced. In a first step, hexahedral elements are used for the tube and tetrahedral for the indenter. The meshed geometry is shown in Figure 59.

Figure 59 – Partition on model mesh

Source: Personal file.

5. Results and discussion

This section presents material model parameters calibration based on experimental testing for API S-135 steel specimen. Numerical simulations are performed and compared to experimental results for validation. The calibrated material model is then used to simulate 6 5/8" 40.87ppf drill pipe cutting in BOP and results are compared to literature and commissioning records. Finally, a simplification in the pipe cut in BOP FEM model is proposed and simulations varying the project variables are performed in order to build the metamodel.

5.1. Experimental testing

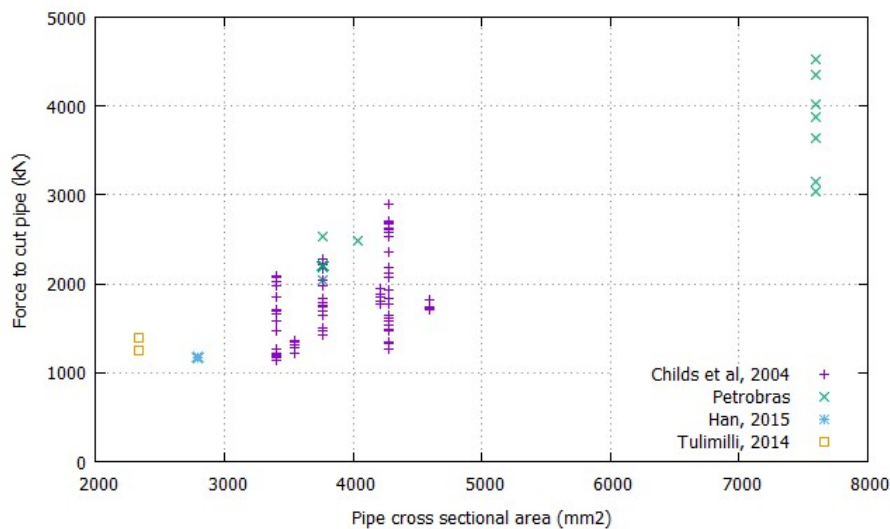
Experimental testing of API S-135 steel specimens were performed at GMSIE (Group of Solid Mechanics and Structural Impact from University of São Paulo) and pipe cut data was collected from literature and from Petrobras during

the period of 2005 to 2018. The data was filtered in order to provide the results only for “V” shape shear rams.

5.1.1. Statistical analysis for BOP commissioning data

BOP commissioning data obtained from the literature and from Petrobras are shown in Attachment D. Data of ultimate force to cut the pipe from Petrobras was collected in diary reports from inspectors who witness the cutting tests in BOP during commissioning procedures. Some reports also provided the dimensions of the cut pipe as illustrated in Attachment E. Data for cut force as a function of cross-sectional area of the tube were compiled and are represented in Figure 60.

Figure 60 - Shear forces x Cross sectional pipe area obtained from literature and Petrobras



Source: Personal file.

From previous data, the ultimate cutting forces and geometry of the cut pipes were analyzed by a statistical approach. The results are shown in Table 16.

Table 16 - Summary of experimental pipe cutting tests

#	PPF	OD (in)	S_t (mm ²)	n samples	Force to cut pipe (kN)	Std. Dev.	OD1 (mm)	OD1 (%)	OD2 (mm)	OD2 (%)
1	13,30	3,50	2336,1	2	1320,2	105,7	115	1,29	52	0,58
2	14,00	4,00	2788,1	1	1179,0	0,0	125	1,23	68	0,67
3	20/18,7	4,50	3547,2	11	1307,2	49,5	*	*	*	*
4	19,50	5,00	3403,0	23	1466,3	341,5	160	1,26	80	0,63
5	21,90	5,50	3760,1	17	1862,3	915,3	210	1,50	60	0,43
6	24,70	5,50	4277,2	28	2026,5	535,5	*	*	*	*
7	24,20	5,88	4034,5	1	2482,0	0,0	215	1,44	40	0,27
8	25,20	6,63	4213,8	5	1851,7	68,9	*	*	*	*
9	27,60	6,63	4598,9	6	1745,6	38,5	*	*	*	*
10	40,87	6,63	7600,6	8	3980,6	729,3	221	1,31	78	0,47

* Data not available

Source: Personal file.

5.1.2. Tensile and bending tests

The notched and unnotched DB tested specimens are shown in Figure 61 up to Figure 64. In order to provide results reliability, three specimens of each type were manufactured and tested. Finally, a 3-point-bending test was performed on three different notched and unnotched beam specimens as illustrated in Figure 65. The chemical composition measured by EDS is shown in Table 17.

Table 17 – Measured chemical composition by EDS for the tested samples

Source	Si	Mn	P	S	Cr	Mo
API Spec 5D, 2000	-	-	<0.015	<0.030	-	-
Tested samples	0.2	0.8	0.01	0.01	0.9	0.3

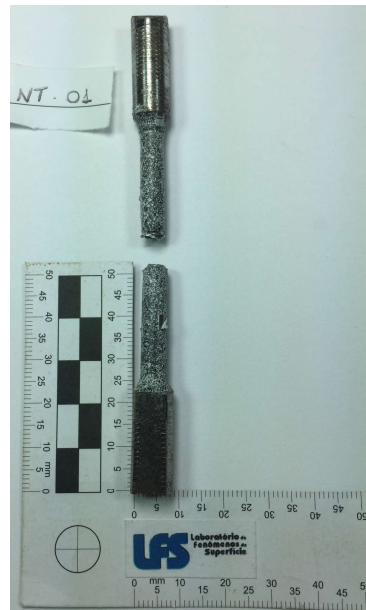
Source: Personal file.

Figure 61 – Unnotched DB NN specimen



Source: Personal file.

Figure 62 - Notched DB NT01 specimen



Source: Personal file.

Figure 63 - Notched DB NT02 specimen



Source: Personal file

Figure 64 - Notched DB NT10 specimen



Source: Personal file

Figure 65 - Beam specimens after 3-point-bending test



Source: Personal file

5.2. Material modeling and analysis

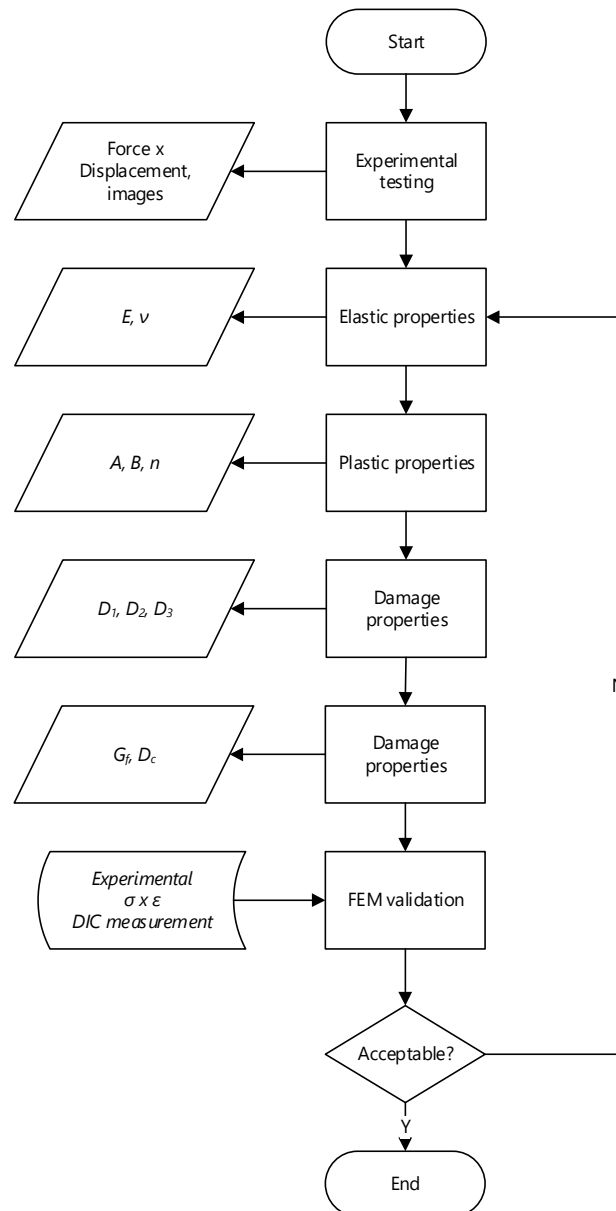
This section presents the numerical results of the material modeling and calibration. The numerical simulations were performed in ABAQUS 6.14-5 FEM software using an Intel Core i7-7500U CPU @ 2.90GHz with 12GB ram memory and a GPU NVIDIA GeForce MX110 2GB.

5.2.1. Material model calibration

Material characterization follows three stages, all validated by comparison with experimental results: (1) elastic and plastic parameters are measured, (2) triaxiality influence on damage initiation modeling, (3) damage evolution and failure criterion. The tensile test performed with the NN specimen provided the elastic and plastic parameters of API S-135 steel. In a first step, the elastic and plastic parameters are measured from the experimental curve and the stress strain curve is plotted analytically to confirm the parameters adherence (J-C model fit). However, such formulation does not consider necking and the parameters obtained are implemented in FEM and simulated to provide the effect

of necking (FEM no damage). At the final step, damage initiation and evolution models were considered in the analyses and the element is deleted when it reaches the failure condition. The material model calibration procedure flowchart is illustrated in Figure 66.

Figure 66 – Process flowchart for material model calibration

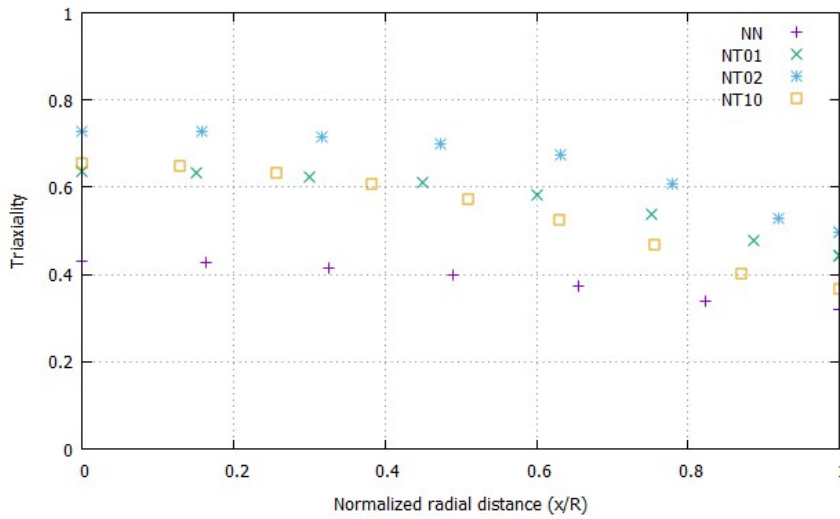


Source: Personal file.

Moreover, the notched specimens provided data to calibrate the failure initiation model at different triaxialities. Damage initiation occurs when

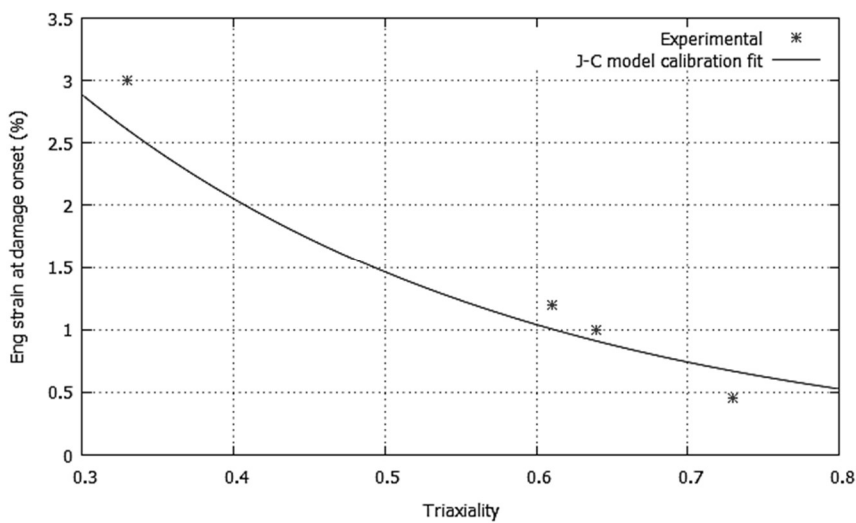
experimental stress-strains curves detach from elastic-plastic FEM simulations. Different triaxiality distributions in the fractured area of tested DB specimens can be perceived numerically, as illustrated by Figure 67, relating triaxiality with the distance of the specimen core to the surface, namely radial distance. At the onset of damage *loci*, triaxiality and plastic strains were determined by FEM to calibrate J-C damage initiation model (Figure 68).

Figure 67 - Triaxiality x normalized distance from DB center



Source: Personal file

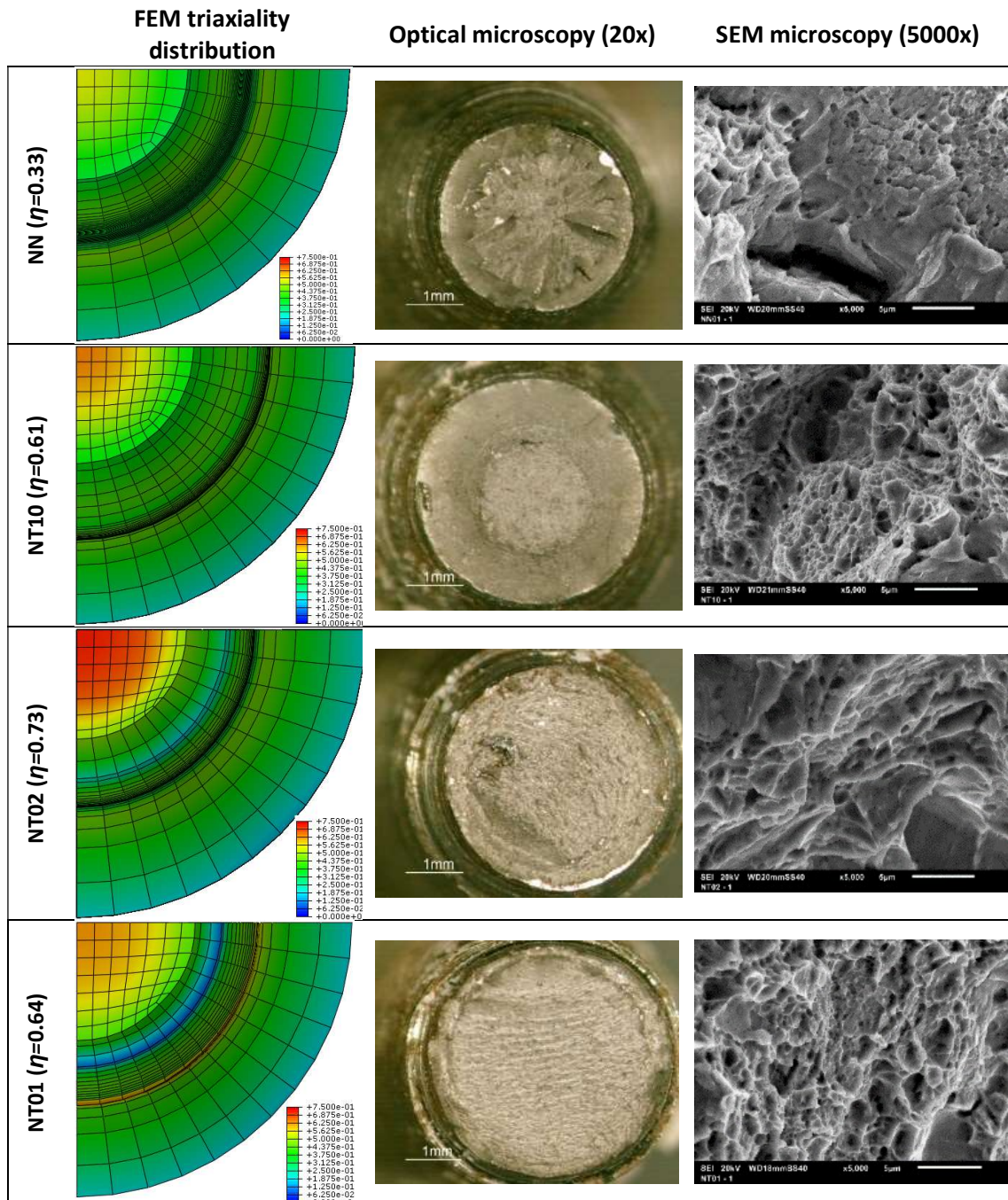
Figure 68 - Calibration procedure for damage initiation model



Source: Personal file.

The effect of triaxiality on API S-135 steel ductility could also be perceived in optical and electronic microscopy (MEV) at the center of the fractured area where voids nucleation begins. Figure 69 shows that, in millimetric scale, the decrease on the surface roughness is visible and with micrometric scale it is seen the tendency to void size increase with an increase of triaxiality.

Figure 69 - DB sample failure

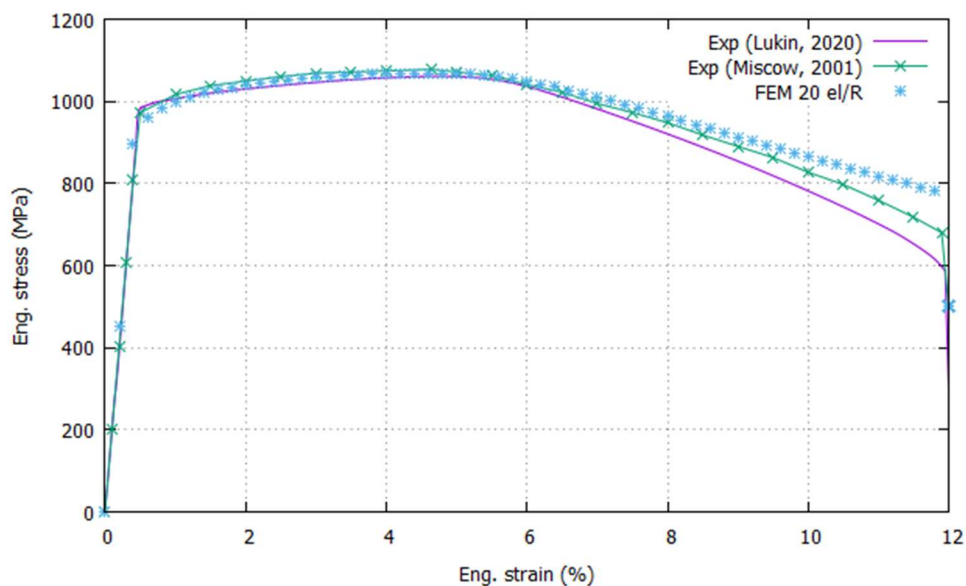


Source: Personal file.

As it can be observed in Figure 69, comparing predicted triaxiality with optical and scanning electron microscopy (SEM) of the fracture surfaces, fragile fractured was spotted in specimens NT02 and NT01, where triaxiality is higher than 0.5. In SEM it was also observed the increase of voids sizes with increase of triaxiality, which increases as notch radii is reduced. The exception was NT02 which presented the highest triaxiality, probably due to manufacturing notch geometry issues. Nevertheless, void diameter in NN specimen which has the lowest triaxiality is less than $1\mu\text{m}$, while in NT02 is higher than $5\mu\text{m}$. NT01 and NT10, having similar triaxiality in the core and similar void profile in the fractured area.

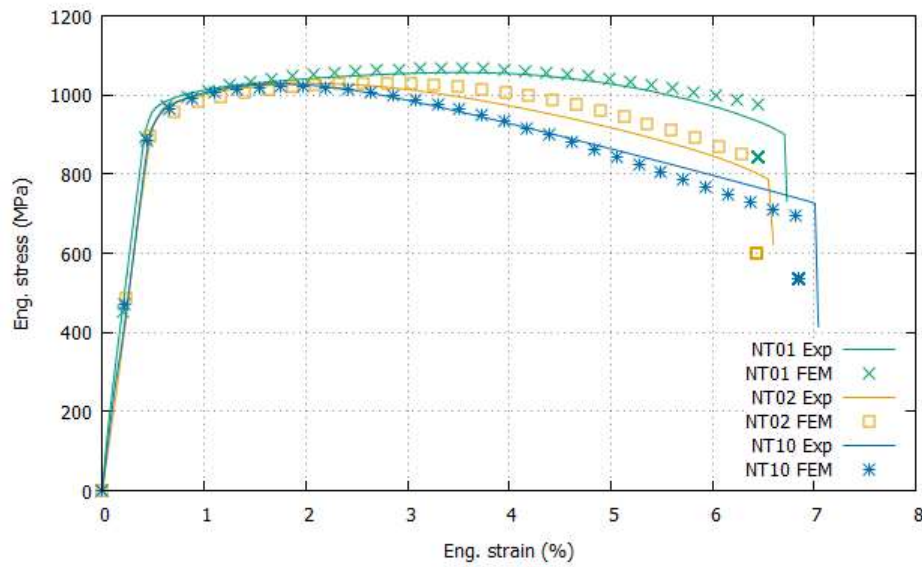
The final step of material model definition is to calibrate the damage and failure parameters. It has been considered a linear evolution of damage model and, by iterative fitting force-displacement curves of FEM simulations on experimental results, material failure criterion was defined as $D_{cr} = 0.048$. Numerical simulation of NN BD specimen in comparison with experimental tests and Literature data [88] are shown in Figure 70 and the notched specimens are illustrated in Figure 71.

Figure 70 - Stress and strains for unnotched specimen and FEM material calibration procedure



Source: Personal file.

Figure 71 - Comparison of experimental and FEM simulation of DB notched specimens



Source: Personal file.

API S-135 steel properties obtained from experimental tests and together with numerical simulations are summarized in Table 18.

Table 18 - API S-135 steel properties

Parameter/ property	Symbol	Value	Unit
Density	ρ	7.6	g/cm^3
Elastic Modulus	E	165	GPa
Poisson's ratio	ν	0.25	-
Yield Stress	$\sigma_y = C_1$	890	MPa
Microhardness	H	35.0	HRC
Ultimate Stress	σ_u	1050	MPa
Nominal strain at NN failure (elongation)	ϵ_{cr}	0.12	-
Friction coefficient	f	0.3	-
Damage at failure	D_{cr}	0.05	-
Energy dissipation parameter	$\frac{G_f}{L}$	12.5	J/mm^3
J-C Plasticity model parameters	C_2	775	MPa
	C_3	0.43	-
J-C Failure model parameters	D_1	0	-
	D_2	0.08	-
	D_3	-3.4	-

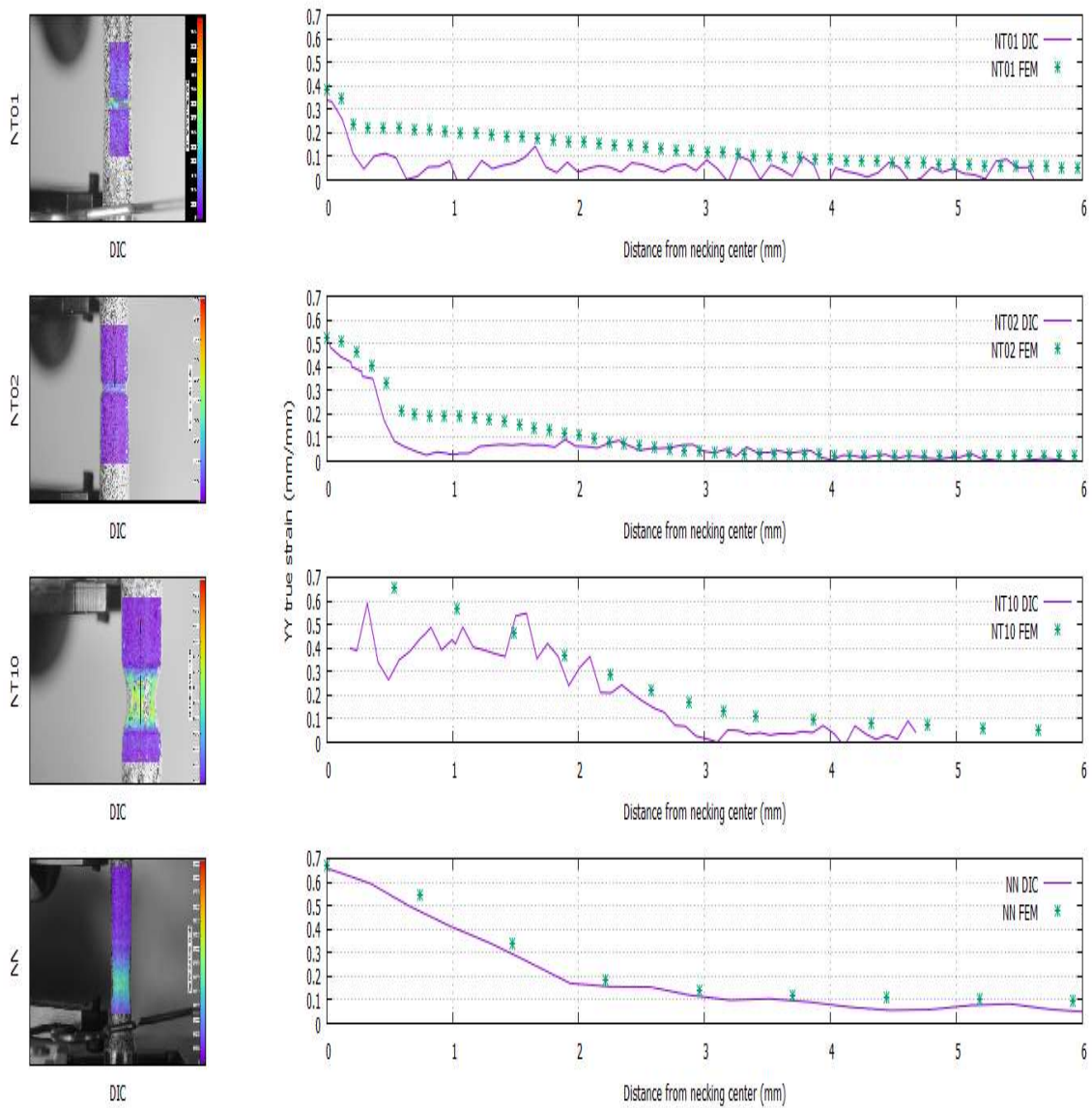
Source: Personal file.

5.2.2. Material model validation

The material model validation was performed by comparing the measured and numerical strain fields on both notched and unnotched, tensile and bending specimens as well as comparing the predicted force-displacement relation of 3-point-bending test. The measurement of strain field was performed using DIC (Digital Image Correlation) and INSTRA 4D software allowed recording the strains on a predefined path. The results were then compared to FEM analysis, just prior to fracture.

In both FEM and DIC analysis, a vertical line centered in the specimen was set on the undeformed body and the measurements of longitudinal true strains (ϵ_{YY}) were based on it. The results for all DB specimens are shown in Figure 72. It was observed that experimental measurements in strain field along the necked area of the specimens were also in good agreement with numerical predictions. Despite the fact that only one camera was used to image acquisition, specimens NN, NT10, NT02 and NT01 presented similar results for FEM and DIC analysis.

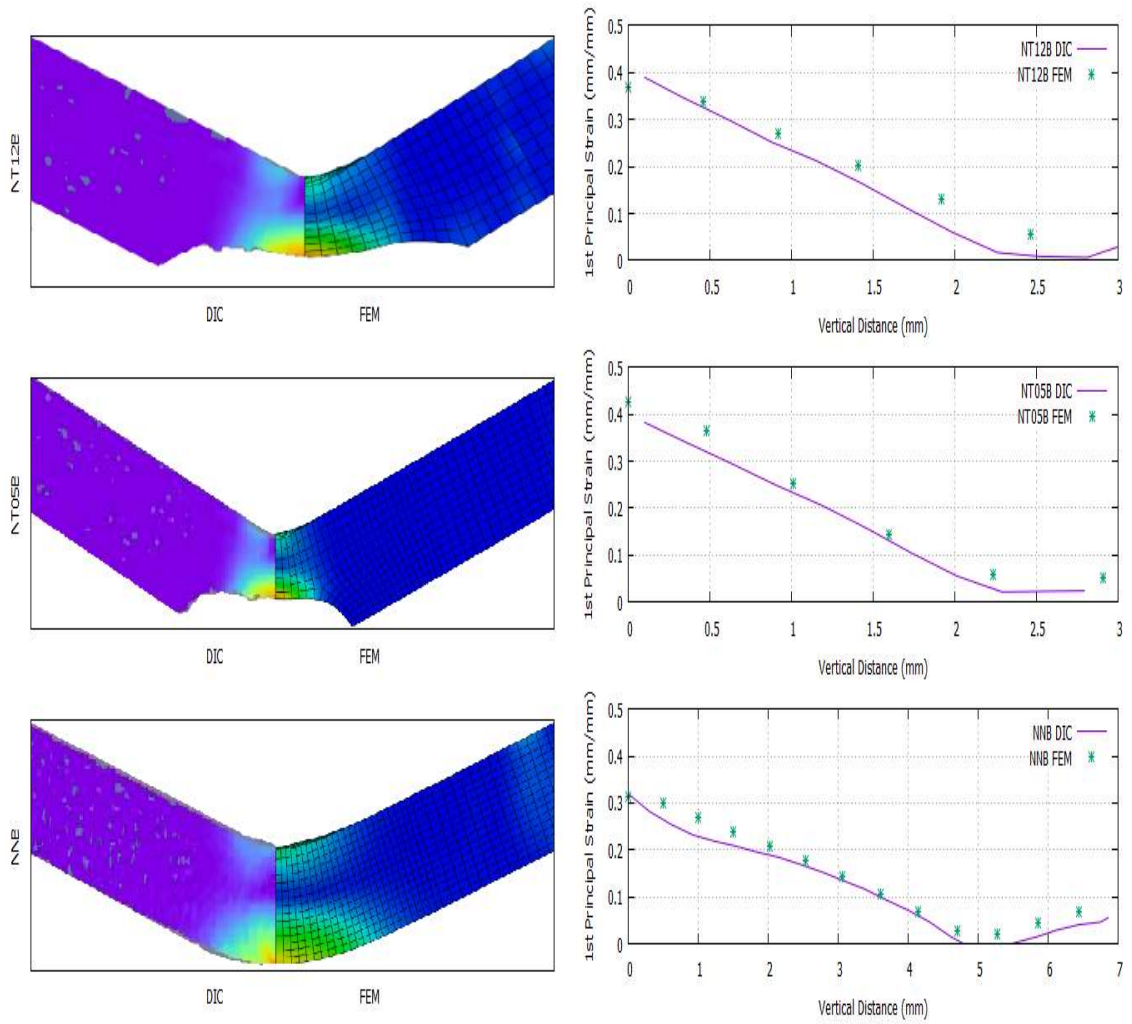
Figure 72 - Numerical predicted axial strain field in comparison to its experimentally measured results in DBs specimens



Source: Personal file.

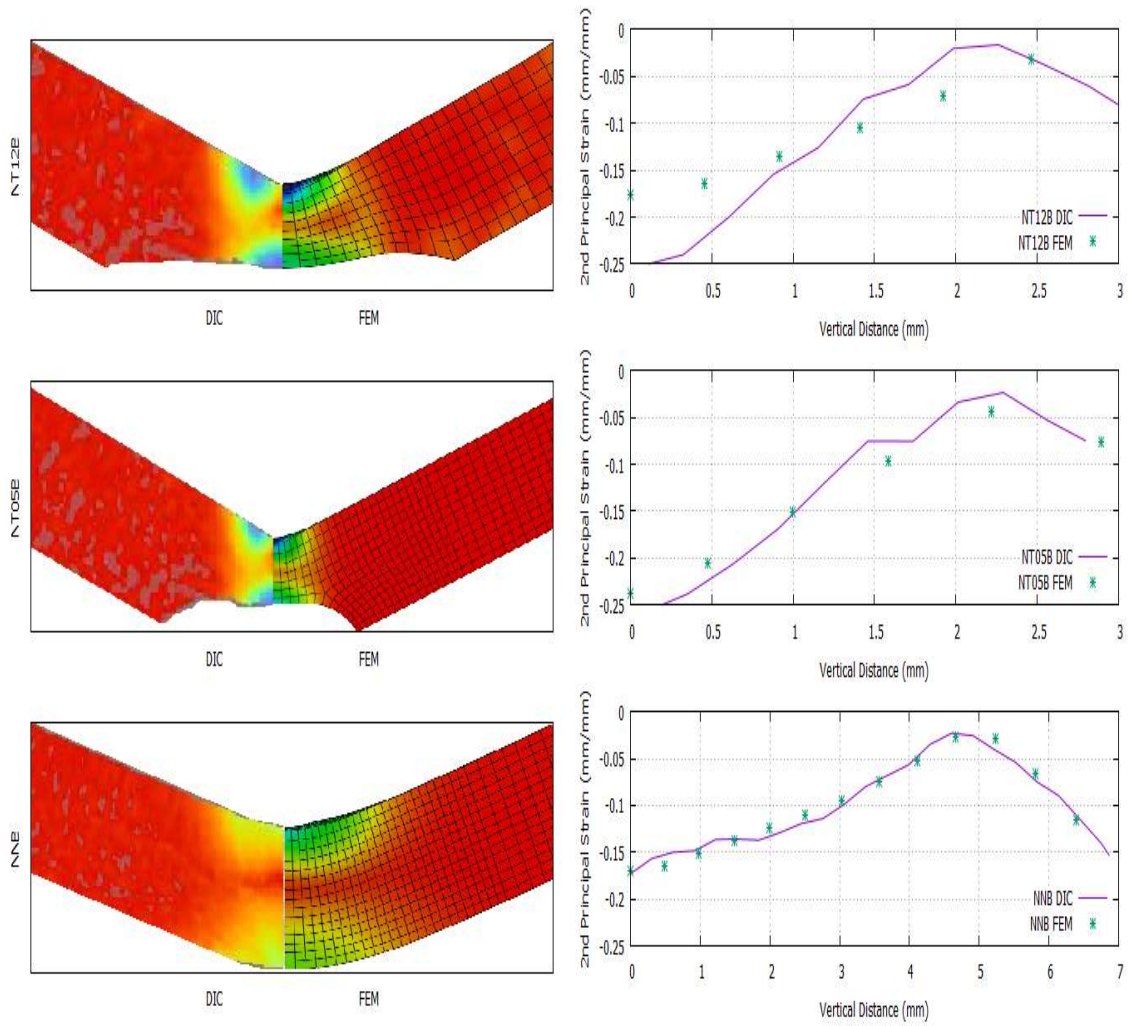
The same previous steps were repeated for the 3-point bending specimen. Measurements of strains were performed from the bottom to the top on a vertical line centered in the middle of the beam body. Results are shown in Figure 73 and Figure 74, comparing the first and second principal strains in the beam body both by FEM and DIC analysis.

Figure 73 - Numerical predicted 1st principal strain field in comparison to its experimentally measured results at failure onset



Source: Personal file.

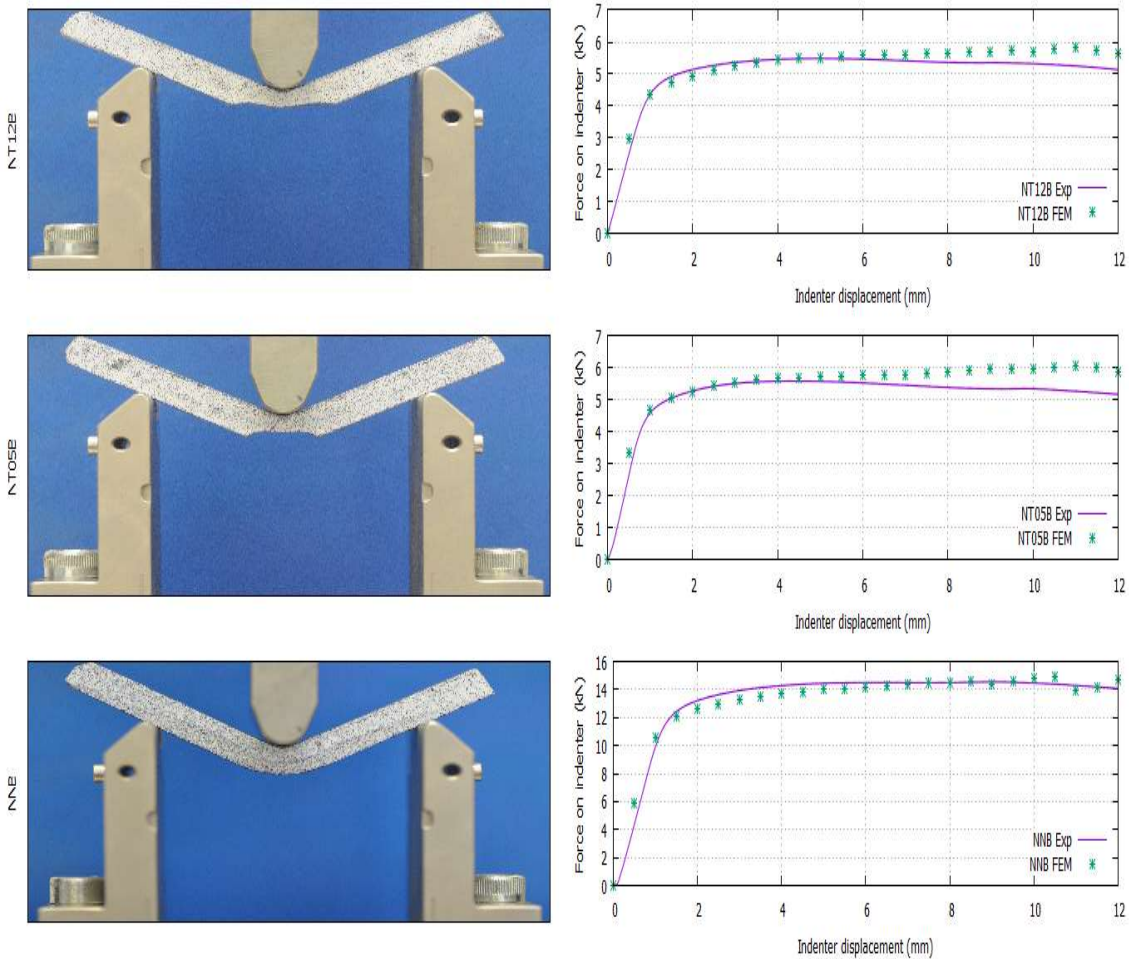
Figure 74 - Numerical predicted 2nd principal strain field in comparison to its experimentally measured results at failure onset



Source: Personal file.

The predicted load-displacement on the indenter comparison with experimental results are shown in Figure 75.

Figure 75 - Comparison of experimental and FEM simulation of force-displacement curves in 3-point-bending tests



Source: Personal file.

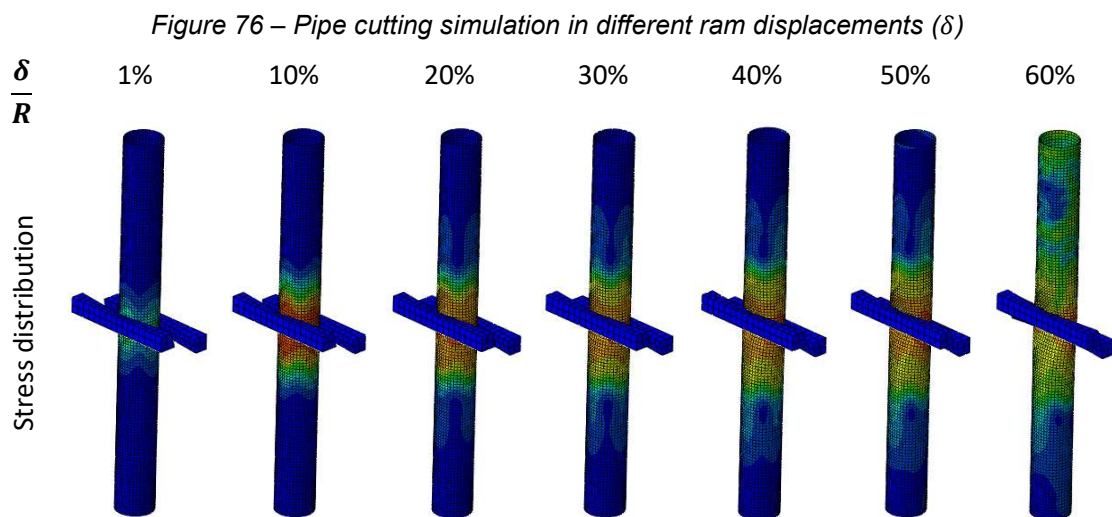
The obtained parameters for API S135 presented good adherence as it can be observed in Figure 73 (1st principal strains), Figure 74 (2nd principal strains) and Figure 75 (force-displacement), in which 3-point-bending experimental testing specimens are compared to numerical simulation. Except for the second principal strain in NT12B specimen, numerical simulation could predict experimental results with a good accuracy using the calibrated model parameters.

5.3. Pipe cut in BOP analysis

This section describes modeling and validation of pipe cut in BOP. A focus is given to 6 5/8" 40.87ppf drill pipe (DP), which is the largest cross sectional area tube used in Petrobras drilling fleet. Moreover, it is one of the most cut pipes due to contractual requirements. For such DP it was found a large collection of photographs and records of cutting tests pressure spectra. The numerical models provide means to understand the cutting process and are validated using experimental data.

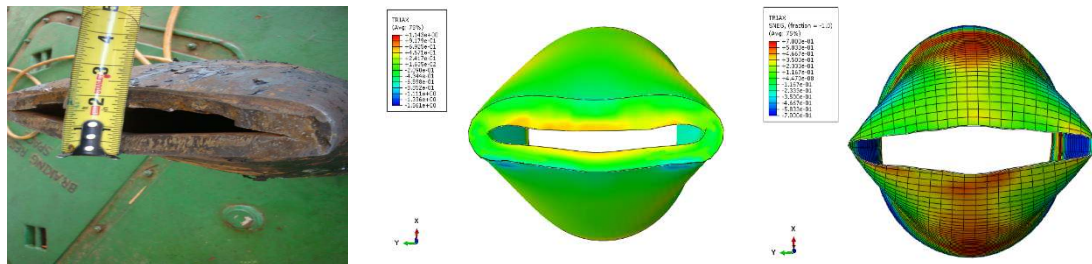
5.3.1. Numerical modeling

Numerical simulations of pipe cut in BOP were performed using the defined geometry and the calibrated material parameters as illustrated in Figure 76. According to Castilho (2016) [32] the pipe cut in BOP model converges with a tubular meshing of 3 elements per wall thickness, however simulations in these conditions are still computational and time costly, unfeasible to construct the metamodel.



In order to make feasible several simulations in parallel a strategy to simplify the numerical model using a mesh constituted by shell elements (1 element per wall thickness) was proposed. A comparison of experimental cut pipe with numerical FEM using hexagonal elements mesh (3 elements per wall thickness) and shell elements is illustrated in Figure 77.

Figure 77 – 6.63" 40.87ppf drill pipe after cut



Source: Personal file.

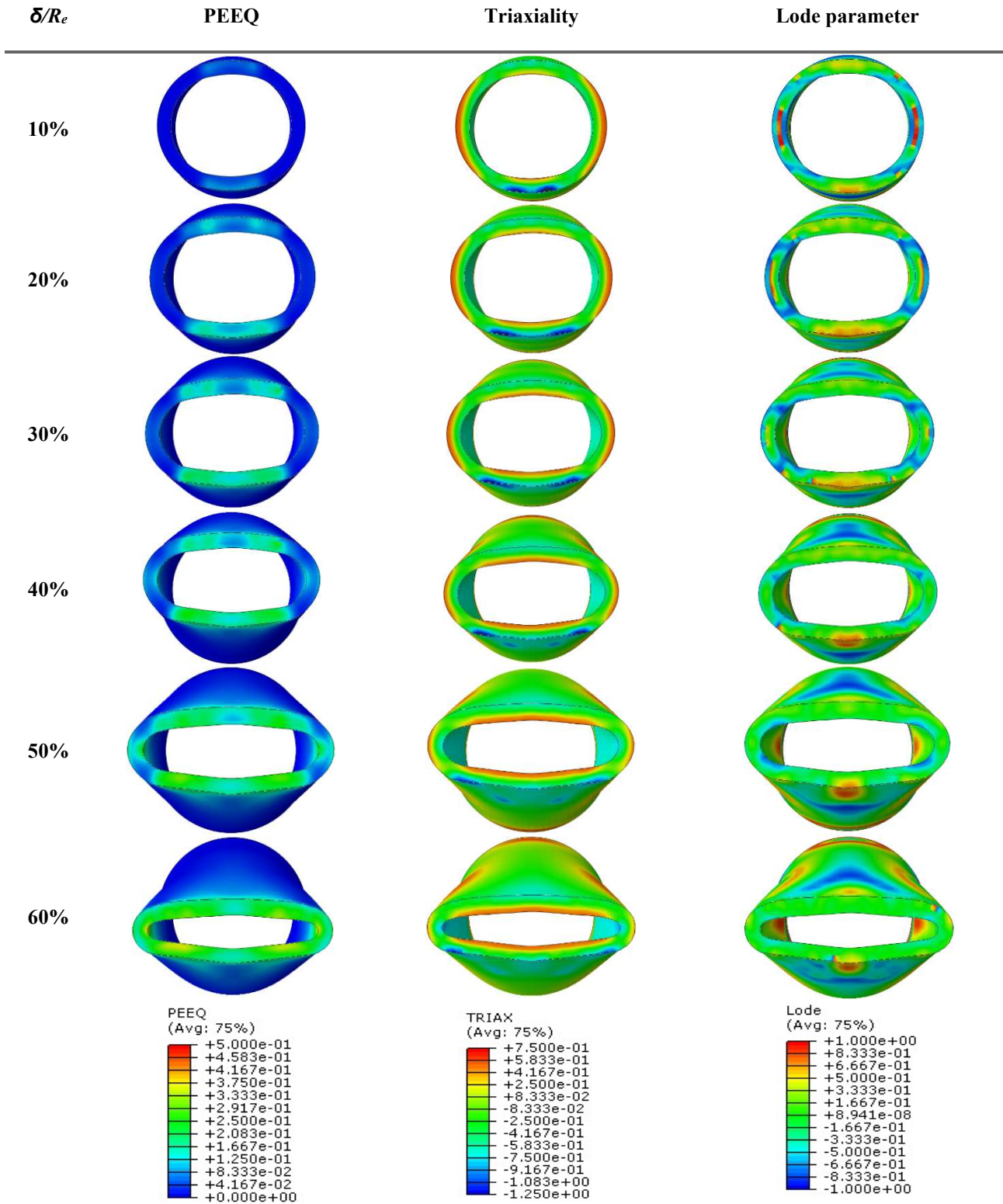
A stress analysis was performed to validate the shell element model. Simulations of cutting pipe under different project variables using hexagonal elements mesh with 3 elements per wall thickness were done to investigate changes in the cutting mechanism.

5.3.1.1. Stress analysis during cut process

Numerical simulations can provide information of the stresses and failure mechanism. Thus, a numerical analysis of the stress state on the fractured cross section of the previous 6 5/8" 40.87ppf tube was performed. Figure 78 shows the distribution of triaxiality, Lode parameter and equivalent plastic strain (*PEEQ*) along the fractured cross-sectional area during the process of pipe cutting. It is shown in the analysis that, the pipe first flattens in the region in contact with the ram and a plastic hinge is formed in its extremities. The plastic strains are higher in the hinge, and when it cannot support any further strains, it cracks internally. It is also observed in Figure 78 that in the region of the pipe in contact with the rams, negative triaxialities are in the external side and positive triaxialities are in the internal side of the tubular cross section, as a bending process in a beam.

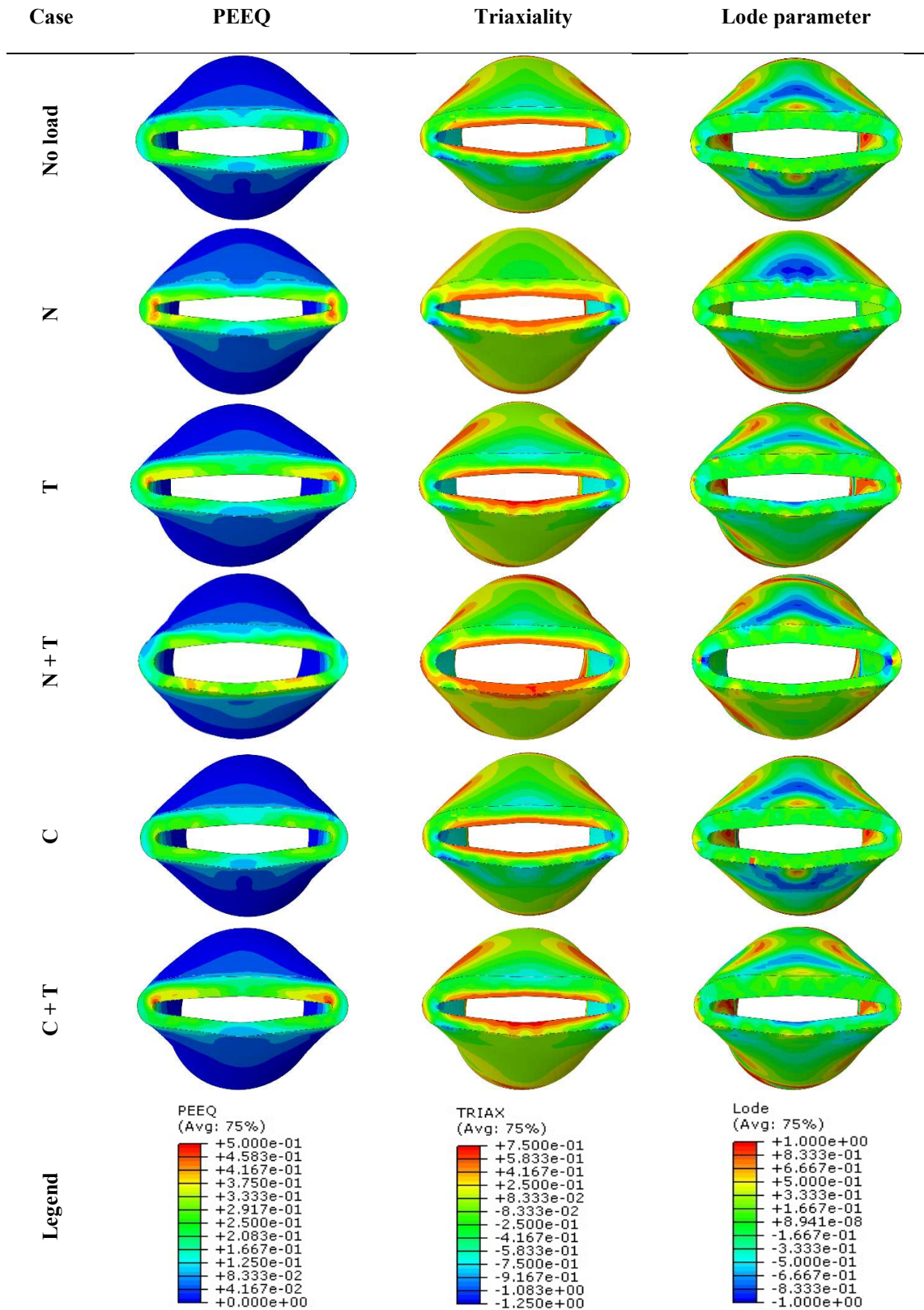
Simulations with different project variables present similar stress states. Stresses were uniformly applied to unrestricted upper edge of the tube, where $N = 400\text{MPa}$, $T = 300\text{MPa}$ and $C = -10\text{MPa}$. Results are shown in Figure 79 and it is observed that despite the variations of project variables, the distribution of the stress invariants remains similar concentrating high triaxialities in the internal part of the tube.

Figure 78 - Numerical predicted PEEQ and triaxiality field in cut cross section of 6.63" 40.87ppf drill pipe in no load condition along process of cut



Source: Personal file.

Figure 79 - Numerical stress analysis in cut cross section of 6.63" 40.87ppf drill pipe for different project variables at onset of pipe cut



Source: Personal file.

5.3.2. Model validation

The numerical model and obtained results for no load condition are validated using fractography analysis. Comparison to experimental measurement of force to cut and final geometry of the pipe are made.

5.3.2.1. Qualitative microfractography analysis

Analysis of the fractured area of a 6 5/8" 40.87ppf drill pipe shows agreement with the numerical results. Figure 80 presents microfractography scanning electron microscopy (*SEM*) images using secondary electrons emission. Each image is associated with local measured microhardness (*HC*) and numerical results (*PEEQ*, triaxiality and Lode parameter) for nine different points distributed in the cross section as indicated, where 0° axis coincides with the indenter displacement direction. The chemical composition of the sample measured by EDS is presented in Table 19.

Table 19 – Measured chemical composition by EDS for the cut tube

Source	Si	Mn	P	S	Cr	Mo
API Spec 5D, 2000	-	-	<0.015	<0.030	-	-
Tested samples	0.4	0.8	0.02	0.06	1.0	0.5

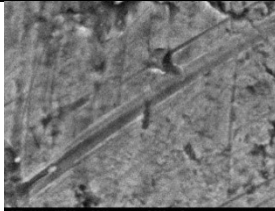
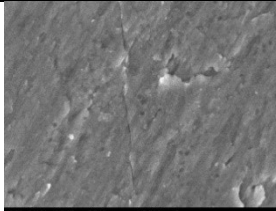
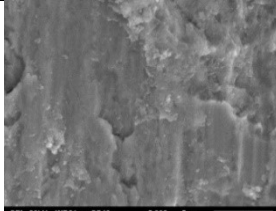
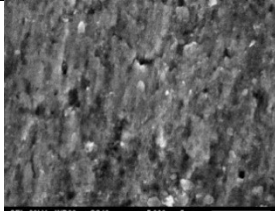
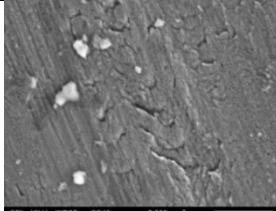
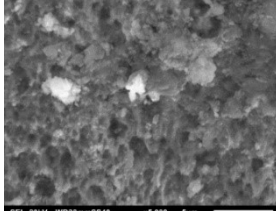
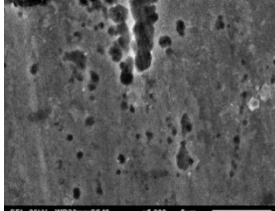
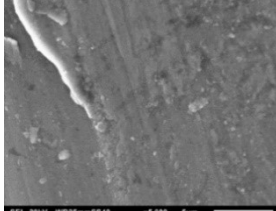
Source: Personal file.

The qualitative microfractography studies suggest that failure was a tear process, i.e., Mode I dominated. Prior to fracture initiation, the numerical results did show that Lode angle parameter and triaxiality are almost constant and null throughout most of the tubular solid cross section, except in its interior in a region between 0° and 45°. There, high triaxialities were found.

The numerical results revealed a good correlation with the surface rugosity. Indeed, over nine measured points, regions with high triaxiality, as predicted by the numerical model, coincided with spherical equiaxial dimples. Regions of low triaxialities are smooth, have stretch marks and parabolic dimples

[95]. Additionally, it was observed that the measured hardness in fractured surface increases proportionally to the PEEQ gradient, in agreement with the plastic strain gradient hardening theory [96] [97].

Figure 80 - Comparison of surface microscopy, microhardness and FEM measurements in the cross-sectional area of a 6 5/8" 40.87ppf tubular

		Angular position			
		0°	45°	90°	
Radial position	External	SEM 5000X			
		HC (HRC)	35.5	40.5	44.2
		PEEQ	0.17	0.21	0.24
		η	-0.70	-0.30	0.42
		ξ	0.15	0.31	0.28
	Middle	SEM 5000X			
		HC (HRC)	35.8	43.1	46.0
		PEEQ	0.14	0.30	0.12
		η	0.43	0.07	-0.30
		ξ	-0.17	-0.10	0.25
	Internal	SEM 5000X			
		HC (HRC)	38.0	39.9	46.5
PEEQ		0.25	0.35	0.41	
η		0.50	0.50	-0.89	
ξ		-0.11	-0.23	-0.22	

Source: Personal file.

The findings here reported go along with the main results of Wierzbicki and Suh model (1988). The tube is seen as assembled by longitudinal beams (generators) which suffer bending due to the indenter contact. Voids are nucleated until failure by coalescence, as highlighted by the SEM images in internal/middle radial positions with angular positions 0° and 45° . This goes side by side with the increase of triaxiality at the internal part of the tube. It should be noticed that the upper triaxiality magnitude predicted by the numerical simulations is within the experimental limits and that failure by bending was validated by experimental tests.

5.3.2.2. Cut pipes geometry

The geometry of cut pipes by FEM simulations are compared to experimental results as reported in Attachment E. For each pipe register, it was measured the lengths of principal directions $OD1$ and $OD2$ of the cut pipe as illustrated in Figure 81. The experimental measurements and comparison to FEM results are summarized in Table 20 and illustrated in Figure 82.

Figure 81 – Pipe geometry after cut in BOP



Source: Extracted from [26].

Table 20 - Comparison of sheared pipe geometries through experimental and FEM numerical results

#	Exp. OD1 (mm)	FEM OD1 (mm)	Dev. OD1 (%)	Exp. OD2 (mm)	FEM OD2 (mm)	Dev. OD2 (%)
1	115	118	2,6	52	35	-32,7
2	125	138	10,4	68	30	-55,9
3	210	189	-10,0	60	42	-30,0
4	215	212	-1,4	40	42	5,0
5	221	233	5,4	78	54	-30,8

Source: Personal file.

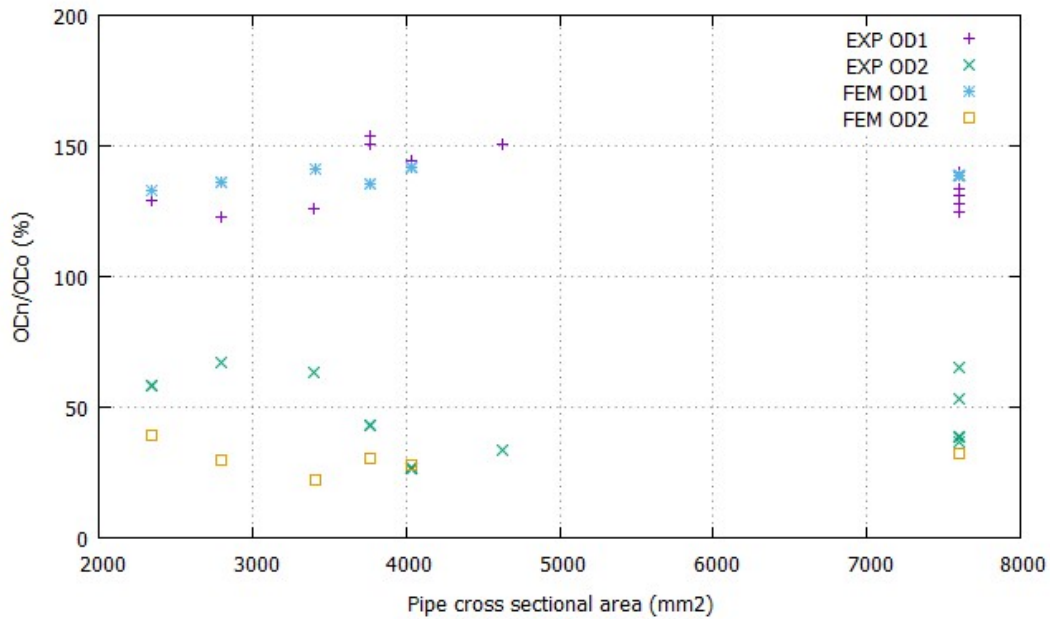
It is observed that the relation between the principal dimensions $OD1$ and $OD2$ of different cut pipes and the undeformed pipe external diameter OD remained constant. The largest principal dimension $OD1$ of the cut pipe is 40% greater than the undeformed diameter, as well as the smaller principal dimension $OD2$ is about 50% of the original pipe diameter for a wide range of tubulars, as it can be seen in Figure 82, indicating that strain at failure is constant. Numerical simulations could capture the same tendency.

This observation can be interpreted as the inextensibility of infinitesimal cross sections that constitutes the pipe. Considering that the cut cross section of the pipe is fitted by a lozenge as a result of the “V” shape indenter, the ratio of the cut pipe perimeter (PL) with the tubular circular perimeter (PC) is given by,

$$\frac{PL}{PC} = \frac{2\sqrt{OD_1^2 + OD_2^2}}{\pi OD} = 95\% \quad (64)$$

Using the average values of $OD1$ and $OD2$ reported, it is shown that cross section pipe perimeter remains inextensible during deformation and cutting of the pipe. Once the perimeter remains inextensible, it is reasonable to assume that the pipe cross sectional area and wall thickness also remains constant, which supports the use of shell elements.

Figure 82 – Comparison of numerical and experimental plot of principal dimensions of the sheared pipe with respect to the original pipe diameter (OD_0)



Source: Personal file.

5.3.2.3. Numerical and experimental comparison of ultimate required force to cut different pipes in BOP

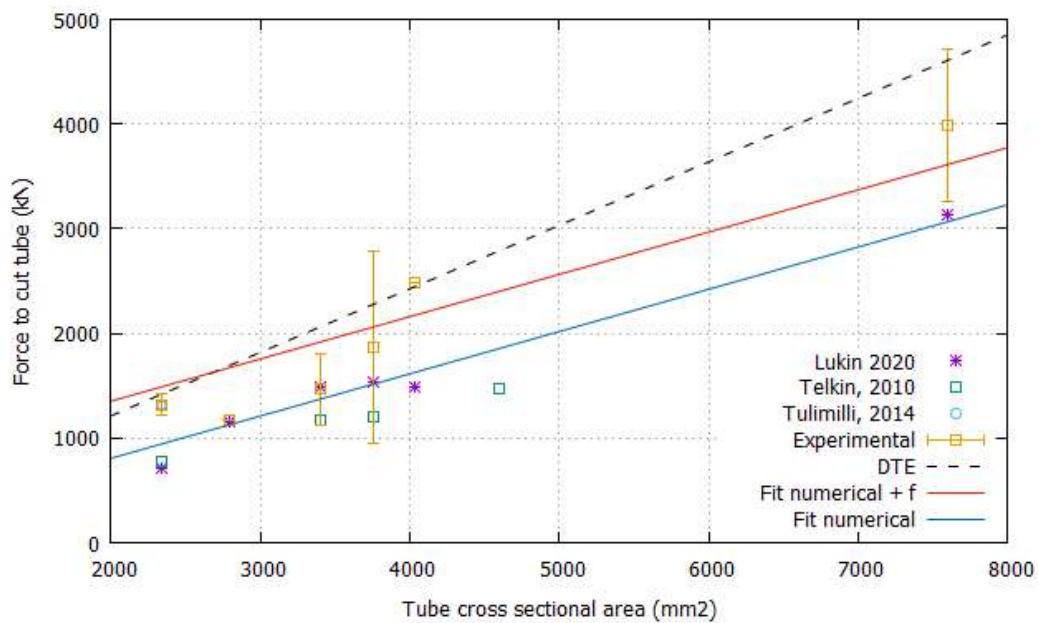
The results of required forces to cut tubes of different cross section area S_t comparison for DTE (F_{DTE}), FEM (F_{FEM}) and experimental (F_{EXP}), including its statistical standard deviation ($F_{exp SD}$) are listed in Table 21 and are plotted in Figure 83. The scattering in experimental data of cutting forces occurs due to different BOPs used, few standard metallurgical requirements for API S-135 steel and uncontrolled variables in BOP commissioning testing procedures (such as pipe length and bore centralization). Although, as expected by DTE model, numerical results for cutting force are proportional to the cross-sectional area.

Table 21 - Summary of experimental and numerical results of pipe cut forces

Pipe	S_t (mm ²)	F_{DTE} (kN)	F_{FEM} (kN)	F_{exp} (kN)	F_{exp} SD (kN)
1	2336.1	1416.2	712	1320.2	105.7
2	2788.1	1690.2	1153	1179.0	-
3	3403.0	2063.0	1480	1466.3	341.5
4	3760.1	2279.4	1542	1862.3	915.3
5	4034.5	2445.8	1489	2482.0	-
6	7600.6	4607.6	3138	3980.6	729.3

Source: Personal file.

Figure 83 - Required force to shear a pipe x pipe cross sectional area: FEM x experimental results



Source: Personal file.

The difference of numerical and experimental results is attributed to internal frictional forces in BOP. It is assumed that they are independent of the pipe size, such that,

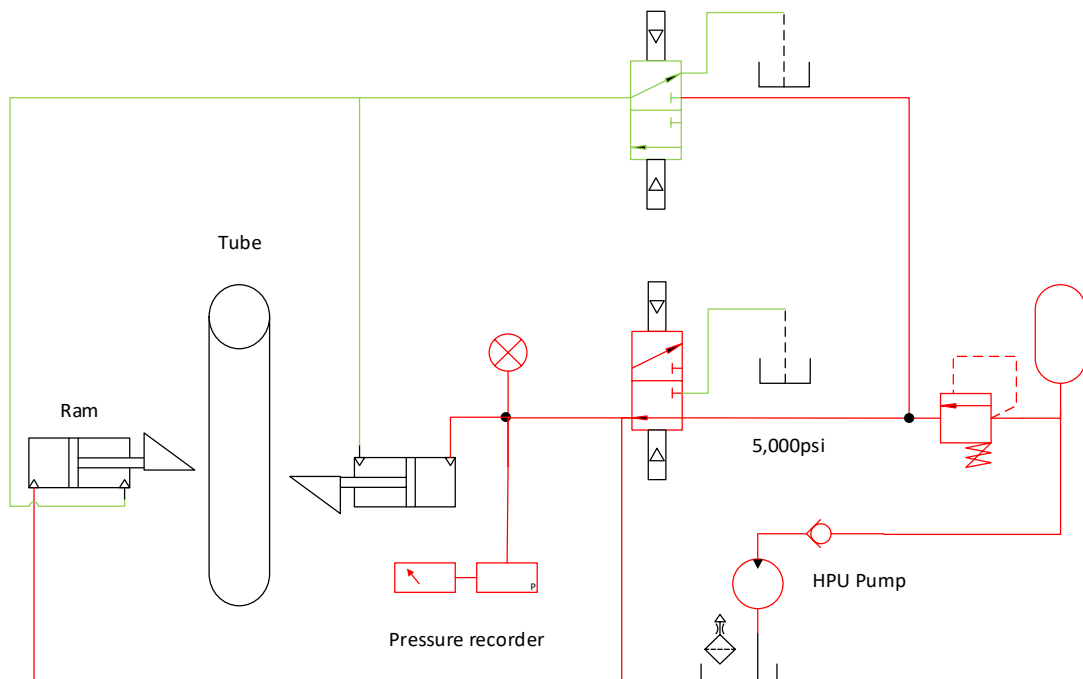
$$F_{exp} = k_f S_t + f \quad (65)$$

where k_f is a coefficient to be adjusted ($0.405 \frac{kN}{mm^2}$), f is the BOP internal frictions ($545kN$) and S_t is the tubular solid cross section area. According to numerical simulations of pipe cut, the relation between measured force and pipe cross section area is 66% from the obtained by DTE model, indicating that stress concentrators reduce the required force to cut the pipe.

5.3.2.4. Numerical and experimental comparison of force on indenter during 6 5/8" 40.87ppf pipe cut process

In some BOP commissioning experiments, the pressure on the closing chamber of the ram piston was recorded during the shear testing. The used arrangement is illustrated in Figure 84, where green lines represent vented (atmospheric) pressure and red lines are pressurized with 5000psi. Force on the indenter is obtained by multiplying measured pressure by the piston area.

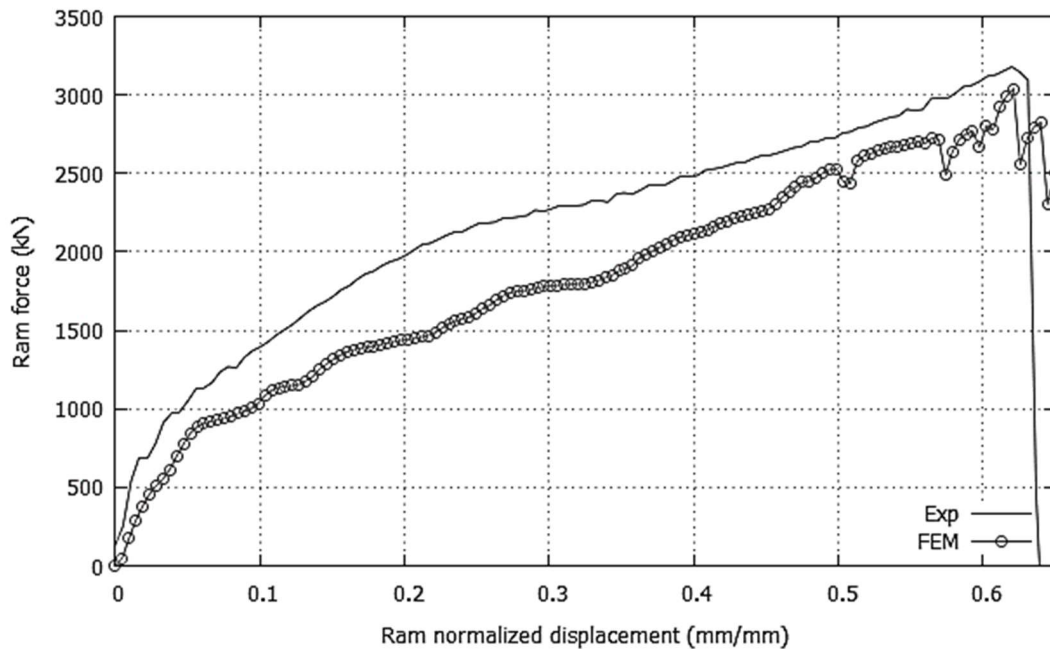
Figure 84 – Experimental arranged used to measure pressure on the closing chamber



Source: Personal file.

A comparison of numerical and experimental results for instantaneous force on indenter during a 6.63" 40.87ppf DP cut was performed. It was found a good agreement between the ram force - normalized displacement predicted by FEM model and experimental test, as shown in Figure 85. For this comparison, the experimental calculated force was discounted by the friction force f and the ram position was determined considering its velocity constant during the measured closing time of 17s. To present the results, the ram displaced is normalized by using the ratio of ram displacement δ to the undeformed pipe external radii D_e .

Figure 85 - Normalized displacement for 6.63" 40.87ppf drill pipe cut in BOP



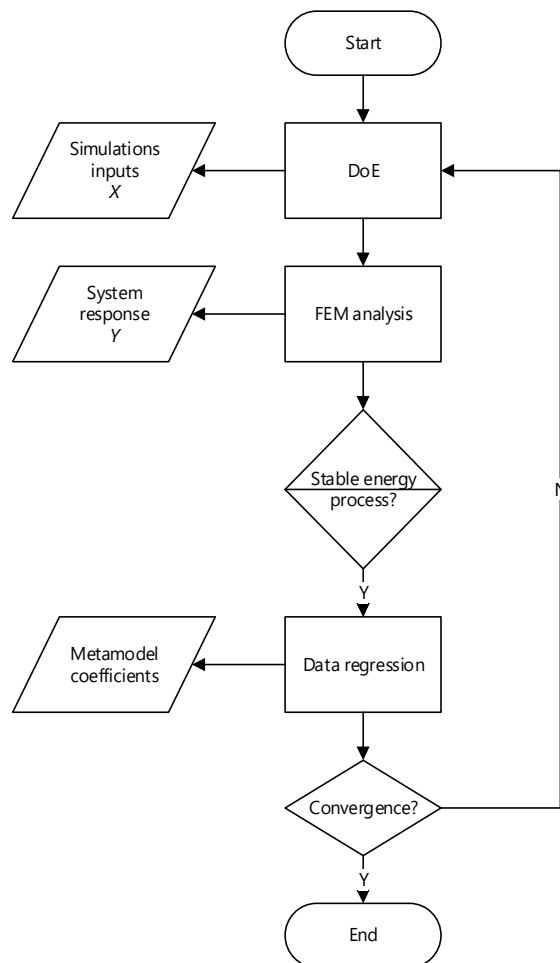
Source: Personal file.

The profile of the pipe cross section after failure is similar to the one simulated in FEM, as seen in Figure 77. The horizontal and vertical main dimensions were 222x62mm for experimental test and 219x62mm for numerical model (both in 63% of ram normalized displacement). Once the material and the numerical models for the pipe cut in BOP are defined and validated, the next step is to simulate the pipe cutting under different project variables to generate sufficient data to build the metamodel.

5.4. Metamodel construction

The metamodel is constructed in three stages: design of experiments (DoE), computational evaluation of the models (Abaqus) and data analyses (metamodel parameters). At the first stage, the definition of the different project variables are established according the proposed LHS and the input files for FEM analyses are developed. Then, all models are simulated with the FEM software ABAQUS. The recorded outputs are the necessary force to cut the 6.63" tube and the energy balance during the process. If the energy is numerically stable, the model is valid and the force is considered in the construction of the metamodel. All steps of the process are illustrated in the flowchart in Figure 86.

Figure 86 - Process flowchart for metamodel construction



Source: Personal file.

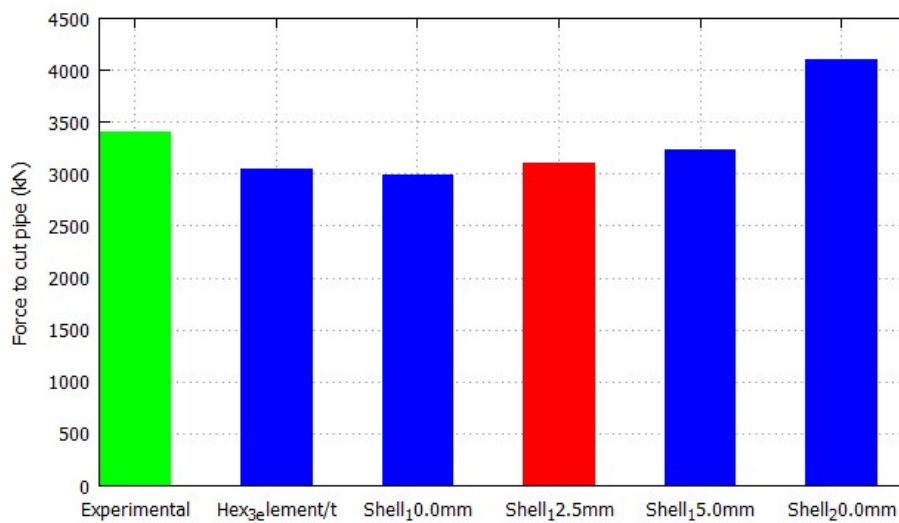
5.4.1. Numerical data generation

This section describes the process of generating valid data for constructing the metamodel.

5.4.1.1. Mesh convergence

A systematic mesh study was performed to check the influence of the element size in the model response. The numerical results of different mesh sizes, including solid and shell elements, are compared to experimental average force. The results are illustrated in Figure 87.

Figure 87 - Mesh convergence study



Source: Personal file.

It is observed, the numerical results tend to converge as the mesh is refined. Considering the computational cost and precision, the model with 12.5mm shell elements was chosen to generate the data for constructing the metamodel. With such model it was possible to simulate in batches of 60

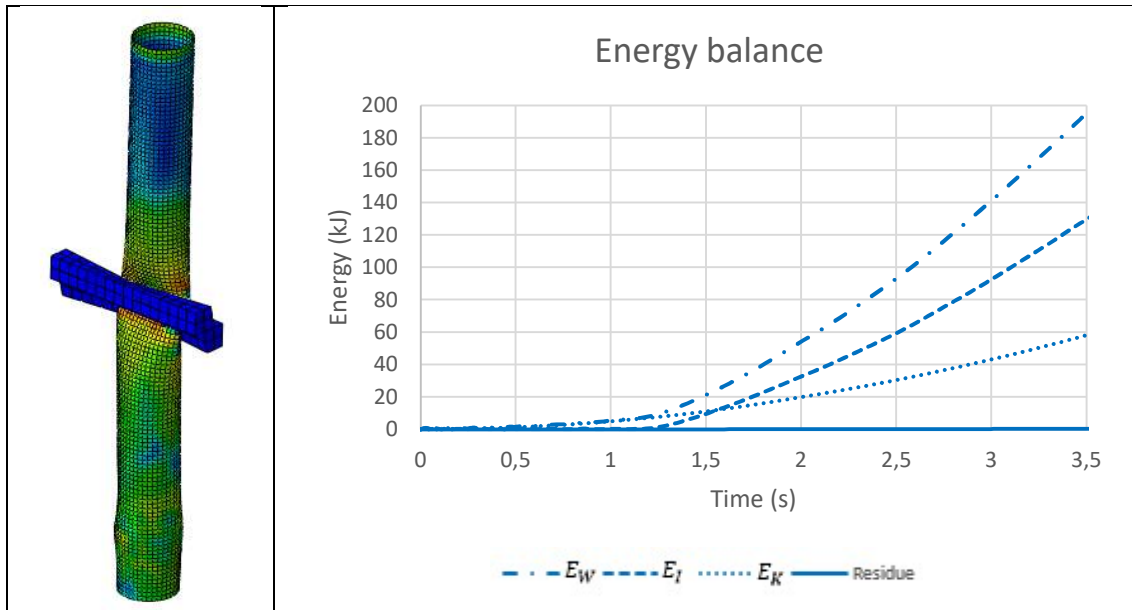
simulations in parallel, lasting 5 days each batch. A total of 5 batches were run to provide enough data for 8 iteration cycles consuming approximately one month.

5.4.1.2. Energy balance in the simulations

Energy balance is checked for every simulation performed, once imposed boundary conditions can cause instabilities, such as buckling and shear locking effects on numerical model, which can lead to imprecise results. For each simulation with a given project variables set, result compatibility is verified by means of first law of thermodynamics, which states that the total energy of a closed system is constant. Therefore, external work (E_W) performed by shear rams should be equal to internal (E_I) and kinetic (E_K) energy of the system as indicated in Attachment A. Once the energy balance is calculated for a numerical model, a residual difference is tolerable if it is relatively small in comparison to other terms.

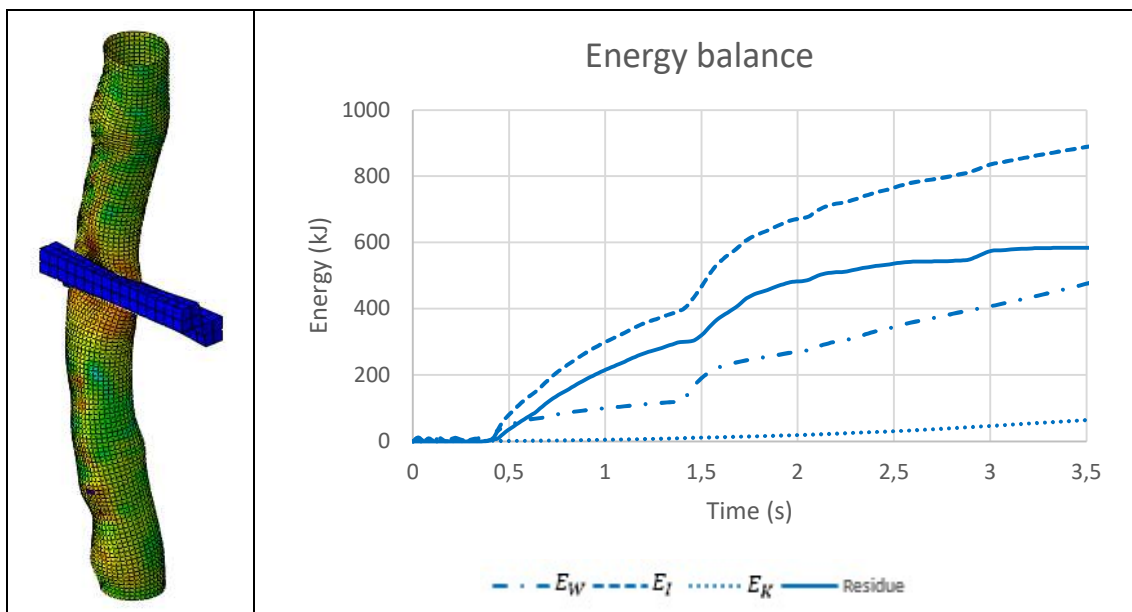
Examples of compatible and incompatible simulations are illustrated in Figure 88 and Figure 89 respectively. As it can be seen, beyond the energy balance the tubular shape indicates the energetic compatibility. Incompatible simulations are discarded and are not used to feed the machine learning algorithm.

Figure 88 – Example of energy balance for compatible boundary conditions



Source: Personal file.

Figure 89 – Example of energy balance for incompatible boundary conditions



Source: Personal file.

5.4.2. Machine-learning

With the numerical model parameters already defined, sets of designed simulations according to the proposed LHS method are performed. For each simulation satisfying the energy balance, the ultimate force to cut the pipe is used

to feed the machine-learning algorithm. The simulation results are listed in Attachment F and the amount of compatible simulations used to feed the machine-learning algorithm on each iteration cycle is summarized in Table 22. A number of 188 valid simulations were obtained and split into $N_{sim_{train}}$ training set (70% of total amount) and $N_{sim_{test}}$ test set (30% of total amount), which includes:

- the inputs $X \in \mathbb{R}^{7 \times 188}$, each input i is a vector $x^i \in \mathbb{R}^{7 \times 1}$;
- the outputs $Y \in \mathbb{R}^{1 \times 188}$, each output i is a scalar y^i with the value of the force necessary to cut the tube when the conditions x^i occur.

Table 22 - Compatible simulations as a function of iteration cycles

Iteration cycle n	Simulations performed	Compatible simulations	$N_{sim_{train}}$	$N_{sim_{test}}$
5	33	24	19	5
6	65	48	34	14
7	129	94	66	28
8	257	188	132	56

Source: Personal file.

In order to avoid bad conditioning, both input and output variables are pre-processed by normalizing it with the equivalent fracture parameters (Table 23). Such normalization intends to give a physical meaning by beaconing the loads to other pipe failure mode.

Table 23 - API S-135 6 5/8" 40.87ppf tube fracture properties obtained from tube manufacturer

Property	Symbol	Value	Unit
Tube traction to rupture	N_u	9236.3	kN
Tube pressure capacity	$P_{i,u}$	204.9	MPa
Tube collapse pressure	$P_{e,u}$	207.6	MPa
Tube torque to rupture	T_u	3.60E+08	N.mm

Source: Personal file.

The normalized values are defined in Table 24 and are indicated with * symbol. The sets of $(N^*, T^*, P_i^*, P_e^*, h^*, d^*, F^*)$ vectors are analyzed through the machine learning algorithm which releases the metamodel parameters.

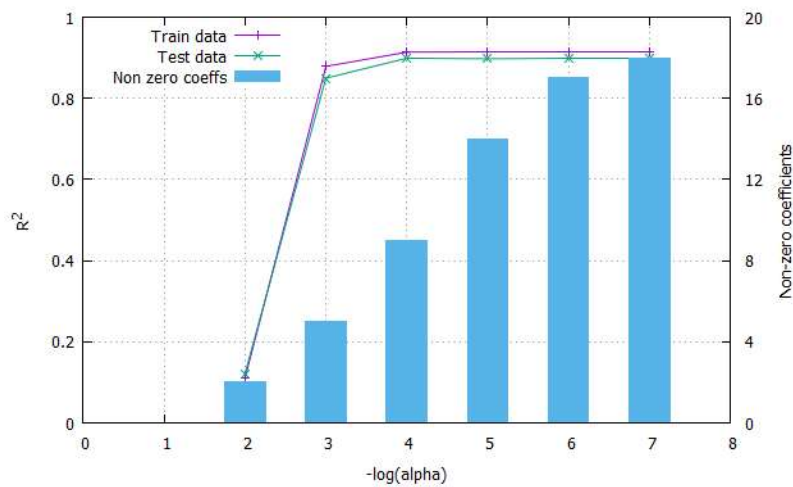
Table 24 - Normalized input variables

Variable	Normalization
Required cutting force	$F^* = \frac{F}{N_u}$
Tubular tension	$N^* = \frac{N}{N_u}$
Tubular torque	$T^* = \frac{T}{T_u}$
Tubular internal pressure	$P_i^* = \frac{P_i}{P_{i,u}}$
Tubular external pressure	$P_e^* = \frac{P_e}{P_{e,u}}$
Indenter offset	$h^* = \frac{h}{h_{max}}$
Tubular centralization	$d^* = \frac{2d}{OD}$

Source: Personal file.

A polynomial regression of order $Q = 3$ is chosen to represent the metamodel with 19 coefficients to be determined. Initially, the tuning for ElasticNet is performed to optimize accuracy and model complexity. It was chosen $\alpha = 10^{-4}$ and $\gamma = 0.5$ due to R^2_{train} maximization with the minimum number of non-zero coefficients. The tuning result is shown in Figure 90.

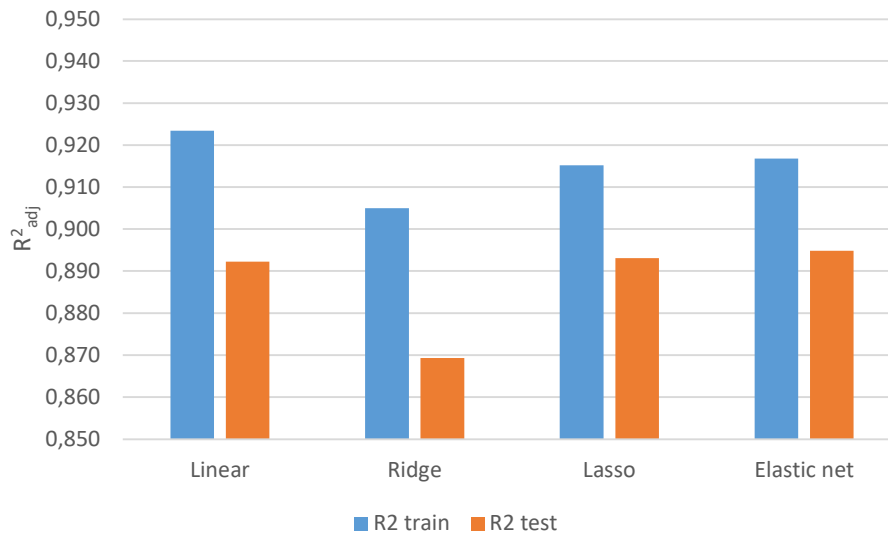
Figure 90 – ElasticNet tuning



Source: Personal file.

A comparison of different data analysis models is performed. The model fitting, generalization and complexity are measured by R_{train}^2 , R_{test}^2 (using a fraction of 30% of data) and number of non-zeros coefficients respectively. Metamodels determined by OLR, Ridge, Lasso and ElasticNet are compared in Figure 91.

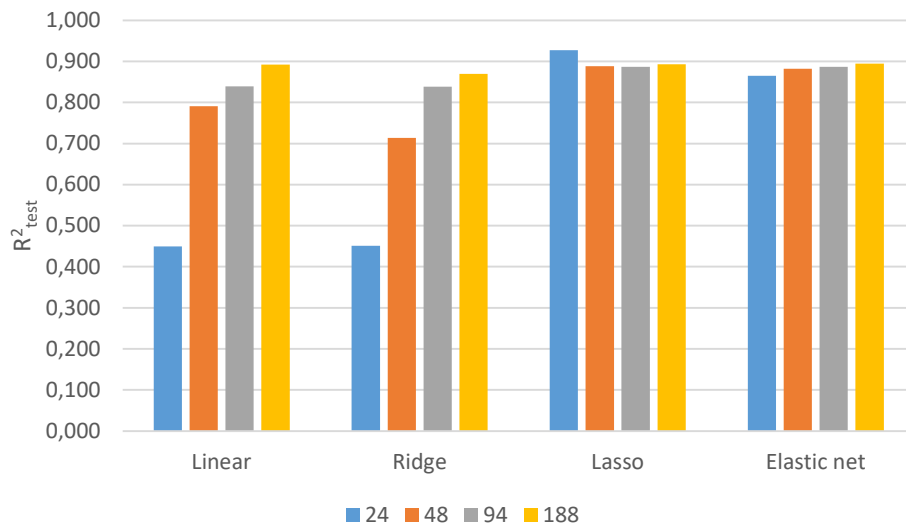
Figure 91 – Accuracy x generalization for different models of data analysis



Source: Personal file.

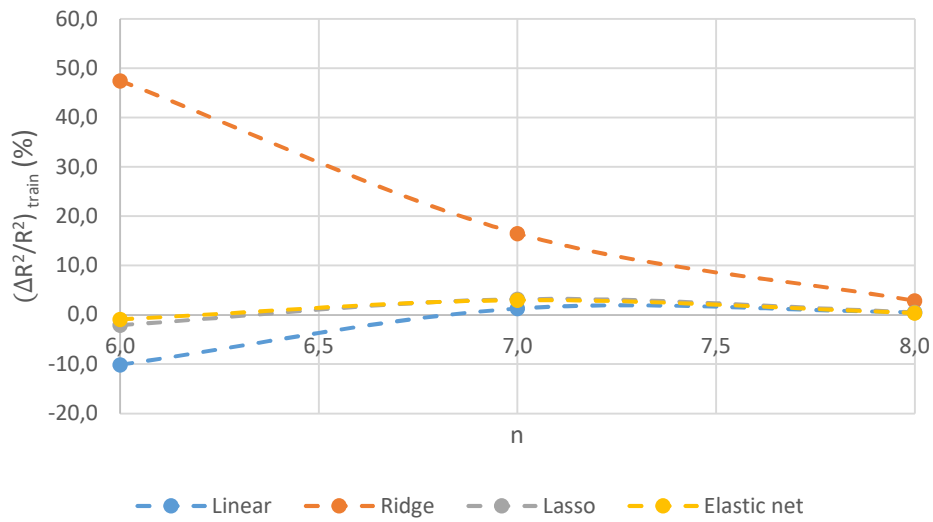
The convergence of metamodel parameters is also compared for different data regression models with a progressive number of input points as iteration cycles n increase. Model fitting accuracy and rate of convergence as previously defined for training data are shown in Figure 92 and Figure 93 respectively. Similar analysis is performed for generalization and its convergence using test dataset in Figure 94 and Figure 95. Models complexity comparison measured by number of non-zero coefficients (p) is shown in Figure 96. Despite all models tend to converge, it is observed that Lasso and ElasticNet models converge faster with smaller datasets.

Figure 92 – Metamodel training accuracy for different analysis models and iteration cycles



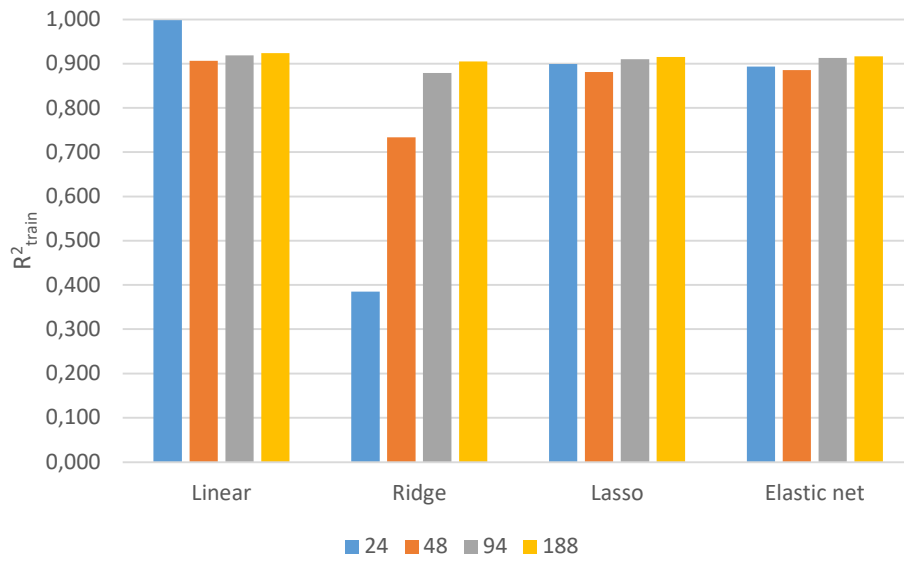
Source: Personal file.

Figure 93 – Rate of convergence for different analysis models using train data



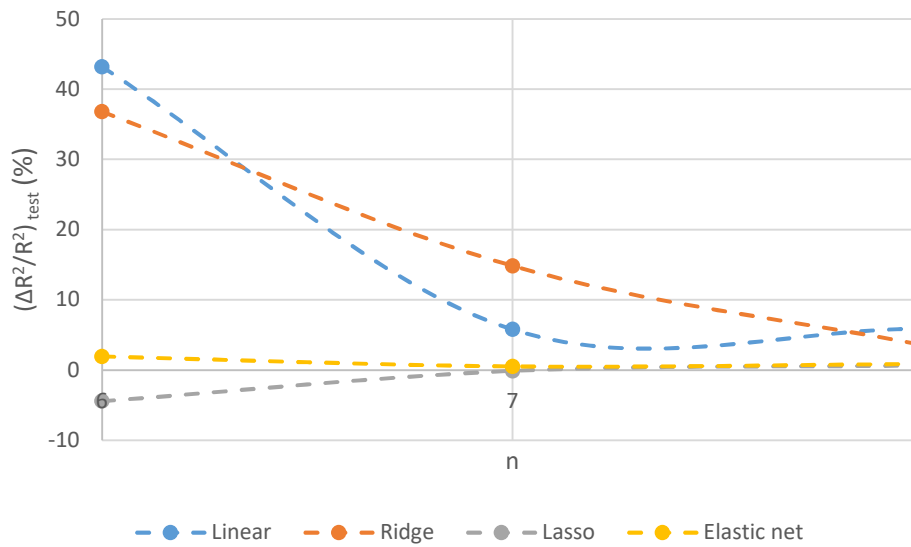
Source: Personal file.

Figure 94 – Metamodel generalization accuracy for different analysis models and iteration cycles



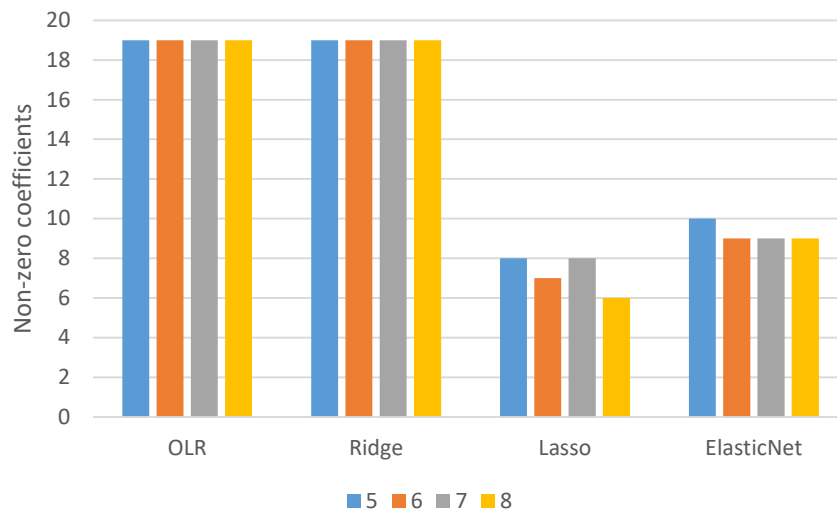
Source: Personal file.

Figure 95 – Rate of convergence for different analysis models using test data



Source: Personal file.

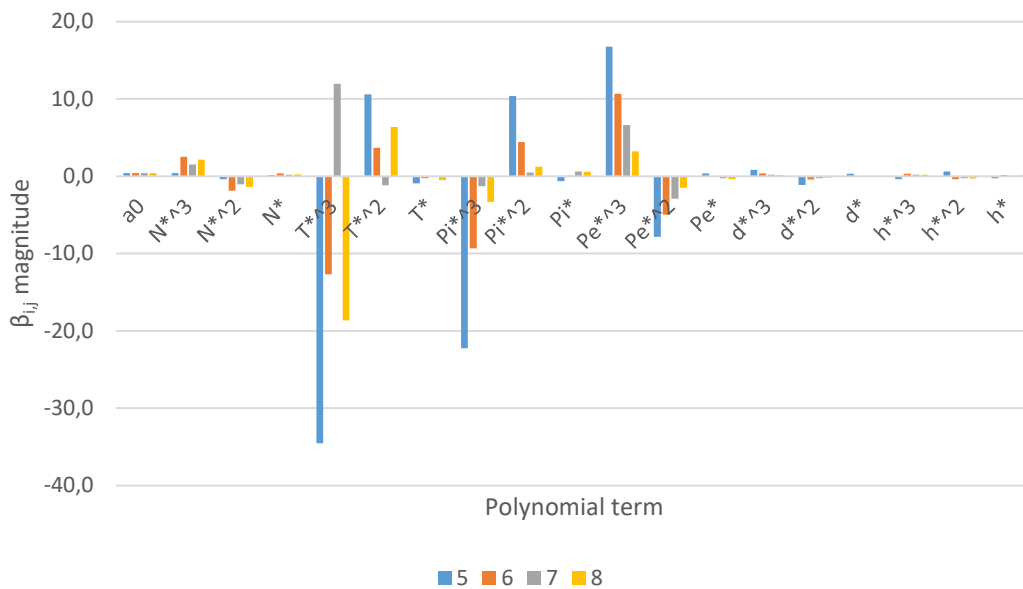
Figure 96 – Metamodel complexity for different analysis models and iteration cycles



Source: Personal file.

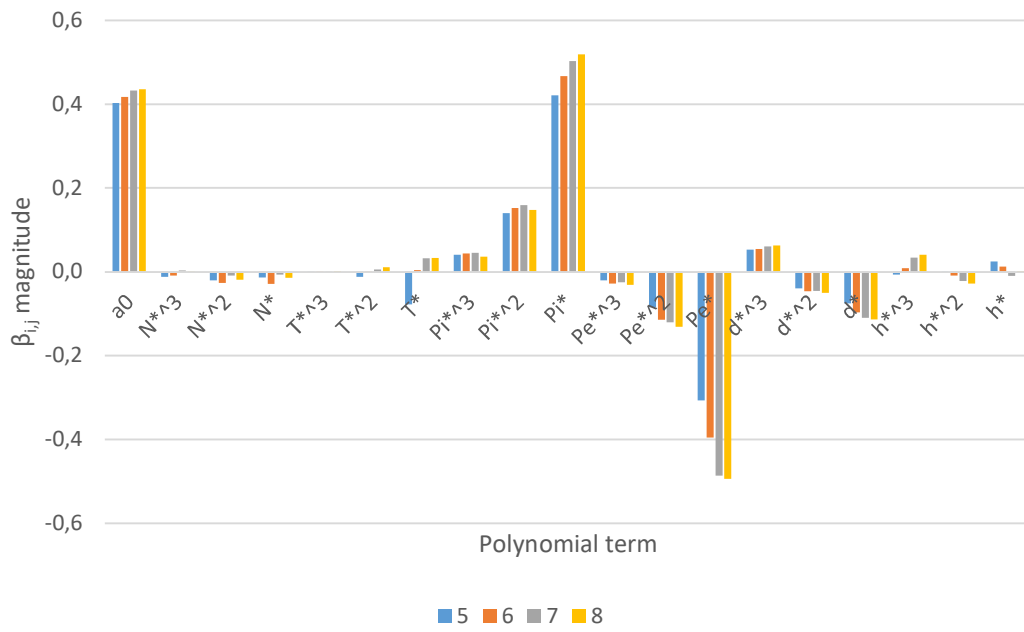
The magnitude of the metamodel parameters found by ordinary linear regression (Figure 97), Ridge (Figure 98), Lasso (Figure 99) and ElasticNet (Figure 100) are compared for different iteration cycles n .

Figure 97 Metamodel parameters convergence using OLR for different iteration cycles



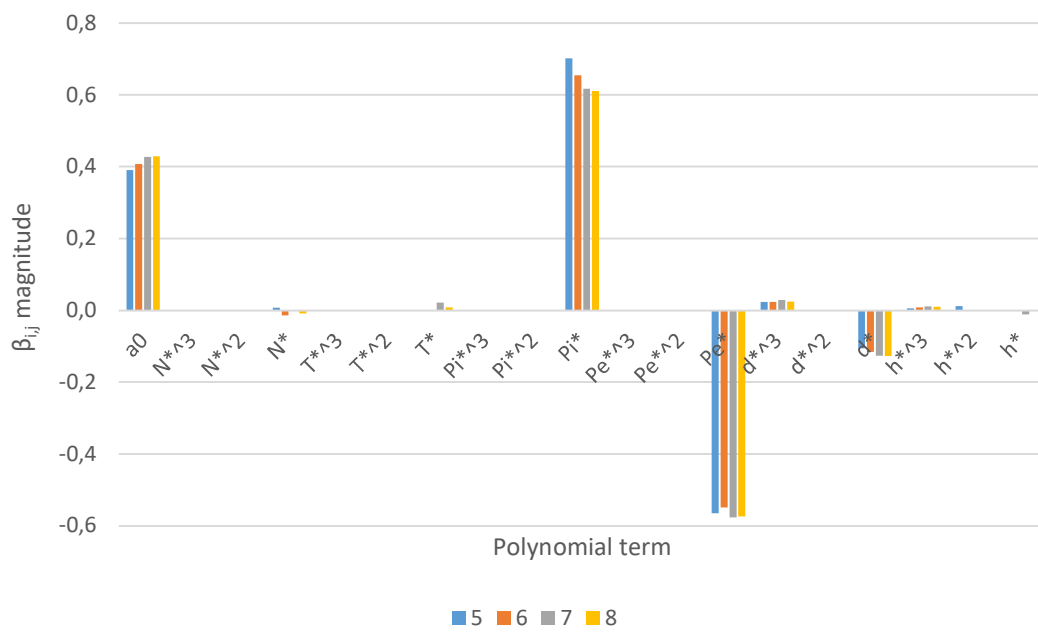
Source: Personal file.

Figure 98 –Metamodel parameters convergence using Ridge for different iteration cycles



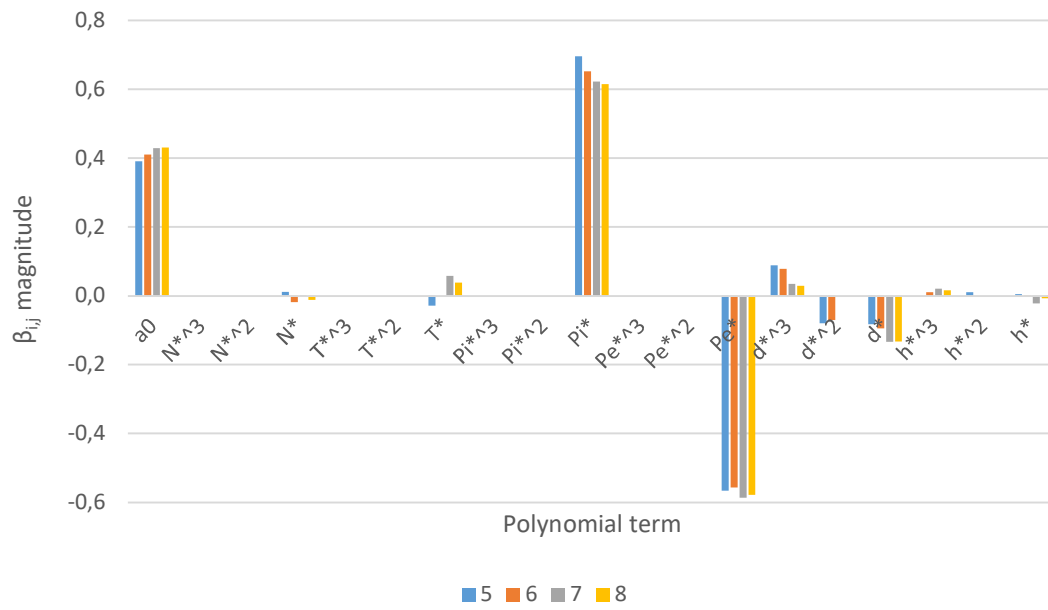
Source: Personal file.

Figure 99 –Metamodel parameters convergence using Lasso for different iteration cycles



Source: Personal file.

Figure 100 –Metamodel parameters convergence using ElasticNet for different iteration cycles



Source: Personal file.

Results show that data analysis using ElasticNet provided the best balance between model fitting, generalization, complexity and convergence. For the maximum data available ($N_{sim_{train}} = 132$), the obtained metamodel is,

$$F^* = 0.431 - 0.012N^* + 0.038T^* + 0.615P_i^* - 0.578P_e^* + 0.029d^{*3} - 0.133d^* + 0.016h^{*3} - 0.007h^* \quad (66)$$

A second analysis suppressing pressure was performed to ensure that such variable is not skewing the results. Using input points and the same tuning parameters for ElasticNet analysis model, similar parameters were obtained demonstrating the robustness of the proposed model.

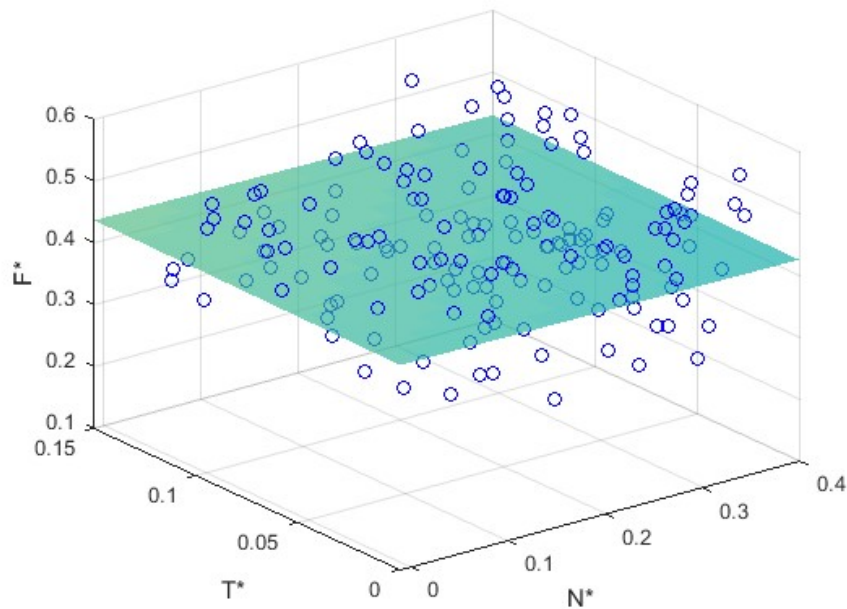
$$F^* = 0.423 - 0.011N^* + 0.017T^* + 0.028d^{*3} - 0.119d^* + 0.009h^{*3} - 0.008h^* \quad (67)$$

Once the coefficients for internal and external pressures on the tube are almost identical, it is supposed that the differential pressure on tube ΔP governs the force to cut it,

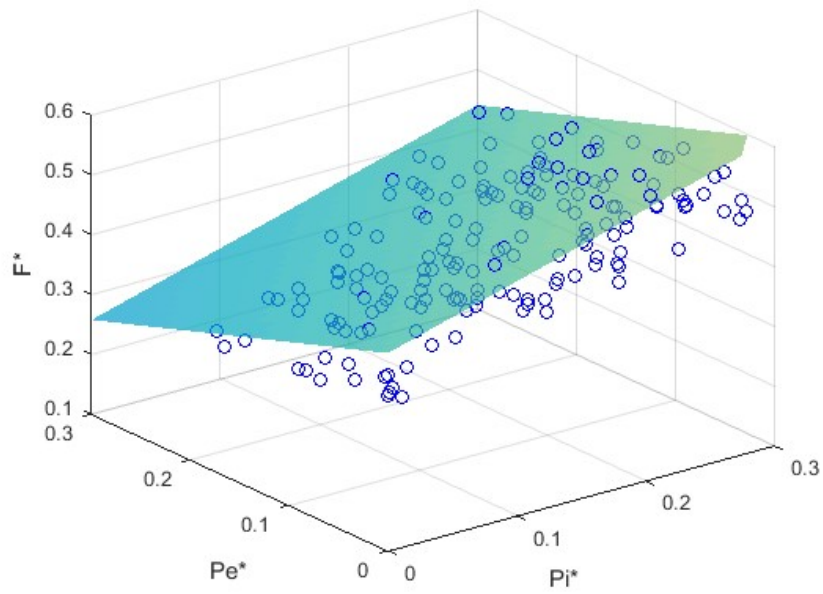
$$F^* = 0.431 - 0.012N^* + 0.038T^* + 0.600\Delta P^* + 0.029d^{*3} - 0.133d^* + 0.016h^{*3} - 0.007h^* \quad (68)$$

For a 6-dimensional domain model, it is not possible to establish visual resources for analysis of function values. However, in the attempt to illustrate the model output, a comparison of the response surface produced by the metamodel and FEM data sets is shown for F^* as a function of two input variables taking the variables pair by pair in Figure 101 (T^* and N^* on F^*), in Figure 102 (T^* and N^* on F^*) and in Figure 103 (Effect of h^* and d^* on F^*).

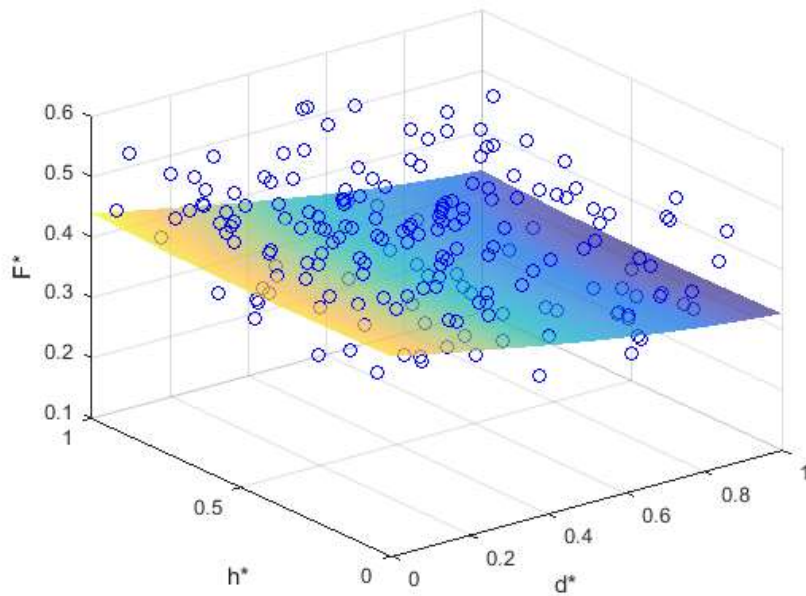
Figure 101 - Effect of T^* and N^* on F^*



Source: Personal file.

Figure 102 - Effect of P_e^* and P_i^* on F^* 

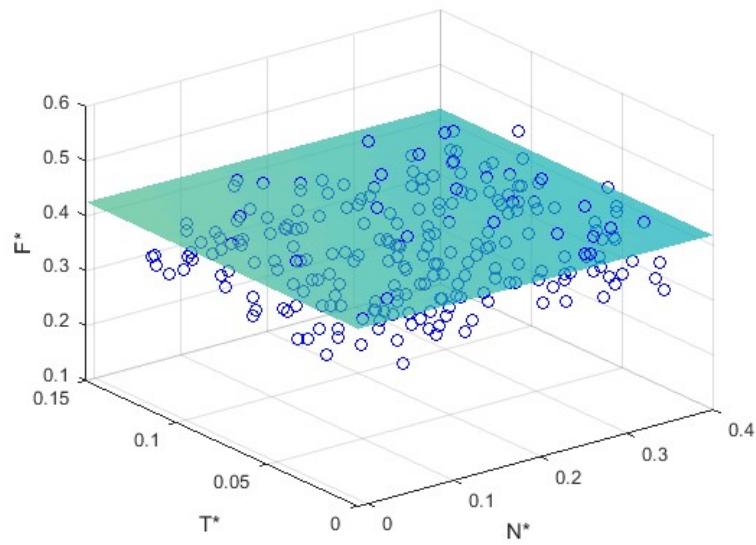
Source: Personal file.

Figure 103 - Effect of h^* and d^* on F^* 

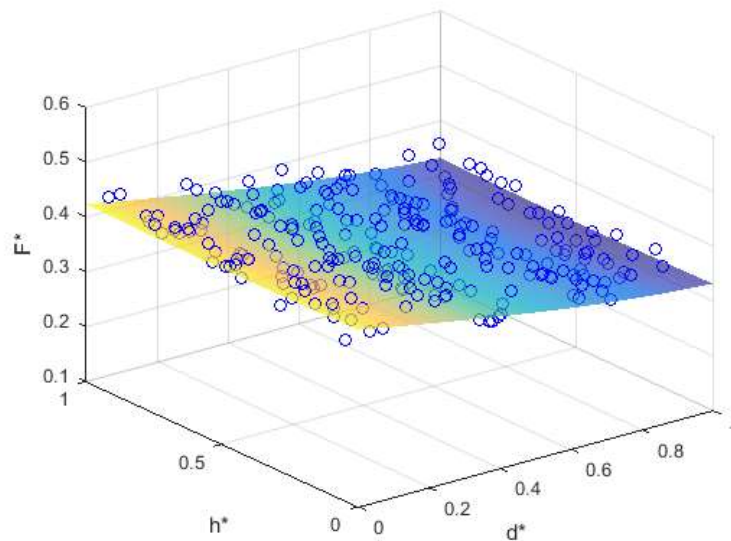
Source: Personal file.

Particularly, when the metamodel is tuned without the contribution of internal and external pressures on tube, it is more clear the effect of the other variables, as illustrated in Figure 104 (T^* and N^* on F^* with attenuated pressure dataset) and in Figure 105 (Effect of h^* and d^* on F^* with attenuated pressure dataset).

Figure 104 - Effect of T^* and N^* on F^* with attenuated pressure dataset



Source: Personal file.

Figure 105 - Effect of h^* and d^* on F^* with attenuated pressure dataset

Source: Personal file.

5.4.3. Results interpretation

The project variables influence on the required force to cut the pipe is measurable when sufficient data is enough to remove noise effects. For the studied set of boundary conditions, the required force to cut tends to increase with internal pressure. On the other side, it tends to decrease with external pressure and pipe offsetting. Torque and traction on tube and ram offsetting are found to have negligible effect on the force to cut the pipe for the considered range.

In the project variables domain, the maximum required force to cut the BOP plus internal frictions are found to be 5.5MN. Independently of the ram mechanical resistance, such force could not be reached in some BOP due to limitations of actuating force on rams. Table 25 shows the maximum force (F_{max}) that can be imposed by BOP as a function of actuating pressure (P_{act}), ram driving piston area (S_{ram}) and the BOP internal friction force (f),

$$F_{ram} = P_{act}S_{ram} - f \quad (69)$$

Table 25 - Maximum force delivered by BOP as a function of actuating pressure and driving piston size

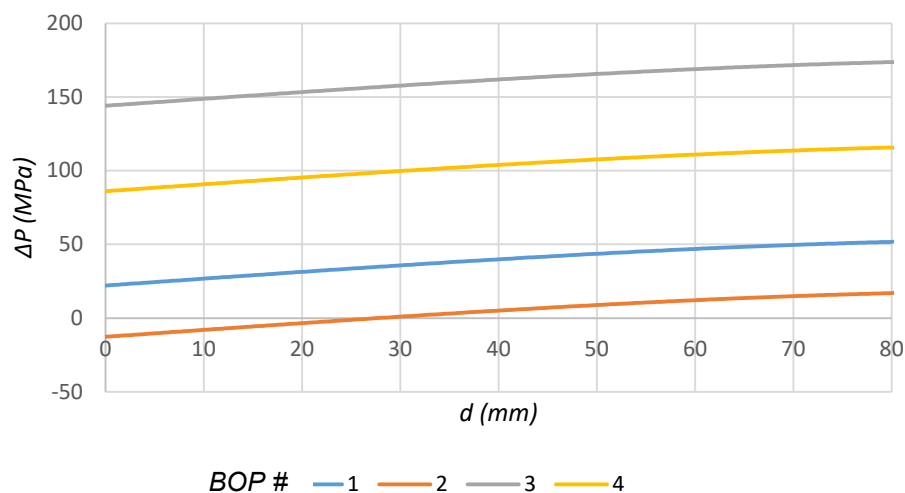
BOP #	Actuating pressure (psi)	Driving piston size	F_{ram} (MN)	F_{ram}^*
1	3000	22"	4.52	0.49
2	3000	14" + booster	3.56	0.39
3	5000	22"	7.90	0.86
4	5000	14" + booster	6.30	0.68

Source: Personal file.

Capability plots of BOP pipe cutting as a function of project variables are proposed by this thesis as a technological advance. Based on the obtained metamodel and restrictions on the project variables domain, the ultimate conditions for a given BOP to succeed in cutting a pipe can be derived. One example is illustrated in Figure 106 where the ultimate combination of differential pressure in the tube ΔP and pipe centralization from well center d are plotted for each BOP of Table 25,

$$F_{max}^* = 0.431 + 0.600\Delta P^* + 0.029d^{*3} - 0.133d^* \quad (70)$$

Figure 106 – Capability plot for pipe cutting as a function of ΔP and d in different BOPs



Source: Personal file.

6. Conclusions

The objective of the present work was successfully reached providing a technological gain to oil offshore industry. API S-135 steel was modeled, calibrated and validated using J-C plasticity and failure material models combined with Hillerborg damage model. Notched and unnotched cylinder specimens (“dog bone” type) for tensile testing were manufactured from a 5.5” 19.0 ppf drill pipe and used to calibrate the model parameters. Extra notched and unnotched beams were used in 3-point-bending tests to validate the model. Numerical FEM results were adherent to experimental testing including DIC measurements and fracture surface observed in SEM was coherent to calculated triaxiality.

With calibrated material model, the pipe cut in BOP was successfully modeled and simulated. The model geometries were extracted from literature and field measurements, considering both indenters (rams) with “V” shape. Numerical simulations presented adherent results to field measurements for the forces in rams during cut process, geometries of the cut pipes and ultimate force to cut a wide range of pipes. Differences of numerical and experimental results were attributed to BOP internal frictions and boundary conditions, which normally are not controlled in commissioning testing. Observed fracture surface in SEM images also agreed with the stress analysis of pipe during cut: dimples were found at the inner part of the tube where regions of high triaxiality were predicted by numerical model suggesting failure by tear process, i.e., Mode I dominated due to bending. On the other side, both numerical and experimental SEM measurement showed that most of the cut cross section have null triaxialities and Lode angles, in accordance with DTE analytical model for thin thickness tubes. Variations found in experimental pipe cut forces are attributed to uncontrolled boundary conditions changes.

Due to impracticality of an experimental study, a metamodel for predicting required force to cut a 6.63” 40.87ppf pipe in BOP under different boundary conditions was settled. At first, the tube was modeled with shell elements as a strategy to make feasible simulating a large number of pipes cutting in parallel for a metamodel construction. A set of designed simulations were proposed based

on LHS having a limited, progressive and unique input variable domain filling. Pipe tension, torque, internal pressure, external pressure and displacement as well as ram offset are input variables, having its limits established based on real operation values, while ultimate force on rams to cut the pipe is the output of simulation. Those parameters were normalized using their equivalent rupture values and results for the computational experiments were analyzed through machine learning concepts. To assure results reliability, a mesh convergence for the simplified model was performed and numerical stability by means of energy balance was checked for each simulation.

Metamodel parameters were found by convergence analysis as the number of simulations increased due to progressive domain discretization. It was proposed a polynomial sum of order 3 with independent terms to represent the ultimate cut force as a function of the project variables. The metamodel terms are determined by different regression models with regularization: ordinary linear regression, Ridge, Lasso and ElasticNet. A comparison among them demonstrated that ElasticNet provided the best balance between model accuracy, generalization and complexity and was used to build the metamodel. Its robustness was proved with a second set of data with suppressed pressure to guarantee its parameters were not skewed. A visual comparison of results predicted by FEM simulations and metamodel showed good adherence.

Finally, the metamodel provides means to understand the effect of combined project variables in structural failure and the method proposed herein can be expanded to similar problems. For the pipe cut in BOP analysis, it was found that external traction and torque on pipe and ram offset have negligible effect on the ultimate force to cut the pipe. On the other side, increase in internal over external pressures increases the required force to cut the pipe by aiding the tubular to maintain its original shape preventing its deformation. It was found that the increase in pipe misalignment relative to BOP bore center also tends to help cutting process by concentrating forces. The effect of the project variables in required force to cut an API S-135 6 5/8" 40.87ppf pipe in "V" shaped ram BOP is summarized in Table 26, where a single arrow represents a weak contribution and three arrows a strong contribution.

Table 26 - Summary of project variables effect in pipe cut

	Symbol	Upper limit	Lower limit	Effect on force to cut pipe on BOP	
Project variable	<i>N</i>	3.5MN	-0.05 MN	Slight decrease	↓
	<i>T</i>	54.2kNm	0kNm	Slight increase	↑
	<i>P_t</i>	65MPa	0kPa	Increase	↑↑↑
	<i>P_e</i>	65MPa	0kPa	Decrease	↓↓↓
	<i>h</i>	2.0mm	0.1mm	Slight increase	↑
	<i>d</i>	84.0mm	0.0mm	Decrease	↓↓↓

Source: Personal file.

The metamodel also aware that under certain boundary conditions, some BOP may not be able to cut the required pipe as indicated in capability plots. It must be highlighted that such conclusions must be limited to the materials, geometries and project variables ranges considered herein.

7. Further Works

It is suggested a deeper characterization of API S-135 steel, including testing plane specimens to cover a wider range of stress states and temperature effects, similar to real well conditions [2]. Due to COVID-19 outbreak it was not possible to perform those tests and characterization was performed in high triaxiality region.

Also, this thesis demonstrated the potentiality of using metamodels to predict structural failure with simplicity and efficiency, having a technological application to the oil industry. Indeed, it is possible to apply the proposed method to other materials and structures.

References

- [1] S. M. Zamania, S. A. Hassanzadeh-Tabrizi and H. Sharific, "Failure analysis of drill pipe: A review," *Engineering Failure Analysis*, pp. 605-623, 2016.
- [2] R. D. Grace, *Blowout and Well Control Handbook*, Burlington: Gulf Professional Publishing, 2003.
- [3] C. Han, "Study of the damage and failure of the shear ram of the blowout preventer in the shearing process," *Engineering Failure Analysis*, vol. 1, pp. 83-95, 2015.
- [4] Aoghs.org Editors, "Offshore Petroleum History," *American Oil & Gas Historical Society*, June 2020.
- [5] J. G. Speight, *Handbook of Offshore Oil and Gas Operations*, Houston: Gulf Professional Publishing, 2011.
- [6] W. Bascom, "The Mohole," *Scientific American*, vol. 200, pp. 41-49, April 1959.
- [7] J. A. Pratt, T. Priest and C. J. Castaneda, *Offshore pioneers: Brown & Root and the history of offshore oil and gas*, Houston: Gulf Publishing Group, 1997.
- [8] Equinor, "What is a blowout preventer?," Equinor, [Online]. Available: www.equinor.com. [Accessed 30 September 2020].
- [9] N. Lukin, *Gestão do risco de falha do preventor anular de BOP multiplexado submarino*, São Paulo: Master Thesis, University of São Paulo, 2016.
- [10] Transocean, *Macondo well incident, Transocean Investigation Report*, vol. I, 2011.
- [11] C. D. Johnson, C. T. Le, G. W. Tisdale and E. Palomo Jr., "Shear ram assembly". United States Patent US 6719042B2, 2014.
- [12] A. Telkin, *Blind shear ram blowout preventers: estimation of shear force and optimization of ram geometry*, Houston: Master Thesis, The Ohio State University, 2010.
- [13] F. Springett, "Low force shear rams: the future is more," *Society of Petroleum Engineers*, 2011.
- [14] C. Hall and T. Cole, "Study tackles industry's shearing capabilities," *The Offshore Frontier*, vol. 1, 2013.

- [15] R. Jones, *Deformation Theory of Plasticity*, ISBN 978-0-9787223-1-9: Bull Ridge Publishing, 2009.
- [16] A. Lima, *Desenvolvimento de um velo urbano seguro utilizando otimização baseada em metamodelos*, São Paulo: PhD thesis, University of São Paulo, 2016.
- [17] R. Rhinehart, *Nonlinear Regression Modeling for Engineering Applications: modeling, model, validation and enabling design of experiments*, West Sussex: Wiley, 2016.
- [18] L. Zhu, J. Kong, Q. Liu, H. Yang and B. Wang, "A numerical study on the ultimate strength of damaged tubular bracing members under axial compression," *ASME 2018 37th International Conference on Ocean, Offshore and Arctic Engineering*, 2018.
- [19] J. D. R. Jr. and P. Hodge, "Crushing of a Tube Between Rigid Plates," *Journal of Applied Mechanics*, vol. 3, pp. 391-395, 1963.
- [20] S. G. Thomas, S. R. Reid and W. Johnson, "Large deformations of thin-walled circular tubes under transverse loading," *International Journal of Mechanical Sciences*, vol. 18, pp. 325-333, 1976.
- [21] S. O. L. and L. G., "Collapse of tubular beams loaded by a wedge-shaped indenter," *Experimental Mechanics*, vol. 36, no. 4, pp. 374-378, 1996.
- [22] T. Wierzbicki and M. S. Suh, "Indentation of tubes under combined loading," *International Journal of Mechanical Sciences*, Vols. 3-4, pp. 229-248, 1988.
- [23] M. Moussouros, "Static Rigid-Plastic Analysis of Unstiffened Cylindrical Shells. Part 2. A New Model for the Cylinder," *NAVSWC TR*, pp. 90-454, 1990.
- [24] M. A. Polanco-Loria, H. Ilstad and E. Levold, "A numerical-experimental approach of indentation problem part i: force-dent response of steel pipes," *Conference: ASME 2017 36th International Conference on Ocean, Offshore and Arctic Engineering*, 2017.
- [25] C. Ruggieri and J. A. Ferrari, "Experimental and numerical study of damaged tubular members under lateral loads," in *Proceedings of OMAE'02 21st International Conference on Offshore Mechanics and Arctic Engineering*, Oslo, Norway, 2002.
- [26] G. Childs, J. Sattler and R. Williamson, "Evaluation of Sheer Ram Capabilities for U.S. Minerals Management Service, Requisition No. 2-1011-1003," 2004. [Online]. Available: <https://www.bsee.gov/research-record/tap-463-evaluation-sheer-ram-capabilities>. [Accessed 3 agosto 2020].

- [27] CBS , "Investigation report executive summary: drilling rig explosion and fire at the Macondo well," U.S. Chemical Safety And Hazard Investigation Board), 4 December 2016. [Online]. Available: <http://www.csb.gov/macondo-blowout-and-explosion/>.
- [28] E. Koustelos, Numerical analysis of a shear ram and experimental determination of fracture parameters, Massachusetts: Massachusetts Institute of Technology, 2012.
- [29] Y. Bai and T. Wierzbicki, "Application of extended Mohr-Coulomb criterion to ductile fracture," *International Journal of Fracture*, vol. 1, pp. 1-20, 2009.
- [30] Z. G. Liu, "Force Prediction in blow-out preventer shearing of drill pipes," *Engineering Failure Analysis*, pp. 159-171, 2017.
- [31] A. B. McCleney, S. T. Green and N. J. Mueschke, "Modeling of Subsea BOP Shear and Sealing Ability Under Flowing Conditions," *Offshore Technology Conference*, p. Offshore Technology Conference, May 2018.
- [32] F. V. Castilho, Estudo do processo de corte de tubos em BOP submarino em poços de petróleo, Rio de Janeiro: CEFET-RJ, 2016.
- [33] B. R. Tulimilli, P. Naik, A. Chakraborty, S. Sawant and A. Whooley, "Design study of BOP shear rams based on validated simulation model and sensitivity studies," *Proceedings of the ASME 2014 33rd International Conference on Ocean, Offshore and Arctic Engineering*, p. 24305, June 2014.
- [34] B. R. Tulimilli, P. Naik, A. Chakraborty, S. Sawant, A. Whooley and R. Weiss, "Experimental and numerical investigation of BOP shear ram performance," *Proceedings of the ASME 2014 33rd International Conference on Ocean, Offshore and Arctic Engineering*, p. 24714, June 2014.
- [35] L. L. D. Morales, Estudo experimental e numérico do comportamento mecânico na fratura da liga AISI 4340, Brasilia: Tese de Doutorado, Universidade de Brasília, 2020.
- [36] K.-J. Bathe, Finite Element Procedures, Massachusetts: Prentice Hall, 2006.
- [37] Y. Bai and T. Wierzbicki, "A new model of metal plasticity and fracture with pressure and Lode dependence," *International Journal of Plasticity*, vol. 6, no. 24, p. 1071–1096, 2008.
- [38] I. Barsoum and J. Faleskog, "Micromechanical analysis on the influence of the Lode parameter on void growth and coalescence," *International Journal of Solids and Structures*, vol. 48, no. 6, pp. 925-938, 15 March 2011.

- [39] K. Danas and P. Ponte Castañeda, "Influence of the Lode parameter and the stress triaxiality on the failure of elasto-plastic porous materials," *International Journal of Solids and Structures*, vol. 49, pp. 1325-1342, June 2012.
- [40] L. Xue, Ductile Fracture Modeling - Theory, Experimental Investigation and Numerical Verification, Massachusetts: Doctorate Thesis, Massachusetts Institute of Technology, 2007.
- [41] M. Brünig, O. Chyra, D. D. L. Albrecht and M. Alves, "A ductile damage criterion at various stress triaxialities," *International Journal of Plasticity*, vol. 24, pp. 1731-1755, 2008.
- [42] L. Driemeier, M. Brünig, G. Micheli and M. Alves, "Experiments on stress-triaxiality dependence of material behavior of aluminum alloys," *Mechanics of Materials*, vol. 42, pp. 207-217, 2010.
- [43] R. Kiran and K. Khandelwal, "A triaxiality and Lode parameter dependent ductile fracture criterion," *Engineering Fracture Mechanics*, vol. 128, pp. 121-138, August 2014.
- [44] X. Xiao, Y. Wang, V. V. Vershinin, L. Chen and Y. Lou, "Effect of Lode angle in predicting the ballistic resistance of Weldox 700 E steel plates struck by blunt projectiles," *International Journal of Impact Engineering*, vol. 128, pp. 46-71, June 2019.
- [45] T. Wierzbicki, Y. Bao, Y.-W. Lee and Y. Bai, "Calibration and evaluation of seven fracture models," *International Journal of Mechanical Sciences*, vol. 47, no. 4-5, pp. 719-743, April-May 2005.
- [46] S. Gerke, P. Adulyasak and M. Brünig, "New biaxially loaded specimens for analysis of damage and fracture in sheet metals," *International Journal of Solids and Structures*, Vols. 110-111, pp. 209-218, 2017.
- [47] M. Brünig, S. Gerke and J. Tix, "Micro-mechanical numerical analysis on the effect of stress state on ductile damage under dynamic loading conditions," *Latin American Journal of Solids and Structures*, vol. 15, p. Epub, 2018.
- [48] M. Brünig, S. Gerke and M. Schmidt, "Biaxial Experiments and Numerical Simulations on Damage and Fracture Mechanisms in Ductile Metals at Different Loading Conditions," *Procedia Structural Integrity*, vol. 2, pp. 3109-3116, 2016.
- [49] M. Brünig, S. Gerke and M. Schmidt, "Biaxial experiments and phenomenological modeling of stress-state-dependent ductile damage and fracture," *International Journal of Fracture*, vol. 200, p. pages63–76, 2016.

- [50] M. Brünig, S. Gerke and M. Schmidt, "Damage and failure at negative stress triaxialities: Experiments, modeling and numerical simulations," *International Journal of Plasticity*, vol. 102, pp. 70-82, March 2018.
- [51] W. K. Rule and S. E. Jones, "A revised form for the Johnson-Cook strength model," *International Journal of Impact Engineering*, vol. 21, no. 8, pp. 609-624, 1998.
- [52] G. R. Johnson and W. H. Cook, "A constitutive model and data for metals subjected to large strains, high strain rates and high temperatures," *Proceedings of the 7th International Symposium on Ballistics*, 1983.
- [53] G. R. Johnson and W. H. Cook, "Fracture characteristics of three metals subjected to various strains, strain rates, temperatures and pressures," *Engineering Fracture Mechanics*, p. 31-48, 1985.
- [54] F. A. McClintock, "A criterion of ductile fracture by the growth of holes," *Journal of Applied Mechanics*, vol. 2, p. 363-371, 1968.
- [55] A. L. Gurson, "Continuum Theory of Ductile Rupture by Void Nucleation and Growth: Part I - Yield Criteria and Flow Rules for Porous Ductile Media," *Journal of Engineering Materials and Technology*, vol. 99, p. 2-15, 1977.
- [56] J. Rice and D. Tracey, "On the ductile enlargement of voids in triaxial stress fields," *Journal of the Mechanics and Physics of Solids*, vol. 17, p. 201-217, 1969.
- [57] V. Tvergaard, "Influence of voids on shear band instabilities under plain strain conditions," *International Journal of Fracture*, p. 389-407, 1981.
- [58] A. A. Benzerga, J.-B. Leblond, A. Needleman and V. Tvergaard, "Ductile failure modeling," *International Journal of Fracture*, pp. 1-52, July 2016.
- [59] P. J. Noell, J. D. Carroll and B. L. Boyce, "The mechanisms of ductile rupture," *Acta Materialia*, vol. 161, p. 83-98, 2018.
- [60] L. Driemeier, *Estudo de falhas em materiais dúcteis: uma abordagem numérica (Tese de Livre Docência)*, São Paulo: Universidade de São Paulo, 2014.
- [61] R. Hill, "A theory of the yielding and plastic flow of anisotropic metals," *Proceedings Mathematical Physical & Engineering Sciences*, no. 193, p. 281-297, 1948.
- [62] J. W. Hancock and A. C. Mackenzie, "On the mechanisms of ductile failure in high-strength steels subjected to multi-axial stress-states," *Journal of the Mechanics and Physics of Solids*, vol. 24, pp. 147-160, 1976.

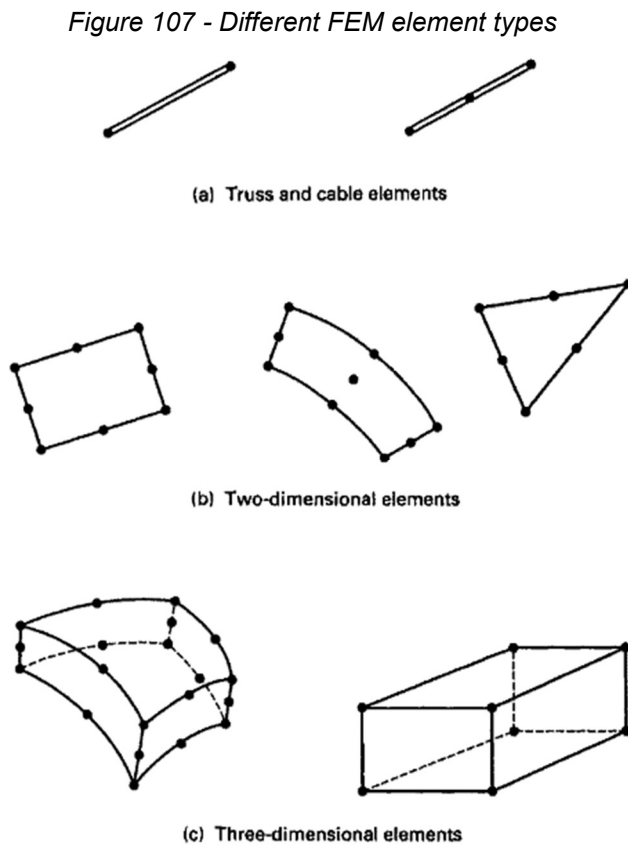
- [63] A. Weck and D. Wilkinson, "Experimental investigation of void coalescence in metallic sheets containing laser drilled holes," *Acta Materialia*, vol. 56, p. 1774–1784, March 2008.
- [64] L. Malcher, F. M. A. Pires and J. M. A. C. d. Sá, "An assessment of isotropic constitutive models for ductile fracture under high and low stress triaxiality," *International Journal of Plasticity*, pp. 81-115, March 2012.
- [65] Y. Bao and T. Wierzbicki, "On fracture locus in the equivalent strain and stress triaxiality space," *International Journal of Mechanical Sciences*, vol. 46, p. 81–98, 2004.
- [66] K. Nahshon and J. Hutchinson, "Modification of the Gurson Model for shear failure," *European Journal of Mechanics A/Solids*, p. 1–17, 2008.
- [67] M. Dunand and D. Mohr, "On the predictive capabilities of the shear modified Gurson and the modified Mohr–Coulomb fracture models over a wide range of stress triaxialities and Lode angles," *Journal of the Mechanics and Physics of Solids*, vol. 59, pp. 1374-1394, July 2011.
- [68] L. Malcher, Da mecânica do dano contínuo: uma evolução do modelo de Lemaitre para redução da dependência do ponto de calibração (tese de doutorado), Brasília: UNB, 2011.
- [69] J. Lemaitre and J. Dufailly, "Damage measurements," *Engineering Fracture Mechanics*, vol. 28, pp. 643-661, 1987.
- [70] V. Tvergaard, "Material Failure by Void Growth to Coalescence," *Advances in Applied Mechanics*, vol. 27, pp. 83-151, 1989.
- [71] B. Wu, X. Li, Y. Di, V. Brinnel, J. Lian and S. Münstermann, "Extension of the modified Bai-Wierzbicki model for predicting ductile fracture under complex loading conditions," *Fatigue and Fracture of Engineering Materials and Structures*, pp. 2152-2168, 2017.
- [72] L. M. Kachanov, "Rupture time under creep conditions," *International Journal of Fracture*, pp. 26-31, 1958.
- [73] J. Lemaitre, A Course on Damage Mechanics, Berlin: Springer-Verlag, 1992.
- [74] J. Lemaitre and J.-L. Chaboche, Mechanics of solid materials, New York: Cambridge University Press, 1990.
- [75] Y. S. Sun, "Revised Miner's rule and its application in calculating equivalent loads for components," *Reability Engineering and System Safety*, vol. 43, pp. 319-324, 1994.

- [76] Dassault Systèmes Simulia Corp, Abaqus Analysis User's Manual, Providence: Dassault Systèmes Simulia Corp, 2009.
- [77] A. Hillerborg, M. Modéer and P.-E. Peterson, "Analysis of crack formation and crack growth in concrete by means of fracture mechanics and finite element," *Cement and concrete research*, vol. 6, pp. 773-782, 1976.
- [78] M. Brünig, "A ductile damage criterion at various," *International Journal of Plasticity*, p. 1731–1755, 2008.
- [79] L. W. Friedman, *The Simulation Metamodel*, Massachusetts: Kluwer, 1996.
- [80] J. S. Arora, *Introduction to Optimal Design*, London: Elsevier, 2017.
- [81] K. B. Petersen and M. S. Pedersen, *The Matrix Cookbook*, 2012.
- [82] T. Hastie, R. Tibshirani and M. Wainwright, *Statistical Learning with Sparsity: The Lasso and Generalizations*, Boca Raton: CRC Press, 2015.
- [83] A. C. Müller and S. Guido, *Introduction to Machine Learning with Python: A Guide for Data Scientists*, Sebastopol: O'Reilly Media, 2016.
- [84] J. S. Cramer, "Mean and variance of R² in small and moderate samples," no. 35, pp. 253-266, 1987.
- [85] J. P. Kleijnen and R. G. Sargent, "A methodology for fitting and validating metamodels in simulation," *European Journal of Operational Research*, vol. 120, pp. 14-29, 2000.
- [86] API, *Spec 5DP: Specification for Drill Pipe*, Washington DC: API (American Petroleum Institute), 2020.
- [87] H. Yan, Z. Xuehu, B. Zhenquan and Y. Chengxian, "Failure Analysis on Fracture of a S135 Drill Pipe," *Procedia Materials Science*, p. 447 – 453, 2014.
- [88] G. F. Miscow, P. E. V. d. Miranda, T. A. Netto, J. C. R. Plácido and J. H. B. S. Jr, "Real Scale Drill-pipe Steel Fatigue," *Conference: Simpósio Materia 2001, At Mexico*, no. DOI: 10.13140/2.1.2440.0160, 2001.
- [89] M. Paredes, J. Lian, T. Wierzbicki, M. E. Cristea, S. Münstermann and P. Darcis, "Modeling of plasticity and fracture behavior of X65 steels: seam weld and seamless pipes," *International Journal of Fracture*, pp. 17-36, january 2018.
- [90] S. Gerke, M. Zistl and M. Brünig, "Experiments with the X0-specimen under non-proportional loading paths". *Engineering Fracture Mechanics*, *Engineering Fracture Mechanics*, vol. 224, no. 1, p. 106795, 2020.

- [91] M. Brünig, S. Gerke and M. Zistl, "Experiments and numerical simulations with the H-specimen on damage and fracture of ductile metals under non-proportional loading paths," *Engineering Fracture Mechanics*, vol. 217, 2019.
- [92] API, API Technical Report 16TR1: BOP Shear Ram Performance Test Protocol, Washington, DC: (API) American Petroleum Institute, 2018.
- [93] RigManufacturing, "18-3/4" NOV CVX-W Type SLX 15M Shear RAM Assy P/N# 20026256-20 – New Surplus," Rig MFG, 2017. [Online]. Available: <http://www.rigmanufacturing.com/2017/04/21/18-34-nov-cvx-w-type-slx-15m-shear-ram-assy-pn-20026256-20-new-surplus/>. [Accessed 20 May 2019].
- [94] L. Weingarh, "Refining the DP Watch Circle," *Dynamic Positioning Conference*, pp. 1-13, 2006.
- [95] ASM, ASM Handbook volume 12: Fractography, USA: The Materials Information Company, 1992.
- [96] W. D. Nix and H. Gao, "Indentation size effects in crystalline materials: a law for strain gradient plasticity," *Journal of Mechanics and Physics of Solids*, vol. 46, no. 3, pp. 411-425, 1997.
- [97] K. Matsuda, "Prediction of stress-strain curves of elastic-plastic materials based on the Vickers indentation," vol. 82, no. 10, pp. 1941-1951, 2002.

Attachment A: FEM fundamentals

Finite Element Method (FEM) is a numerical method to analyze phenomena restrained by boundary conditions and governed by partial differential equations in continuous media. It is widely used in solid mechanics as it provides an approximate solution for stresses in complex structures. Basically, the continuous media geometry is discretized into nodes which are connected to form simple elements that are subdomains of the body. The group of elements is named mesh. Some elements geometries are shown in Figure 107. Each element type has its own formulation and is suitable for a specific application [36].



Source: Extracted from [36].

Although FEM leads to approximate solutions, it converges as long as the element size diminishes. Inside the elements domain, it is assumed that displacements are defined by interpolation functions and the differential problem is converted into a set of algebraic equations. Strains and stresses are obtained

from kinematic and constitutive laws. It is not the purpose of this thesis to describe in details FEM method, limiting its description to three main stages: pre-processing, processing and post-processing.

In pre-processing, the approximated geometry of the analyzed body is discretized into small finite elements. The material properties and the boundary and initial conditions (loads, displacements) are inputted to completely define the problem.

The method then calculates the displacements of the elements nodes U_i at global coordinates on the processing phase. According to the FEM formulation, the displacements must satisfy the Principal of Minimum Potential Energy. In the final algebraic form,

$$\mathbf{M}\ddot{\mathbf{U}}(t) + \mathbf{C}\dot{\mathbf{U}}(t) + \mathbf{K}\mathbf{U}(t) = \mathbf{F}(t) \quad (71)$$

where \mathbf{M} is the global mass matrix, \mathbf{C} is the global dumping matrix and \mathbf{K} is the global stiffness matrix of the structure that may be variable depending on the stress state of the system in a linear or nonlinear way and on time. The displacement, velocity and acceleration vectors of the structure nodes are $\mathbf{U}(t)$, $\dot{\mathbf{U}}(t)$ and $\ddot{\mathbf{U}}(t)$, while $\mathbf{F}(t)$ are the forces applied in respect to time.

The Principal of Minimum Potential Energy also can be used to validate the numerical solution for the structure. If the solution is numerically stable, the balance of energy is satisfied for the whole structure,

$$E_I + E_K - E_W = E_{Residue} \quad (72)$$

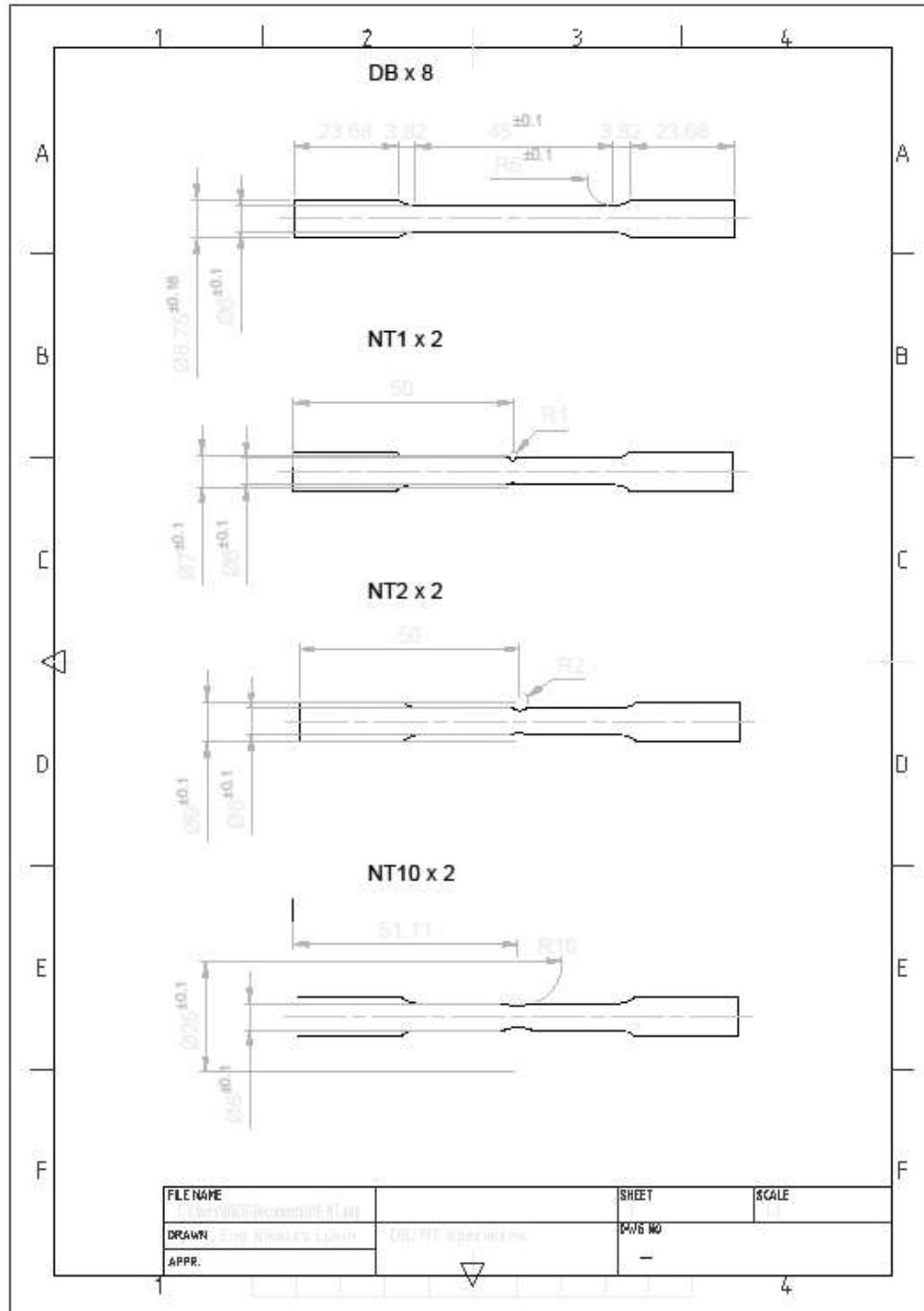
where E_I is the internal energy, E_K is the kinetic energy, E_W is the external work and $E_{Residue}$ is the system energy residue which should be negligible compared to the other terms. Energy balance can be verified for each simulation and when $E_{Residue} \approx 0$ it is stated that energy balance $BE = Y$, otherwise $BE = N$.

Finally, the results are presented in post-processing stage through a graphic-user interface (GUI). The amount of available information generated by a dynamic nonlinear analysis is enormous, including, for example, reactions, stress components, equivalent stresses, strains, strain energies, etc... The post processor is certainly a useful tool, since it allows the design engineer to analyze

details that would hardly be possible with analytical models or even experimental tests. In fact, the balance of the triad – analytical, experimental and numerical analyses – is important for the analysis, verification and validation of models.

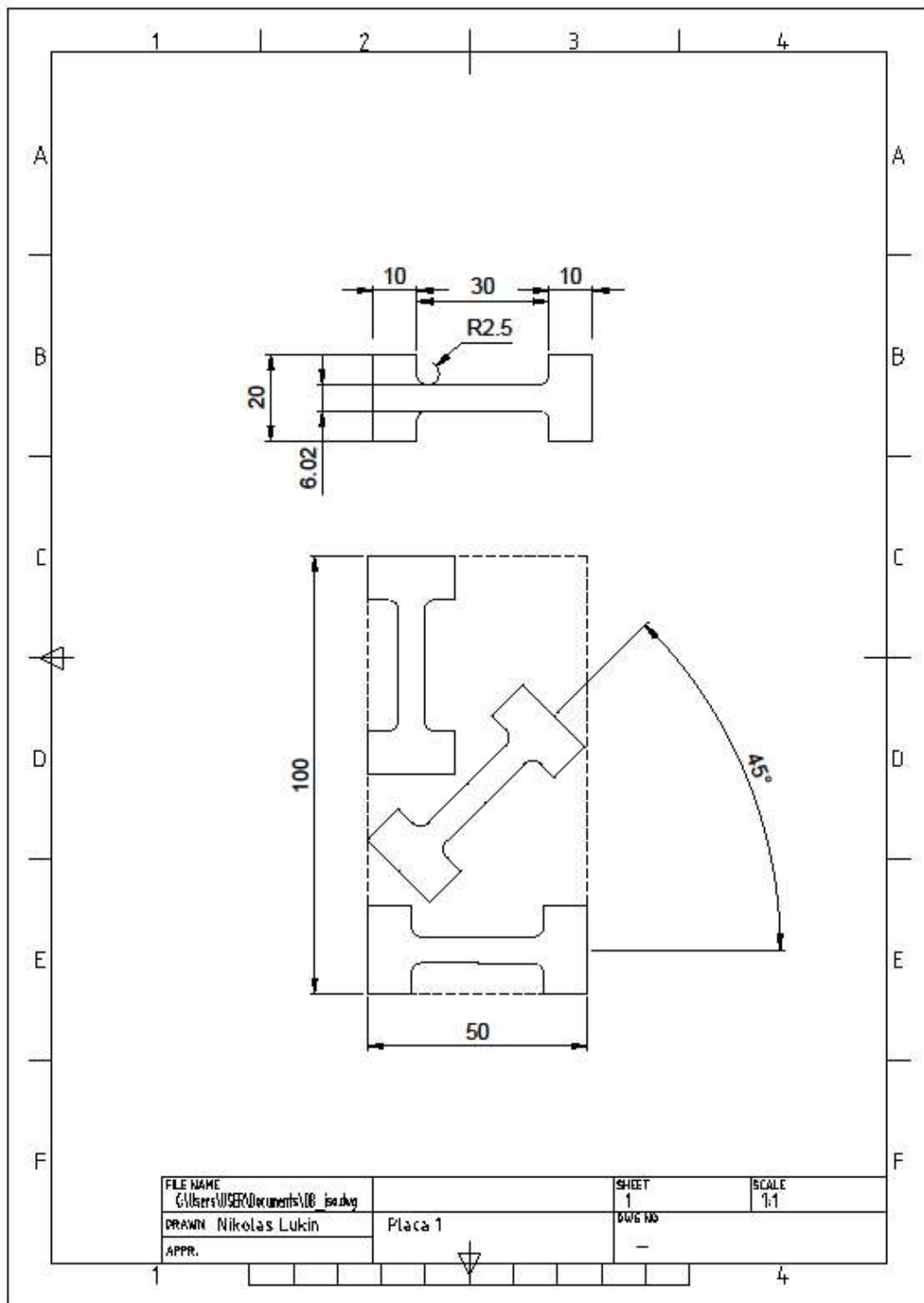
Attachment B: Design for manufacturing testing specimens

Figure 108 - Manufacturing project for DB specimens



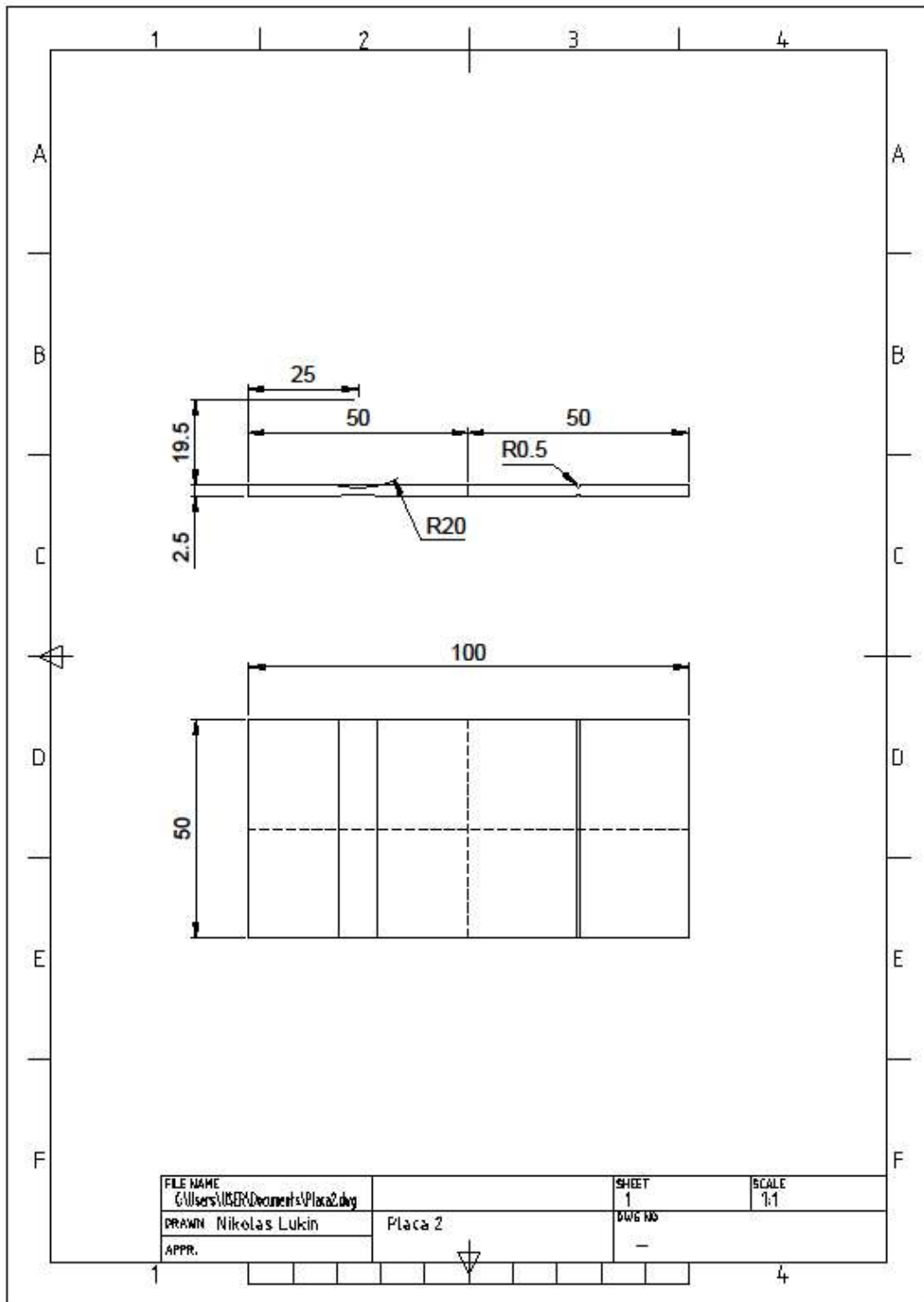
Source: Personal file.

Figure 109 - Manufacturing project for specimens of plate 1



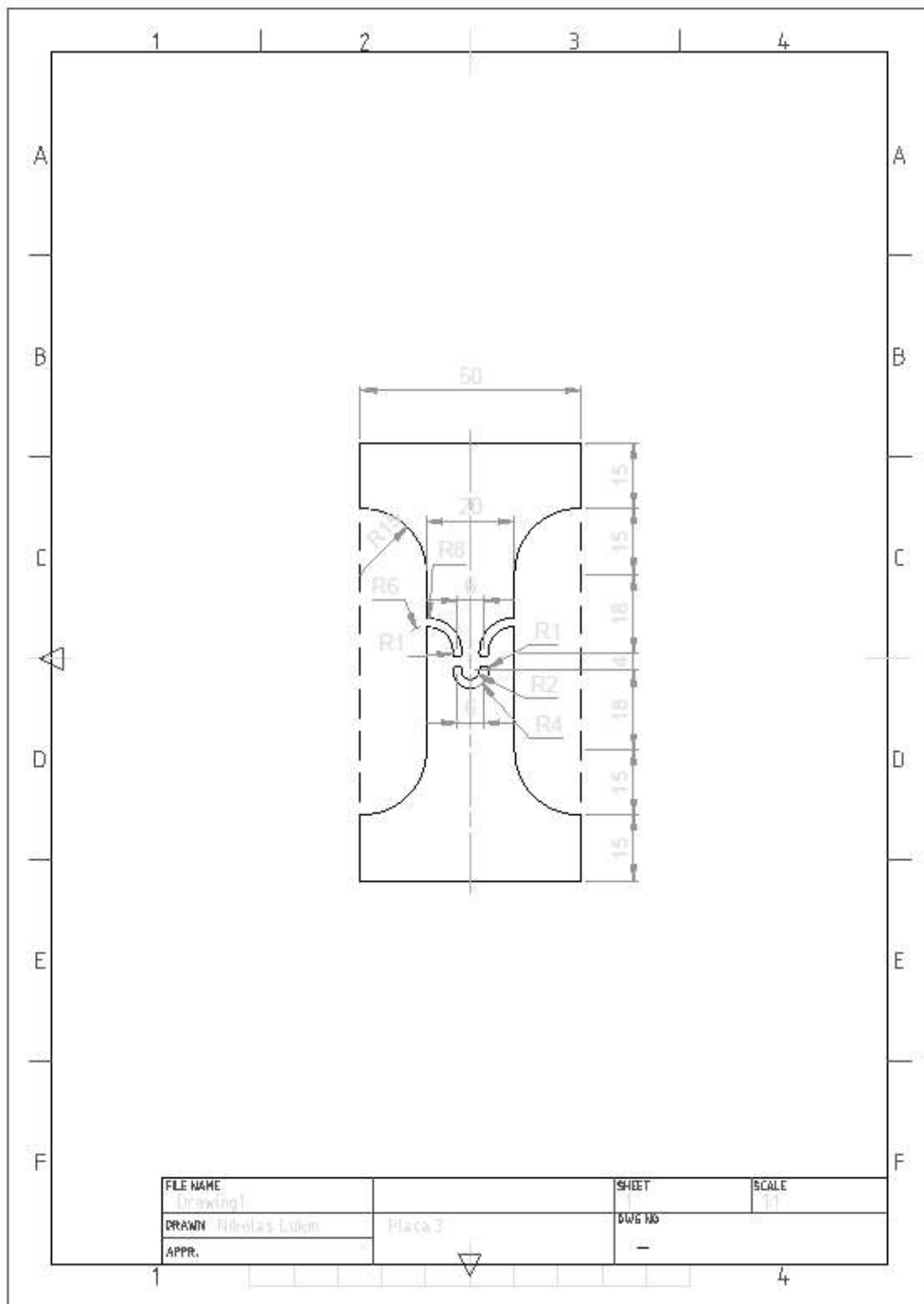
Source: Personal file.

Figure 110 - Manufacturing project for specimens of plate 2



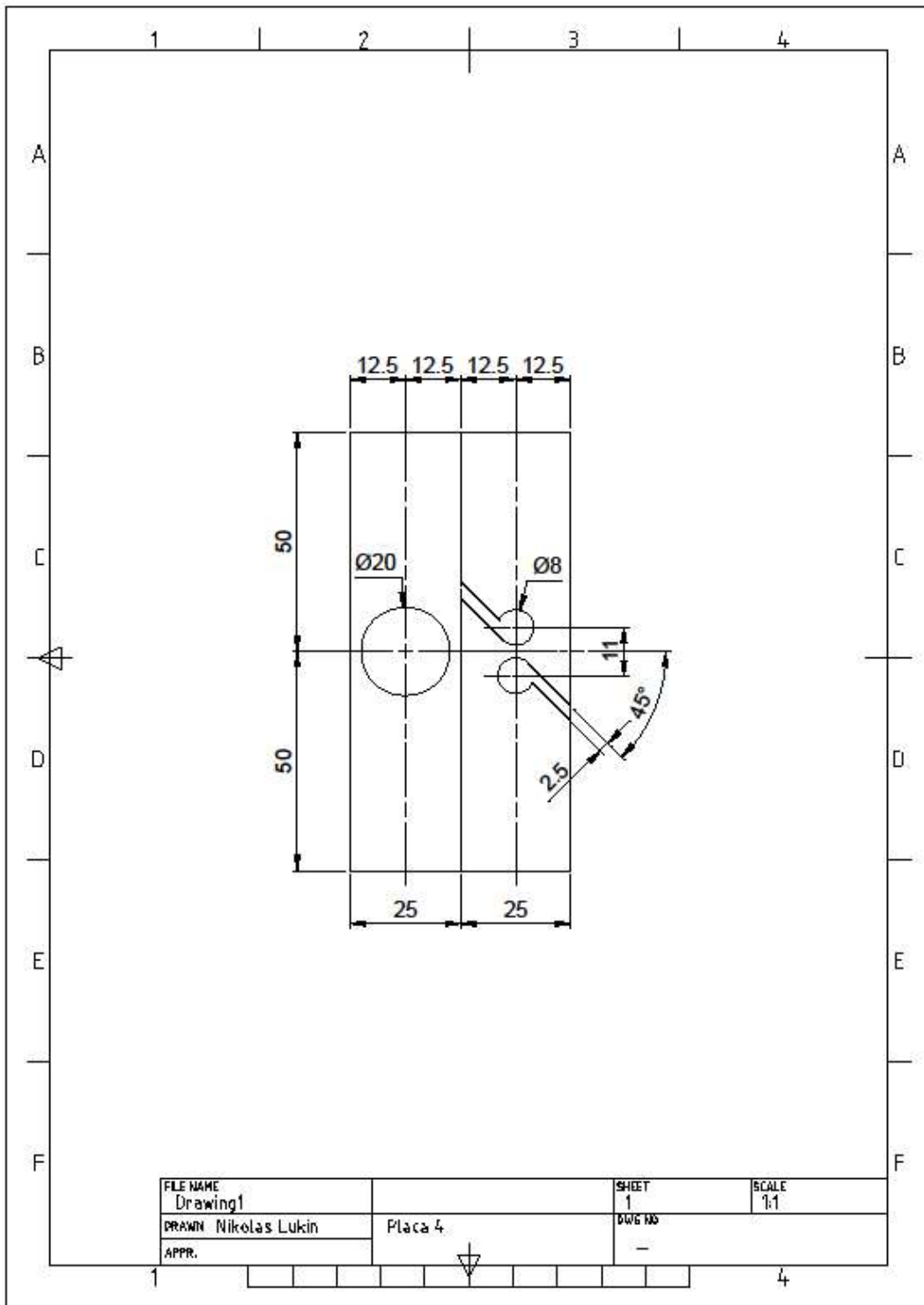
Source: Personal file.

Figure 111 - Manufacturing project for specimens of plate 3



Source: Personal file.

Figure 112 - Manufacturing project for specimens of plate 4

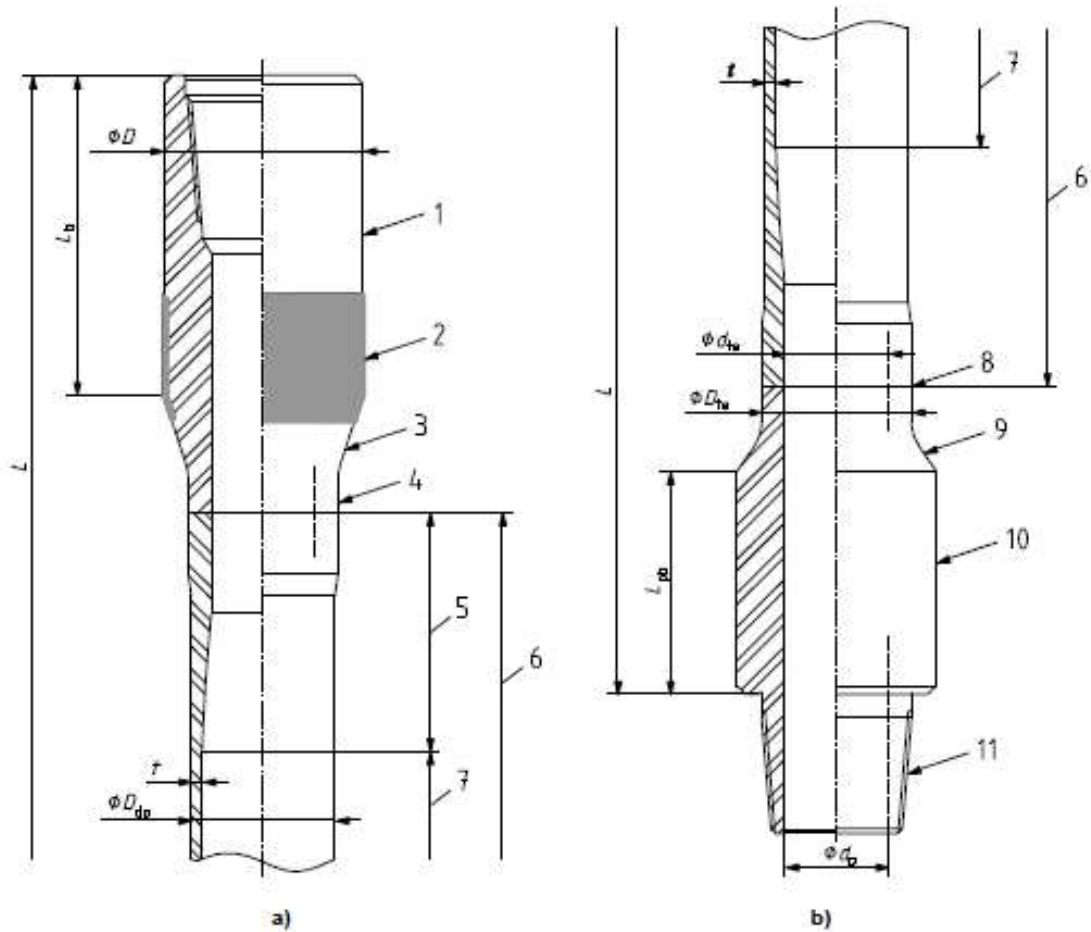


Source: Personal file.

Attachment C: API/ISO drill pipe geometrical properties

Drill pipe geometrical properties are normalized by API 5DP Spec [86]. Its main dimensions are presented in Figure 113 and Table 27.

Figure 113 – Drill pipe geometrical properties



Key

1	tool-joint box	7	pipe body
2	hard banding (optional)	8	friction weld
3	tapered elevator shoulder	9	pin taper
4	drill-pipe weld neck	10	tool-joint pin
5	drill-pipe-body upset	11	rotary shouldered connection.
6	drill-pipe-body		

Source: Extracted from [86].

Table 27 – Drill pipe geometrical properties

Designations ^a					Pipe body OD	Pipe wall thickness	Drill-pipe weld neck	Tool joint				RSC bevel dia.	Approx. mass ^c
Label 1	Label 2	Grade	Upset type	RSC type ^d				OD	Pin ID	Pin OD length	Box OD length		
					D_{op} mm	t mm	D_{te} ^b mm	D mm	d_p mm	L_{pb} mm	L_b mm	D_r mm	W_{op} kg/m
					See Table A.2	-12,5 %	max.	± 0,8	+0,4 -0,8	± 0,4	± 0,4	± 0,4	Calculated
1	2	3	4	5	6	7	8	9	10	11	12	13	14
Internal-external upset, IEU													
5-1/2	21.90	G	IEU	5 1/2 FH	139,70	9,17	144,5	184,2	88,9	203,20	254,00	170,66	37,61
5-1/2	21.90	S	IEU	5 1/2 FH	139,70	9,17	144,5	190,5	76,2	203,20	254,00	180,18	39,27
5-1/2	24.70	E	IEU	5 1/2 FH	139,70	10,54	144,5	177,8	101,6	203,20	254,00	170,66	39,19
5-1/2	24.70	X, G	IEU	5 1/2 FH	139,70	10,54	144,5	184,2	88,9	203,20	254,00	170,66	41,32
5-1/2	24.70	S	IEU	5 1/2 FH	139,70	10,54	144,5	190,5	76,2	203,20	254,00	180,18	42,97
6-5/8	25.20	E	IEU	6 5/8 FH	168,28	8,38	176,2	203,2	127,0	203,20	279,40	195,66	41,03
6-5/8	25.20	X	IEU	6 5/8 FH	168,28	8,38	176,2	203,2	127,0	203,20	279,40	195,66	41,03
6-5/8	25.20	G	IEU	6 5/8 FH	168,28	8,38	176,2	209,6	120,7	203,20	279,40	195,66	42,60
6-5/8	25.20	S	IEU	6 5/8 FH	168,28	8,38	176,2	215,9	108,0	203,20	279,40	195,66	44,73
6-5/8	27.70	E	IEU	6 5/8 FH	168,28	9,19	176,2	203,2	127,0	203,20	279,40	195,66	43,79
6-5/8	27.70	X, G	IEU	6 5/8 FH	168,28	9,19	176,2	209,6	120,7	203,20	279,40	195,66	45,35
6-5/8	27.70	S	IEU	6 5/8 FH	168,28	9,19	176,2	215,9	108,0	203,20	279,40	195,66	47,48
NOTE See Figure B.1.													
^a Designations are shown for the purpose of identification in ordering.													
^b D_{te} is held to a maximum to ensure fit with elevator.													
^c These values have been based on a drill-pipe-body length of 8,96 m and are provided for information only. For other lengths, see API RP 7G for the method of calculation.													
^d The RSC type indicates the size and style of the applicable rotary shouldered connection.													

Source: Extracted from [86].

Attachment D: Data of cut pipes in BOP

Data from open literature and provided by Petrobras of pipe cut in BOP with “V” shaped rams are summarized in Table 28.

Table 28 - Data of pipe cut in BOP from Petrobras and open literature

#	PPF	OD (in)	ID (in)	t (mm)	S_t (mm ²)	Operator	Ultimate pressure (psi)	Force to cut pipe (kN)	Year	Source
1	21,90	5,50	4,78	9,17	3760,1	14" + booster 14"	1564	2043,1	2011	Petrobras
2	24,20	5,88	5,15	9,17	4034,5	14" + booster 14"	1900	2482,0	2011	Petrobras
3	40,70	6,63	5,38	15,88	7600,6	14" + booster 14"	2414	3153,5	2012	Petrobras
4	40,50	6,63	5,38	15,88	7600,6	22"	1800	3043,5	2015	Petrobras
5	48,13	6,63	5,38	15,88	7600,6	22"	2290	3872,0	2011	Petrobras
6	40,87	6,63	5,38	15,88	7600,6	22"	2380	4024,2	2012	Petrobras
7	40,87	6,63	5,38	15,88	7600,6	22"	2570	4345,4	2012	Petrobras
8	40,87	6,63	5,38	15,88	7600,6	22"	2680	4531,4	2012	Petrobras
9	40,87	6,63	5,38	15,88	7600,6	22"	3100	5241,6	2012	Petrobras
10	40,70	6,63	5,38	15,88	7600,6	22"	2149	3633,6	2012	Petrobras
11	21,90	5,50	4,78	9,17	3760,1	22"	1500	2536,2	2010	Petrobras
12	21,90	5,50	4,78	9,17	3760,1	22"	1300	2198,1	2011	Petrobras
13	14,00	4,00	3,24	9,65	2788,1	13,5	2030	1179,0	2015	Han, 2015
14	13,30	3,50	2,76	9,35	2336,1			1245,4	2013	MCS Kenny, 2013
15	13,30	3,50	2,76	9,35	2336,1			1394,9	2013	MCS Kenny, 2013
16	19,50	5,00	4,28	9,19	3403,0		2500	1711,4		Childs et al, 2004
17	19,50	5,00	4,28	9,19	3403,0		2145	1468,4		Childs et al, 2004
18	19,50	5,00	4,28	9,19	3403,0		1850	1266,4		Childs et al, 2004
19	19,50	5,00	4,28	9,19	3403,0		3050	2087,9		Childs et al, 2004
20	19,50	5,00	4,28	9,19	3403,0		3025	2070,8		Childs et al, 2004
21	19,50	5,00	4,28	9,19	3403,0		2700	1848,3		Childs et al, 2004
22	19,50	5,00	4,28	9,19	3403,0		2900	1985,2		Childs et al, 2004
23	19,50	5,00	4,28	9,19	3403,0		2950	2019,4		Childs et al, 2004
24	19,50	5,00	4,28	9,19	3403,0		1127	1574,9	1992	Childs et al, 2004
25	19,50	5,00	4,28	9,19	3403,0		1189	1661,5	1992	Childs et al, 2004
26	19,50	5,00	4,28	9,19	3403,0		1212	1693,6	1992	Childs et al, 2004

27	19,50	5,00	4,28	9,19	3403,0		1445	1212,8	1992	Childs et al, 2004
28	19,50	5,00	4,28	9,19	3403,0		1425	1196,0	1992	Childs et al, 2004
29	19,50	5,00	4,28	9,19	3403,0		1434	1203,5	1992	Childs et al, 2004
30	19,50	5,00	4,28	9,19	3403,0		1460	1225,4	1992	Childs et al, 2004
31	19,50	5,00	4,28	9,19	3403,0		1440	1208,6	1992	Childs et al, 2004
32	19,50	5,00	4,28	9,19	3403,0		1459	1224,5	1992	Childs et al, 2004
33	19,50	5,00	4,28	9,19	3403,0		1404	1178,4	1992	Childs et al, 2004
34	19,50	5,00	4,28	9,19	3403,0		1410	1183,4	1992	Childs et al, 2004
35	19,50	5,00	4,28	9,19	3403,0		1430	1200,2	1992	Childs et al, 2004
36	19,50	5,00	4,28	9,19	3403,0		1406	1180,1	1992	Childs et al, 2004
37	19,50	5,00	4,28	9,19	3403,0		1367	1147,3	1992	Childs et al, 2004
38	19,50	5,00	4,28	9,19	3403,0		1402	1176,7	1992	Childs et al, 2004
39	20/18,7	4,50	3,64	10,92	3547,2		1725	1223,7	1983	Childs et al, 2004
40	20/18,7	4,50	3,64	10,92	3547,2		1800	1276,9	1983	Childs et al, 2004
41	20/18,7	4,50	3,64	10,92	3547,2		1910	1354,9	1983	Childs et al, 2004
42	20/18,7	4,50	3,64	10,92	3547,2		1890	1340,8	1983	Childs et al, 2004
43	20/18,7	4,50	3,64	10,92	3547,2		1860	1319,5	1983	Childs et al, 2004
44	20/18,7	4,50	3,64	10,92	3547,2		1725	1223,7	1983	Childs et al, 2004
45	20/18,7	4,50	3,64	10,92	3547,2		1800	1276,9	1983	Childs et al, 2004
46	20/18,7	4,50	3,64	10,92	3547,2		1910	1354,9	1983	Childs et al, 2004
47	20/18,7	4,50	3,64	10,92	3547,2		1900	1347,8	1983	Childs et al, 2004
48	20/18,7	4,50	3,64	10,92	3547,2		1890	1340,8	1983	Childs et al, 2004
49	20/18,7	4,50	3,64	10,92	3547,2		1860	1319,5	1983	Childs et al, 2004
50	21,90	5,50	4,78	9,17	3760,1		2150	1471,8		Childs et al, 2004
51	21,90	5,50	4,78	9,17	3760,1		2200	1506,0		Childs et al, 2004
52	21,90	5,50	4,78	9,17	3760,1		2080	1423,8		Childs et al, 2004
53	21,90	5,50	4,78	9,17	3760,1		2080	1423,8		Childs et al, 2004
54	21,90	5,50	4,78	9,17	3760,1		2101	1763,4	1992	Childs et al, 2004
55	21,90	5,50	4,78	9,17	3760,1		2122	1781,0	1992	Childs et al, 2004
56	21,90	5,50	4,78	9,17	3760,1		2431	2040,3	1992	Childs et al, 2004
57	21,90	5,50	4,78	9,17	3760,1		1960	1645,0	1992	Childs et al, 2004
58	21,90	5,50	4,78	9,17	3760,1		2438	2046,2	1992	Childs et al, 2004
59	21,90	5,50	4,78	9,17	3760,1		2712	2276,2	1992	Childs et al, 2004
60	21,90	5,50	4,78	9,17	3760,1		2647	2221,6	1992	Childs et al, 2004
61	21,90	5,50	4,78	9,17	3760,1		2068	1735,7	1992	Childs et al, 2004
62	21,90	5,50	4,78	9,17	3760,1		2196	1843,1	1992	Childs et al, 2004
63	21,90	5,50	4,78	9,17	3760,1		2361	1981,6	1992	Childs et al, 2004
64	21,90	5,50	4,78	9,17	3760,1		2025	1699,6	1992	Childs et al, 2004
65	21,90	5,50	4,78	9,17	3760,1		2587	2171,3	1992	Childs et al, 2004
66	25,20	6,63	5,97	8,38	4213,8		2850	1951,0		Childs et al, 2004
67	25,20	6,63	5,97	8,38	4213,8		2600	1779,8		Childs et al, 2004
68	25,20	6,63	5,97	8,38	4213,8		2700	1848,3		Childs et al, 2004

69	25,20	6,63	5,97	8,38	4213,8		2750	1882,5		Childs et al, 2004
70	25,20	6,63	5,97	8,38	4213,8		2625	1796,9		Childs et al, 2004
71	24,70	5,50	4,67	10,54	4277,2		1960	1341,7		Childs et al, 2004
72	24,70	5,50	4,67	10,54	4277,2		1970	1348,5		Childs et al, 2004
73	24,70	5,50	4,67	10,54	4277,2		2140	1464,9		Childs et al, 2004
74	24,70	5,50	4,67	10,54	4277,2		2250	1540,3		Childs et al, 2004
75	24,70	5,50	4,67	10,54	4277,2		2360	1615,5		Childs et al, 2004
76	24,70	5,50	4,67	10,54	4277,2		2150	1471,8		Childs et al, 2004
77	24,70	5,50	4,67	10,54	4277,2		1950	1334,9		Childs et al, 2004
78	24,70	5,50	4,67	10,54	4277,2		1850	1266,4		Childs et al, 2004
79	24,70	5,50	4,67	10,54	4277,2		2175	1488,9		Childs et al, 2004
80	24,70	5,50	4,67	10,54	4277,2		4220	2888,8		Childs et al, 2004
81	24,70	5,50	4,67	10,54	4277,2		2580	1766,1		Childs et al, 2004
82	24,70	5,50	4,67	10,54	4277,2		3700	2532,8		Childs et al, 2004
83	24,70	5,50	4,67	10,54	4277,2		3100	2122,1		Childs et al, 2004
84	24,70	5,50	4,67	10,54	4277,2		2675	1831,2		Childs et al, 2004
85	24,70	5,50	4,67	10,54	4277,2		2400	1642,9		Childs et al, 2004
86	24,70	5,50	4,67	10,54	4277,2		3450	2361,7		Childs et al, 2004
87	24,70	5,50	4,67	10,54	4277,2		2315	1584,7		Childs et al, 2004
88	24,70	5,50	4,67	10,54	4277,2		3950	2704,0		Childs et al, 2004
89	24,70	5,50	4,67	10,54	4277,2		3775	2584,2		Childs et al, 2004
90	24,70	5,50	4,67	10,54	4277,2		2820	1930,4		Childs et al, 2004
91	24,70	5,50	4,67	10,54	4277,2		3025	2070,8		Childs et al, 2004
92	24,70	5,50	4,67	10,54	4277,2		3900	2669,7		Childs et al, 2004
93	24,70	5,50	4,67	10,54	4277,2		3200	2190,6		Childs et al, 2004
94	24,70	5,50	4,67	10,54	4277,2		3825	2618,4		Childs et al, 2004
95	24,70	5,50	4,67	10,54	4277,2		3700	2532,8		Childs et al, 2004
96	24,70	5,50	4,67	10,54	4277,2		3810	2608,1		Childs et al, 2004
97	24,70	5,50	4,67	10,54	4277,2		3710	2539,7		Childs et al, 2004
98	24,70	5,50	4,67	10,54	4277,2		3930	2690,3		Childs et al, 2004
99	27,60	6,63	5,91	9,19	4598,9		1244	1738,3	1992	Childs et al, 2004
100	27,60	6,63	5,91	9,19	4598,9		1303	1820,8	1992	Childs et al, 2004
101	27,60	6,63	5,91	9,19	4598,9		1228	1716,0	1992	Childs et al, 2004
102	27,60	6,63	5,91	9,19	4598,9		1250	1746,7	1992	Childs et al, 2004
103	27,60	6,63	5,91	9,19	4598,9		1238	1730,0	1992	Childs et al, 2004
104	27,60	6,63	5,91	9,19	4598,9		1232	1721,6	1992	Childs et al, 2004

Attachment E: Cut pipes geometric measurements

Records obtained from Petrobras of pipes cut in BOP as part of commissioning procedures are illustrated from Figure 114 up to Figure 117.

Figure 114 - 5" x 19,5 lb/ft (2012)



Source: Personal file.

Figure 115 - 5 ½" x 21,90lb/ft (2011)



Source: Personal file.

Figure 116 - 5 7/8" x 26,7 lb/ft (2011).



Source: Personal file.

Figure 117 - 6 5/8" x 48,13 lb/ft (2011).



Source: Personal file.

Attachment F: Simulation results for pipe cut under different boundary conditions

Table 29 summarize the simulations performed in FEM for pipe cut in BOP. Each simulation i presents the normalized force to cut pipe (F^*) and corresponding energy balance (BE) as a function of project variables ($N^*, T^*, P_i^*, P_e^*, d^*, h^*$). A second set of FEM simulations using the same boundary conditions but suppressing internal and external pressures ($P_i^* = 0, P_e^* = 0$) also presented results for normalized force to cut pipe (F_2^*) and corresponding energy balance (BE_2^*).

Table 29 - FEM simulations results

i	N^*	T^*	P_i^*	P_e^*	d^*	h^*	F^*	BE	F_2^*	BE_2^*
0	-0.006	0.000	0.000	0.000	0.000	0.050	0.393	y	0.393	y
1	0.427	0.139	0.313	0.317	0.998	1.000	0.403	y	0.360	y
2	0.210	0.069	0.157	0.159	0.499	0.525	0.358	y	0.358	y
3	0.102	0.035	0.078	0.238	0.748	0.763	0.276	n	0.349	y
4	0.319	0.104	0.235	0.079	0.249	0.288	0.530	y	0.428	y
5	0.373	0.052	0.117	0.040	0.125	0.881	0.436	y	0.375	y
6	0.265	0.017	0.274	0.198	0.374	0.169	0.433	y	0.379	y
7	0.048	0.122	0.039	0.278	0.873	0.406	0.214	n	0.346	y
8	0.156	0.087	0.196	0.119	0.624	0.644	0.420	y	0.358	y
9	0.129	0.130	0.254	0.297	0.561	0.466	0.332	y	0.327	y
10	0.075	0.061	0.137	0.258	0.935	0.703	0.246	n	0.337	y
11	0.021	0.026	0.059	0.178	0.436	0.584	0.326	n	0.355	y
12	0.183	0.009	0.294	0.099	0.312	0.347	0.511	y	0.410	y
13	0.346	0.113	0.098	0.218	0.187	0.822	0.315	y	0.383	y
14	0.400	0.095	0.020	0.020	0.686	0.941	0.345	y	0.369	y
15	0.237	0.043	0.215	0.139	0.062	0.109	0.492	y	0.446	y
16	0.292	0.078	0.176	0.059	0.811	0.228	0.399	y	0.330	y
17	0.116	0.100	0.010	0.208	0.218	0.614	0.235	n	0.399	y
18	0.170	0.039	0.245	0.287	0.094	0.080	0.398	y	0.386	y
19	0.143	0.109	0.147	0.050	0.717	0.733	0.396	y	0.342	y
20	0.359	0.135	0.088	0.169	0.530	0.317	0.293	y	0.338	y
21	0.089	0.013	0.108	0.069	0.343	0.555	0.406	y	0.380	y
22	0.386	0.048	0.186	0.010	0.405	0.436	0.464	y	0.348	y
23	0.278	0.056	0.225	0.268	0.156	0.970	0.379	y	0.372	y
24	0.251	0.074	0.284	0.030	0.842	0.911	0.480	y	0.338	y
25	0.332	0.030	0.264	0.248	0.966	0.852	0.366	y	0.362	y

26	0.197	0.082	0.205	0.307	0.655	0.139	0.258	n	0.372	y
27	0.224	0.004	0.166	0.089	0.592	0.792	0.429	y	0.394	y
28	0.008	0.022	0.068	0.149	0.779	0.673	0.258	n	0.326	y
29	0.062	0.126	0.303	0.109	0.904	0.258	0.445	y	0.421	y
30	0.035	0.091	0.127	0.228	0.031	0.198	0.320	n	0.339	y
31	0.413	0.117	0.029	0.129	0.468	0.495	0.290	y	0.422	y
32	0.305	0.065	0.049	0.188	0.281	0.377	0.321	n	0.335	y
33	0.082	0.033	0.083	0.064	0.701	0.124	0.347	y	0.368	y
34	0.150	0.115	0.171	0.164	0.109	0.570	0.396	y	0.352	y
35	0.271	0.046	0.132	0.263	0.857	0.273	0.234	n	0.364	y
36	0.339	0.002	0.289	0.035	0.359	0.302	0.539	y	0.417	y
37	0.231	0.106	0.269	0.074	0.296	0.748	0.545	y	0.394	y
38	0.258	0.011	0.024	0.114	0.608	0.421	0.300	y	0.350	y
39	0.136	0.137	0.015	0.005	0.920	0.926	0.346	y	0.355	y
40	0.041	0.059	0.210	0.084	0.234	0.480	0.478	y	0.368	y
41	0.122	0.041	0.220	0.015	0.203	0.688	0.535	y	0.358	y
42	0.014	0.124	0.161	0.144	0.452	0.065	0.370	y	0.347	y
43	0.001	0.063	0.298	0.094	0.670	0.777	0.452	y	0.352	y
44	0.190	0.024	0.113	0.203	0.733	0.985	0.276	n	0.420	y
45	0.325	0.089	0.230	0.045	0.016	0.510	0.561	y	0.379	y
46	0.068	0.132	0.073	0.283	0.140	0.095	0.225	n	0.400	y
47	0.393	0.050	0.093	0.055	0.577	0.540	0.424	y	0.361	y
48	0.028	0.093	0.005	0.302	0.483	0.213	0.136	n	0.327	y
49	0.285	0.102	0.201	0.273	0.795	0.243	0.299	y	0.353	y
50	0.380	0.054	0.044	0.223	0.421	0.955	0.245	y	0.323	y
51	0.095	0.080	0.064	0.292	0.889	0.391	0.167	n	0.408	y
52	0.298	0.085	0.308	0.104	0.078	0.629	0.463	y	0.309	y
53	0.407	0.067	0.152	0.124	0.826	0.896	0.336	y	0.344	y
54	0.366	0.028	0.054	0.134	0.514	0.599	0.290	y	0.364	y
55	0.217	0.007	0.191	0.193	0.546	0.718	0.347	y	0.349	y
56	0.163	0.037	0.240	0.312	0.982	0.807	0.288	y	0.406	y
57	0.109	0.098	0.034	0.173	0.265	0.451	0.315	n	0.428	y
58	0.055	0.015	0.142	0.233	0.047	0.154	0.330	n	0.379	y
59	0.177	0.111	0.250	0.253	0.639	0.362	0.380	y	0.370	y
60	0.312	0.020	0.181	0.025	0.390	0.837	0.467	y	0.417	y
61	0.420	0.128	0.103	0.183	0.327	0.184	0.366	y	0.370	y
62	0.244	0.119	0.279	0.154	0.951	0.659	0.439	y	0.433	y
63	0.352	0.072	0.259	0.213	0.171	0.332	0.413	y	0.330	y
64	0.204	0.076	0.122	0.243	0.764	0.866	0.273	n	0.348	y
65	0.214	0.086	0.042	0.221	0.927	0.547	0.192	n	0.365	y
66	0.099	0.062	0.281	0.047	0.585	0.696	0.497	y	0.326	y
67	0.295	0.075	0.179	0.196	0.896	0.191	0.316	y	0.372	y
68	0.315	0.029	0.159	0.305	0.210	0.414	0.310	y	0.433	y
69	0.275	0.081	0.296	0.265	0.055	0.280	0.457	y	0.427	y

70	0.079	0.107	0.051	0.166	0.132	0.770	0.321	n	0.359	y
71	0.390	0.101	0.198	0.057	0.382	0.443	0.453	y	0.397	y
72	0.241	0.005	0.252	0.186	0.148	0.176	0.445	y	0.367	y
73	0.004	0.103	0.032	0.022	0.507	0.814	0.372	y	0.443	y
74	0.268	0.023	0.286	0.280	0.023	0.948	0.453	y	0.321	y
75	0.288	0.042	0.291	0.107	0.834	0.592	0.427	y	0.408	y
76	0.207	0.038	0.267	0.136	0.117	0.889	0.510	y	0.346	y
77	0.112	0.049	0.227	0.002	0.740	0.844	0.470	y	0.360	y
78	0.092	0.094	0.086	0.290	0.631	0.354	0.217	n	0.422	y
79	0.180	0.123	0.237	0.121	0.086	0.740	0.498	y	0.368	y
80	0.072	0.084	0.218	0.112	0.164	0.488	0.529	y	0.351	y
81	0.153	0.092	0.262	0.235	0.850	0.102	0.367	y	0.329	y
82	0.336	0.051	0.193	0.211	0.803	0.651	0.317	y	0.323	y
83	0.261	0.068	0.110	0.201	0.865	0.369	0.267	y	0.315	y
84	0.200	0.066	0.002	0.285	0.912	0.859	0.177	n	0.449	y
85	0.396	0.105	0.100	0.315	0.179	0.310	0.232	n	0.325	y
86	0.146	0.053	0.056	0.206	0.974	0.399	0.258	n	0.413	y
87	0.160	0.058	0.061	0.087	0.288	0.325	0.408	y	0.394	y
88	0.126	0.125	0.081	0.082	0.351	0.132	0.407	y	0.413	y
89	0.329	0.064	0.095	0.245	0.366	0.384	0.279	y	0.347	y
90	0.173	0.118	0.037	0.116	0.943	0.458	0.275	y	0.361	y
91	0.187	0.127	0.125	0.072	0.475	0.666	0.395	y	0.405	y
92	0.166	0.040	0.091	0.255	0.273	0.577	0.263	n	0.335	y
93	0.045	0.001	0.139	0.092	0.787	0.785	0.359	y	0.420	y
94	0.011	0.008	0.017	0.126	0.070	0.874	0.305	n	0.394	y
95	0.234	0.110	0.164	0.176	0.195	0.829	0.428	y	0.411	y
96	0.194	0.114	0.169	0.017	0.101	0.755	0.516	y	0.364	y
97	0.085	0.016	0.311	0.027	0.600	0.904	0.535	y	0.352	y
98	0.281	0.003	0.276	0.141	0.725	0.621	0.441	y	0.368	y
99	0.302	0.018	0.174	0.037	0.881	0.963	0.429	y	0.407	y
100	0.356	0.120	0.012	0.161	0.257	0.236	0.323	y	0.346	y
101	0.322	0.129	0.115	0.300	0.709	0.221	0.240	n	0.352	y
102	0.383	0.136	0.247	0.191	0.429	0.800	0.386	y	0.338	y
103	0.410	0.077	0.208	0.131	0.538	0.993	0.452	y	0.400	y
104	0.119	0.112	0.007	0.151	0.226	0.117	0.323	n	0.321	y
105	0.018	0.047	0.183	0.067	0.959	0.933	0.397	y	0.418	y
106	0.349	0.088	0.301	0.032	0.491	0.918	0.550	y	0.400	y
107	0.051	0.021	0.223	0.097	0.008	0.295	0.492	y	0.342	y
108	0.363	0.090	0.149	0.226	0.444	0.087	0.301	y	0.364	y
109	-0.003	0.060	0.242	0.012	0.522	0.978	0.528	y	0.349	y
110	0.065	0.014	0.071	0.275	0.694	0.532	0.182	n	0.355	y
111	0.024	0.055	0.105	0.230	0.397	0.072	0.287	n	0.335	y
112	0.038	0.044	0.144	0.270	0.772	0.518	0.216	n	0.420	y
113	0.139	0.138	0.203	0.260	0.039	0.503	0.403	y	0.344	y
114	0.106	0.012	0.213	0.042	0.990	0.339	0.442	y	0.384	y

115	0.342	0.079	0.154	0.156	0.662	0.711	0.362	y	0.353	y
116	0.309	0.010	0.022	0.146	0.413	0.057	0.299	n	0.340	y
117	0.417	0.027	0.130	0.007	0.460	0.429	0.417	y	0.423	y
118	0.423	0.031	0.272	0.250	0.320	0.265	0.431	y	0.431	y
119	0.403	0.034	0.306	0.240	0.242	0.206	0.456	y	0.341	y
120	0.133	0.097	0.076	0.171	0.678	0.473	0.284	n	0.419	y
121	0.376	0.131	0.066	0.052	0.335	0.146	0.428	y	0.370	y
122	0.221	0.116	0.257	0.310	0.553	0.636	0.340	y	0.376	y
123	0.254	0.025	0.232	0.062	0.647	0.161	0.473	y	0.405	y
124	0.058	0.099	0.188	0.295	0.304	0.681	0.356	n	0.333	y
125	0.031	0.133	0.027	0.102	0.818	0.725	0.275	n	0.342	y
126	0.248	0.036	0.120	0.077	0.756	0.607	0.374	y	0.331	y
127	0.227	0.071	0.046	0.216	0.569	0.562	0.312	n	0.371	y
128	0.369	0.073	0.135	0.181	0.616	0.250	0.341	y	0.335	y
129	0.178	0.124	0.263	0.284	0.892	0.262	0.320	y	0.345	y
130	0.425	0.110	0.199	0.294	0.674	0.662	0.299	y	0.336	y
131	0.182	0.092	0.016	0.311	0.931	0.514	0.141	n	0.356	y
132	0.361	0.105	0.087	0.162	0.916	0.187	0.306	y	0.347	y
133	0.104	0.076	0.226	0.053	0.518	0.143	0.468	y	0.443	y
134	0.259	0.001	0.170	0.274	0.004	0.751	0.363	n	0.350	y
135	0.344	0.086	0.202	0.177	0.994	0.202	0.368	y	0.322	y
136	0.273	0.113	0.187	0.296	0.853	0.766	0.268	n	0.360	y
137	0.117	0.002	0.104	0.229	0.409	0.432	0.324	n	0.393	y
138	0.243	0.019	0.040	0.237	0.760	0.158	0.222	n	0.358	y
139	0.226	0.074	0.190	0.073	0.744	0.106	0.427	y	0.324	y
140	0.300	0.075	0.209	0.038	0.869	0.403	0.424	y	0.376	y
141	0.239	0.138	0.307	0.207	0.417	0.699	0.474	y	0.323	y
142	0.283	0.122	0.062	0.197	0.877	0.180	0.221	n	0.321	y
143	0.124	0.049	0.231	0.100	0.807	0.358	0.428	y	0.410	y
144	0.063	0.007	0.131	0.276	0.090	0.788	0.207	n	0.387	y
145	0.320	0.079	0.097	0.128	0.596	0.343	0.366	y	0.437	y
146	0.263	0.005	0.251	0.123	0.043	0.291	0.528	y	0.448	y
147	0.175	0.078	0.283	0.182	0.027	0.440	0.503	y	0.325	y
148	0.138	0.025	0.305	0.031	0.791	0.417	0.475	y	0.404	y
149	0.097	0.024	0.094	0.063	0.238	0.863	0.432	y	0.371	y
150	0.165	0.067	0.182	0.147	0.183	0.647	0.421	y	0.388	y
151	0.314	0.097	0.309	0.242	0.144	0.469	0.455	y	0.379	y
152	0.070	0.114	0.180	0.024	0.495	0.306	0.455	y	0.429	y
153	0.046	0.061	0.028	0.056	0.097	0.365	0.411	y	0.411	y
154	0.158	0.068	0.177	0.019	0.191	0.410	0.565	y	0.358	y
155	0.364	0.044	0.290	0.078	0.924	0.083	0.457	y	0.362	y
156	0.144	0.023	0.285	0.009	0.705	0.336	0.495	y	0.375	y
157	0.209	0.136	0.292	0.227	0.651	0.677	0.413	y	0.403	y
158	0.023	0.031	0.070	0.165	0.199	0.328	0.309	n	0.384	y

159	0.280	0.094	0.009	0.145	0.168	0.655	0.320	n	0.401	y
160	0.040	0.011	0.079	0.222	0.292	0.098	0.176	n	0.400	y
161	0.205	0.103	0.163	0.150	0.464	0.284	0.374	y	0.403	y
162	0.033	0.096	0.065	0.108	0.284	0.150	0.404	y	0.324	y
163	0.310	0.119	0.043	0.058	0.838	0.276	0.322	y	0.386	y
164	0.219	0.033	0.067	0.261	0.339	0.900	0.228	y	0.408	y
165	0.391	0.100	0.075	0.140	0.370	0.870	0.317	y	0.402	y
166	0.256	0.055	0.246	0.143	0.425	0.959	0.426	y	0.334	y
167	0.266	0.093	0.297	0.029	0.775	0.670	0.491	y	0.386	y
168	0.395	0.050	0.141	0.066	0.214	0.581	0.475	y	0.447	y
169	0.229	0.101	0.172	0.113	0.129	0.551	0.417	y	0.358	y
170	0.172	0.030	0.150	0.281	0.456	0.774	0.262	n	0.397	y
171	0.043	0.120	0.102	0.041	0.323	0.796	0.446	y	0.367	y
172	0.148	0.029	0.248	0.212	0.401	0.878	0.389	y	0.386	y
173	0.347	0.004	0.302	0.046	0.160	0.373	0.580	y	0.359	y
174	0.324	0.014	0.099	0.219	0.721	0.135	0.278	y	0.386	y
175	0.290	0.107	0.133	0.138	0.487	0.477	0.369	y	0.334	y
176	0.216	0.039	0.168	0.239	0.861	0.447	0.291	y	0.326	y
177	0.236	0.095	0.006	0.172	0.830	0.172	0.210	n	0.350	y
178	0.381	0.045	0.148	0.051	0.737	0.061	0.387	y	0.365	y
179	0.246	0.080	0.119	0.187	0.690	0.076	0.326	y	0.317	y
180	0.408	0.028	0.165	0.266	0.768	0.484	0.267	y	0.353	y
181	-0.001	0.032	0.121	0.271	0.666	0.054	0.233	n	0.422	y
182	0.151	0.130	0.001	0.095	0.019	0.499	0.355	n	0.378	y
183	0.077	0.106	0.253	0.170	0.565	0.848	0.450	y	0.330	y
184	0.094	0.059	0.018	0.204	0.713	0.299	0.224	n	0.377	y
185	0.192	0.037	0.116	0.014	0.386	0.744	0.425	y	0.386	y
186	0.297	0.053	0.092	0.081	0.121	0.247	0.405	y	0.365	y
187	0.307	0.099	0.126	0.214	0.394	0.232	0.311	y	0.336	y
188	0.050	0.040	0.185	0.006	0.814	0.996	0.438	y	0.345	y
189	0.002	0.071	0.280	0.152	0.066	0.610	0.503	y	0.362	y
190	0.253	0.010	0.072	0.026	0.479	0.462	0.394	y	0.432	y
191	0.418	0.036	0.312	0.130	0.136	0.269	0.500	y	0.383	y
192	0.303	0.116	0.258	0.115	0.253	0.573	0.408	y	0.392	y
193	0.067	0.027	0.035	0.190	0.557	0.254	0.250	n	0.353	y
194	0.121	0.065	0.077	0.264	0.355	0.818	0.246	n	0.376	y
195	0.009	0.083	0.053	0.120	0.698	0.714	0.280	n	0.443	y
196	0.195	0.043	0.234	0.076	0.752	0.558	0.434	y	0.376	y
197	0.060	0.091	0.033	0.167	0.573	0.937	0.241	n	0.373	y
198	0.276	0.131	0.207	0.004	0.012	0.210	0.571	y	0.397	y
199	0.202	0.098	0.295	0.135	0.152	0.855	0.508	y	0.384	y
200	0.249	0.132	0.204	0.068	0.659	0.217	0.446	y	0.312	y
201	0.334	0.081	0.268	0.299	0.347	0.596	0.364	y	0.413	y
202	0.270	0.088	0.109	0.291	0.503	0.091	0.213	n	0.336	y
203	0.006	0.034	0.128	0.301	0.783	0.640	0.172	n	0.387	y

204	0.371	0.012	0.275	0.001	0.799	0.113	0.492	y	0.416	y
205	0.134	0.137	0.212	0.180	0.300	0.915	0.442	y	0.363	y
206	0.188	0.041	0.143	0.254	0.581	0.707	0.299	n	0.365	y
207	0.287	0.003	0.229	0.200	0.612	0.625	0.405	y	0.359	y
208	0.415	0.125	0.153	0.257	0.316	0.224	0.340	y	0.401	y
209	0.107	0.072	0.192	0.110	0.378	0.544	0.470	y	0.355	y
210	0.013	0.069	0.013	0.309	0.526	0.729	0.160	n	0.372	y
211	0.185	0.052	0.021	0.061	0.729	0.195	0.328	y	0.353	y
212	0.090	0.008	0.114	0.306	0.074	0.121	0.255	n	0.364	y
213	0.337	0.135	0.138	0.021	0.986	0.833	0.425	y	0.420	y
214	0.317	0.121	0.287	0.043	0.643	0.165	0.525	y	0.390	y
215	0.073	0.126	0.221	0.304	0.970	0.737	0.265	n	0.325	y
216	0.405	0.048	0.300	0.090	0.362	0.313	0.529	y	0.379	y
217	0.398	0.057	0.048	0.033	0.261	0.974	0.414	y	0.353	y
218	0.330	0.133	0.158	0.247	0.588	0.529	0.323	y	0.415	y
219	0.111	0.070	0.238	0.279	0.939	0.425	0.314	y	0.401	y
220	0.114	0.108	0.084	0.125	0.627	0.967	0.355	y	0.399	y
221	0.019	0.087	0.224	0.244	0.448	0.069	0.317	n	0.396	y
222	0.232	0.066	0.216	0.105	0.269	0.944	0.501	y	0.440	y
223	0.053	0.056	0.055	0.314	0.308	0.885	0.070	n	0.319	y
224	0.354	0.085	0.214	0.048	0.222	0.321	0.514	y	0.380	y
225	0.141	0.046	0.197	0.217	0.277	0.454	0.417	y	0.333	y
226	0.293	0.015	0.265	0.175	0.035	0.722	0.501	y	0.338	y
227	0.199	0.062	0.045	0.224	0.846	0.759	0.204	n	0.345	y
228	0.378	0.134	0.236	0.155	0.207	0.492	0.494	y	0.327	y
229	0.080	0.123	0.031	0.195	0.947	0.603	0.233	n	0.431	y
230	0.087	0.082	0.124	0.157	0.900	0.840	0.341	y	0.341	y
231	0.422	0.009	0.175	0.160	0.440	0.388	0.427	y	0.373	y
232	0.026	0.129	0.278	0.209	0.955	0.692	0.374	y	0.345	y
233	0.327	0.021	0.111	0.036	0.051	0.618	0.487	y	0.394	y
234	0.057	0.104	0.243	0.016	0.885	0.811	0.521	y	0.350	y
235	0.084	0.006	0.050	0.093	0.620	0.588	0.366	y	0.313	y
236	0.036	0.063	0.026	0.232	0.978	0.536	0.149	n	0.372	y
237	0.374	0.109	0.106	0.011	0.331	0.566	0.457	y	0.344	y
238	0.212	0.090	0.155	0.133	0.682	0.952	0.389	y	0.341	y
239	0.412	0.054	0.136	0.289	0.908	0.351	0.220	y	0.362	y
240	0.101	0.084	0.023	0.286	0.542	0.781	0.166	n	0.376	y
241	0.155	0.016	0.057	0.234	0.963	0.395	0.207	n	0.423	y
242	-0.004	0.020	0.270	0.259	0.604	0.892	0.387	y	0.369	y
243	0.128	0.017	0.038	0.316	0.472	0.922	0.256	n	0.341	y
244	0.351	0.073	0.082	0.192	0.105	0.380	0.327	y	0.391	y
245	0.368	0.022	0.194	0.252	0.058	0.521	0.391	y	0.426	y
246	0.131	0.047	0.241	0.086	0.433	0.239	0.470	y	0.334	y
247	0.402	0.018	0.146	0.103	0.511	0.826	0.406	y	0.316	y

248	0.161	0.060	0.011	0.098	0.175	0.506	0.328	n	0.370	y
249	0.168	0.058	0.089	0.083	0.246	0.128	0.420	y	0.375	y
250	0.016	0.117	0.256	0.185	0.534	0.633	0.412	y	0.434	y
251	0.388	0.112	0.060	0.118	0.822	0.989	0.286	y	0.363	y
252	0.385	0.118	0.273	0.202	0.113	0.685	0.471	y	0.431	y
253	0.029	0.111	0.261	0.071	0.549	0.929	0.507	y	0.352	y
254	0.341	0.042	0.004	0.249	0.230	0.803	0.227	n	0.393	y
255	0.222	0.035	0.160	0.269	0.635	0.907	0.338	n	0.360	y
256	0.358	0.127	0.219	0.088	0.082	0.981	0.529	y	0.358	y
257	0.101	0.132	0.261	0.205	0.668	0.631	0.399	y	0.349	y

Attachment G: Petrobras data disclaimer

Petrobras data use in this thesis was allowed by Mr. Lucas Saber Rocha on 12th April 2019 under the condition of not relating operators and manufactures to experimental results.

Nikolas Lukin

De: Lucas Saber Rocha
Enviado em: sexta-feira, 12 de abril de 2019 07:18
Para: Nikolas Lukin
Cc: Ricardo Barroso Ballona; Dalisson Santos Vieira
Assunto: Re: PADRÃO - REALIZAR DIVULGAÇÃO EXTERNA DE TRABALHOS TÉCNICOS E/OU CIENTÍFICOS

Nikolas,

Não vejo problemas no uso das informações de teste de corte para o seu doutorado. Peço apenas não mencionar os nomes das empresas contratadas e fabricantes, se atendo às informações técnicas do corte.

Atenciosamente,

Lucas Sáber Rocha

-----Nikolas Lukin/BRA/Petrobras escreveu: -----

Para: Lucas Saber Rocha/BRA/Petrobras@Petrobras
De: Nikolas Lukin/BRA/Petrobras
Data: 07/04/2019 07:52 AM
cc: Ricardo Barroso Ballona/BRA/Petrobras@PETROBRAS
Assunto: Re: PADRÃO - REALIZAR DIVULGAÇÃO EXTERNA DE TRABALHOS TÉCNICOS E/OU CIENTÍFICOS

Saber, bom dia

Conforme conversamos, segue o meu pedido para utilizar informações de testes de corte provenientes da Petrobras no meu trabalho de doutorado. Pretendo utilizar os dados de corte no BOP de tubos S-135 (informações do tubular, força de corte, gaveta utilizada, gráficos e fotografias) realizados entre os anos de 2011 e 2016. Não irei divulgar datas, sondas ou inspetor que acompanhou o teste. Estimo que utilizarei dados de menos de 20 testes. Resumo do trabalho:

Modelagem e calibração da falha dúctil por cisalhamento do aço API S-135 para aplicações offshore

"O objetivo científico desta tese é analisar e desenvolver um modelo de falha em cisalhamento para o aço API S-135 para ser implementado em simulações numéricas de elementos finitos (FEM). Por outro lado, o propósito tecnológico deste trabalho é determinar a força necessária para um indentador cortar um tubular, uma vez que este problema tem aplicações em problemas de modelagem de perfurações offshore podendo ser usado para determinar a capacidade e a confiabilidade de um BOP (BlowOut Preventers) executar uma operação de corte de colunas de perfuração em situações de emergência. Em uma primeira etapa, o modelo de falha dúctil por cisalhamento é selecionado e desenvolvido. A seguir o problema de corte de tubular em BOP é modelado em FEM (Abaqus) e a calibração do modelo de falha é feita com base em ensaios destrutivos de corpos de prova usinados a partir de uma amostra de um tubular do aço S-135. O corte de diversos tamanhos de tubulares foram simulados para comparar o modelo proposto com os resultados experimentais. Finalmente, uma análise de sensibilidade é realizada para verificar a validade do modelo ao longo das condições de trabalho de uma coluna de perfuração."

Ressalto que estas informações já existem na literatura (S. E. West, Shear Study for U.S. Minerals Management Service, Requisition No. 2-1011-1003, U.S. Minerals Management Service, 2004), porém os dados da Petrobras são mais atualizados, possuem outras informações (fotos e gráficos) e serão um

Attachment H: Publications derived from this thesis

Parts of this thesis have been published in the following articles:

LUKIN, Nikolas; MOURA, Rafael Traldi; ALVES, Marcilio; BRÜNIG, Michael; DRIEMEIER, Larissa, “Analysis of API S-135 steel drill pipe cutting process by blowout preventer”, *Journal of Petroleum Science and Engineering*, Volume **195**, 2020, 107819, ISSN 0920-4105, <https://doi.org/10.1016/j.petrol.2020.107819>.

(<http://www.sciencedirect.com/science/article/pii/S0920410520308809>)

LUKIN, Nikolas; DRIEMEIER, Larissa, “Using metamodels to predict shear forces in BOP”, *Rio Oil & Gas Expo and Conference 2020*, Rio de Janeiro, RJ, Brazil, 2020 (**20**), ISSN 2525-7579, <https://doi.org/10.48072/2525-7579.rog.2020.130>

(https://icongresso.ibp.itarget.com.br/arquivos/trabalhos_completos/ibp/3/final.IBP0781_20_26112020_164533.pdf)

<This page is intentionally left in blank>